January 2015

Advancement of 31P Magnetic Resonance Spectroscopy Using GRAPPA Reconstruction on a 3D Volume

Tony Clevenger
Purdue University

Graduate School Form 30
Updated 1/15/2015

PURDUE UNIVERSITY
GRADUATE SCHOOL
Thesis/Dissertation Acceptance

This is to certify that the thesis/dissertation prepared

By TONY CLEVENGER

Entitled
ADVANCEMENT OF 31P MAGNETIC RESONANCE SPECTROSCOPY USING GRAPPA RECONSTRUCTION ON A 3D VOLUME

For the degree of Doctor of Philosophy

Is approved by the final examining committee:

ANDREW HIRSCH
Chair

ULRIKE DYDAK
Co-chair

JOHN FINLEY

JORGE RODRIGUEZ

To the best of my knowledge and as understood by the student in the Thesis/Dissertation Agreement, Publication Delay, and Certification Disclaimer (Graduate School Form 32), this thesis/dissertation adheres to the provisions of Purdue University's "Policy of Integrity in Research" and the use of copyright material.

Approved by Major Professor(s): ANDREW HIRSCH

Approved by: ANDREW HIRSCH 7-6-2015
Head of the Departmental Graduate Program Date

ADVANCEMENT OF ^{31}P MAGNETIC RESONANCE SPECTROSCOPY USING GRAPPA RECONSTRUCTION ON A 3D VOLUME

A Dissertation

Submitted to the Faculty

of

Purdue University

by

Tony Clevenger

In Partial Fulfillment of the

Requirements for the Degree

of

Doctor of Philosophy

August 2015

Purdue University

West Lafayette, Indiana

For my loving parents, David and Amanda Clevenger, and my beautiful wife, Jamie Clevenger.

I love you all

ACKNOWLEDGMENTS

I wish to thank Dr. Andrew Hirsch and Dr. Ulrike Dydak in their support and encouragement through this journey. They took me in, a floundering graduate student, and turned me into the candidate I am today. I will be forever grateful for all that you both of done for me. I would also like to thank Dr. Anshuman Panda and Dr. Scott Jones for their help and guidance with this project. They laid the groundwork for my success and I cannot thank them enough!

To all the technical staff and faculty at the Indiana University School of Medicine, Indianapolis, IN. Specifically I would thank Michele Beal, Traci Day, Rob Bryant, Scott Persohn, and Courtney Robbins. Without their hard work and persistence this work would have been stalled long ago and we would not be where we are today. Thank you.

I would also like to recognize my friends and support at Purdue University. These last seven years have had their ups and downs, but through all of it, we were there for each other. I cannot express the comfort I have found from them while they lent me their support and guidance. They have also made the time here an enjoyable one, whether it was staying in and playing games or going out on the town for a night out. I could not have made it this far without them. Thank you.

I would thank my wife, Jamie Clevenger, for her support through these trying times. She has been my rock through these tough times and long nights. She has had more patience than should be asked for and I am forever grateful. Thank you, my love.

And finally, to my parents. Thank you for sacrificing all that you have to allow me to get to where I am today. Thank you for lending me the support that only parents can give. Thank you for encouraging me, even as the years dragged on. Thank you for all of the lessons you've taught me throughout the years that have gotten me this

far. Thank you a thousand different ways. But most importantly, thank you for being you. I love you both!

Thank you all!

TABLE OF CONTENTS

LIST OF TABLES

LIST OF FIGURES

ABBREVIATIONS

GRAPPA	Generalized Autocalibrating Partially Parallel Acquisitions
SMASH	SiMultaneous Acquisition of Spatial Harmonics
AUTO-SMASH	AUTOmatic-SMASH
MRS	Magnetic Resonance Spectroscopy
MRI	Magnetic Resonance Imaging
NMR	Nuclear Magnetic Resonance
HCC	Hepatocellular Carcinoma
SBRT	Stereotactic Body Radiation Therapy
SIRT	Selective Internal Radiation Therapy
Y90	Yttrium-90
PME	Phosphomonoester
PDE	Phosphodiester
PCr	Phosphocreatine
ATP	Adenosine Triphosphate
FOV	Field of View
ROI	Region of Interest
ACS	Auto-Calibration Signal
SAR	Specific Absorption Rate
TE	Echo Time
TR	Repetition Time
SNR	Signal-to-Noise Ratio
MR	Magnetic Resonance
TX	Transmit
RX	Receive
PSF	Point Spread Function

RF	Radio Frequency
CSI	Chemical Shift Image
CT	Computerized Tomography
SEG	Slice Encoding Gradient
FEG	Frequency Encoding Gradient
PEG	Phase Encoding Gradient
FT	Fourier Transform
US	Undersample
ACR	American College of Radiology

NOMENCLATURE

Anterior	Front of the body
Posterior	Back of the body
Sagital View	View from side-to-side
Coronal View	View from chest-to-back or back-to-chest
Axial/Transverse View	View along the body from head-to-toe or toe-to-head
Voxel	3D pixel; also a volume element for spectroscopic positioning
Isocenter	The central position of the scanner with a homogeneous B_0 field

GLOSSARY

Resection	Removal of tissues or organs
T_1	Spin-lattice interaction time constant; decay time constant due to interaction between spins and lattice
T_2	Spin-spin interaction time constant; decay time constant due to interactions with other spins
T_2*	Modified spin-spin interaction time constant; Similar to T_2 but also takes into account field inhomogeneities
Phantom	A container containing a controlled substance in which to test new sequences without the risk of harming a living subject
B_0	The main magnetic field produced in the bore of the scanner
M_{long}	The component of the magnetization vector that points along the B_0 field
M_{trans}	The component of the magnetization vector that is perpendicular to the B_0 field
PSF	A measure of the quality of the localization of a signal

ABSTRACT

Clevenger, Tony Ph.D., Purdue University, August 2015. Advancement of ^{31}P Magnetic Resonance Spectroscopy Using GRAPPA Reconstruction on a 3D Volume. Major Professors: Andrew Hirsch and Ulrike Dydak.

The overall objective of this research is to improve currently available metabolic imaging techniques for clinical use in monitoring and predicting treatment response to radiation therapy in liver cancer. Liver metabolism correlates with inflammatory and neoplastic liver diseases, which alter the intracellular concentration of phosphorus-31 (^{31}P) metabolites [1]. It is assumed that such metabolic changes occur prior to physical changes of the tissue. Therefore, information on regional changes of ^{31}P metabolites in the liver, obtained by Magnetic Resonance Spectroscopic Imaging (MRSI) [1,2], can help in diagnosis and follow-up of various liver diseases. Specifically, there appears to be an immediate need of this technology for both the assessment of tumor response in patients with Hepatocellular Carcinoma (HCC) treated with Stereotactic Body Radiation Therapy (SBRT) [3–5], as well as assessment of radiation toxicity, which can result in worsening liver dysfunction [6]. Pilot data from our lab has shown that ^{31}P MRSI has the potential to identify treatment response five months sooner than conventional methods [7], and to assess the biological response of liver tissue to radiation 24 hours post radiation therapy [8]. While this data is very promising, commonly occurring drawbacks for ^{31}P MRSI are patient discomfort due to long scan times and prone positioning within the scanner, as well as reduced data quality due to patient motion and respiration. To further advance the full potential of ^{31}P MRSI as a clinical diagnostic tool in the management of liver cancer, this PhD research project had the following aims:

I) Reduce the long acquisition time of 3D ^{31}P MRS by formulating and implementing an appropriate GRAPPA undersampling scheme and reconstruction on a clinical MRI scanner

II) Testing and quantitative validation of GRAPPA reconstruction on 3D ^{31}P MRSI on developmental phantoms and healthy volunteers

At completion, this work should considerably advance ^{31}P MRSI as a clinical diagnostic tool for liver cancer, and potentially other cancer types, by reducing the amount of time needed to get relevant data for treatment efficacy of SBRT patients. Implementation of this work into our ongoing clinical study will further provide insights into whether the ^{31}P MSRI method can be an early predictor of normal tissue toxicity and/or treatment response.

1. Introduction and Background

1.1 Specific Aims

The increase in liver cancer in the last few years [9] has amplified the need to monitor cancer treatment in the liver. Currently, the method for monitoring a patient's response consists of observing the change in size of a tumor after an appropriate amount of time (3-6 months) using the RECIST criteria [10]. It has been proposed that use of phosphorous-31 magnetic resonance spectroscopy (^{31}P MRS) [1, 7, 11, 12] can be a suitable biomarker for liver response, post radiation treatment. The recent primary focus of this group is cancer treatment by Stereotactic Body Radiation Therapy (SBRT) [13–16] and studying the efficacy of treatment response. The purpose of this work is to advance the field of ^{31}P MRS in hopes of making ^{31}P MRS a viable option for clinical usage in monitoring a patient's response to radiation therapy. This has been achieved through the following two specific aims:

I) Reduce the long acquisition time of 3D ^{31}P MRS by formulating and implementing an appropriate GRAPPA undersampling scheme and reconstruction on a clinical MRI scanner

II) Testing and quantitative validation of GRAPPA reconstruction on 3D ^{31}P MRSI on developmental phantoms and healthy volunteers

1.2 ^{31}P MRS

Our group is proposing to use MRS as a faster way to determine treatment efficacy, motivated by the fact that the metabolism of a tumor should change faster than the physical characteristics of the tumor [17–19]. This is the motivating hypothesis of our ^{31}P liver studies and has been shown to be accurate thus far [7, 8, 20–22].

In-vivo MRS can be done on any nuclei that contain an odd number of protons and are abundant within a body. Commonly used nuclei are: hydrogen-1 (^{1}H), carbon-13 (^{13}C), phosphorous-31 (^{31}P), sodium-23 (^{23}Na), potassium-39 (^{39}K), and fluorine-19 (^{19}F) [23]. Table 1.2 show some common NMR properties of different nuclei. ^{31}P metabolites naturally occur as part of the human body's metabolism, making it a viable candidate for the study of the metabolism of tumorous tissue. Another benefit for using ^{31}P is the broad chemical shift range of ^{31}P resonances (30 ppm) on the frequency spectrum, which enable clean and easy identification of ^{31}P peaks [23]. Therefore, this study focuses on ^{31}P nuclei, particularly on certain phosphates and metabolites found in the human liver. Specifically, we focus on the following seven metabolites: α-ATP (alpha adenosine triphosphate), β-ATP (beta adenosine triphosphate), γ-ATP (gamma adenosine triphosphate), PCr (phosphocreatine), Pi (inorganic phosphate), PME (phosphomonoester), and PDE (phosphodiester). A brief description of each of these molecules follows:

Table 1.2 shows the chemical shift positions of the ^{31}P metabolites that will be studied here. ATP (pictured in Figure 1.1) is considered the metabolic "currency" of energy within the body. This molecule will produce three peaks in a ^{31}P spectrum corresponding to the three phosphate sites: α, β, and γ. Inorganic phosphate (Pi) is one of the products of metabolic chemical reactions that involve the breakdown of ATP, along with adenosine diphosphate (ADP). Note that ADP resonances are not shown in the in-vivo spectra because of their close proximity to the γ-ATP and the α-ATP resonances and thus cannot be distinguished from these peaks [23–25]. Consequently, though, the ADP peaks do contribute to the broadening of the γ-ATP and α-ATP peaks. Phosphocreatine (PCr) is a associated with areas of the body that contain muscle. It tends to act as a metabolic energy buffer, creating or breaking down ATP as needed. Note that since the liver is not a muscle, there should be no PCr found within the liver itself. Any PCr seen inside of voxels in the liver is a sign of signal bleeding.

Table 1.1
Approximate chemical shift positions of metabolites found in the liver, as stated in [23]. All shifts are referenced to PCr.

Molecule	**Chemical Shift Position (ppm)**
α-ATP	-7.52
β-ATP	-16.26
γ-ATP	-2.48
PCr	0.0
Pi	5.02
PME*	6.33*
PDE**	2.98**
*Location is averaged for contributions from PC and PE	(5.88+6.78)/2
**Location is averaged for contributions from GPC and GPE	(3.20+2.76)/2

Phosphodiesters (PDE) and Phosphomonoesters (PME) are two peaks that do not associate with one metabolite in particular, but, instead, refers to a mix of compounds at a specific chemical shift [2]. In tumors, PDE signals correspond to glycerophosphocholine (GPC) and glcerophosphoethanolamine (GPE) and suggest cell membrane degradation products [1]. PME signals, on the other hand, correspond to phosphocholine (PC) and phosphoethanoamine (PE) and tend to represent phospholipid cell membrane precursors [2].

It has been found that the signal from the PME and PDE peaks differ between cancerous and healthy tissue [26,27]. The PME level has been shown to increase while the PDE level appears to decrease [19] when compared to a healthy subjects. It has also been shown that the PME to ATP ratio will increase when compared to healthy

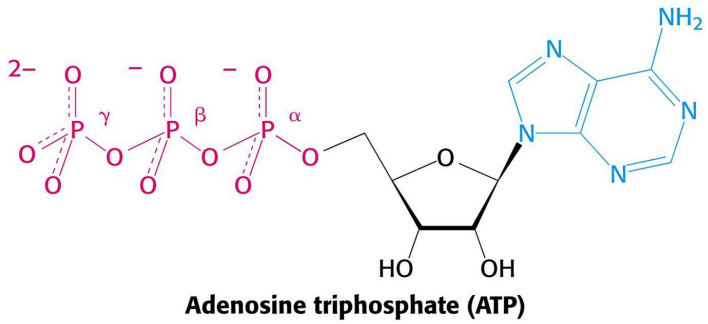

(a) ATP molecule

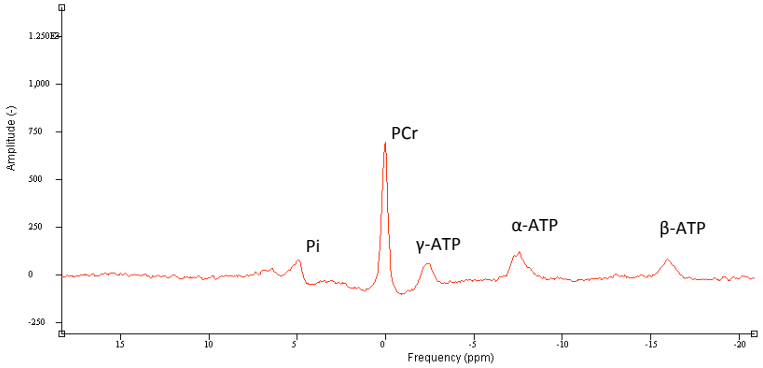

(b) Typical spectrum from a single voxel

Figure 1.1. Adenosine triphosphate (ATP), with the three ^{31}P nuclei (α, β, and γ) that give rise to the three peaks associated with the ATP molecule. The associated peaks are seen in the given spectrum.

subjects [28]. Thus, it appears that the naturally occurring phosphometabolites found within the liver can serve as a biomarker for treatment response much earlier than the physical properties of the tumor [29]. Figure 1.1(b) shows a typical spectrum from a single voxel of a 3D ^{31}P MRS scan.

Table 1.2
Different NMR properties with different isotopes. Information in this table was obtained from [23].

Isotope	Spin	Gyromagnetic Ratio (x$10^7 \frac{rad}{Ts}$)	f_{Larmor} at 2.35T (MHz)	f_{Larmor} at 3T (MHz)	Natural Abundance (%)	Sensitivity Relative to ^{1}H
^{1}H	$\frac{1}{2}$	26.752	100.000	127.66	99.985	1.00
^{13}C	$\frac{1}{2}$	6.728	25.145	32.1	1.108	1.76x10^{-4}
^{19}F	$\frac{1}{2}$	25.181	94.094	120.12	100	0.834
^{23}Na	$\frac{3}{2}$	7.080	26.466	33.79	100	9.27x10^{-2}
^{31}P	$\frac{1}{2}$	10.841	40.481	51.678	100	6.65x10^{-2}

The most commonly used coils for ^{31}P MRS studies are surface coils. Surface coils are only sensitive to a region over the areas of the coils and to a depth within the subject approximately equal to the diameter of the coil [30]. Using these surface coils, only small portions of the liver can be viewed at a time and no tumors deep within the liver can be seen. Surface coils have a high Signal-to-Noise-Ratio (SNR), but provide no information on the depth of what is seen. To achieve sampling of the whole liver and to obtain spatially resolved information on healthy and cancerous tissue, an 8 channel, phased array coil has been used [20]. This coil was specifically developed by Dr. Ulrike Dydak's group in conjunction with Stark Contrast MRI Coils Research from Erlangen, Germany. Technical details of this coil will be covered in Chapter 3, discussing the experimental setup.

1.2.1 Challenges with ^{31}P MRS

^{31}P MRS has a low sensitivity when compared to ^{1}H MRS. To account for this, many different averages are sampled during a scan. This allows us to obtain a higher SNR. Unfortunately, since each average takes approximately one second, the length

of a typical scan can quickly increase. In this case, where scans cover the whole liver, the scan times of conventional acquisitions are approximately 30 minutes. This increase in time leads to further complications: patient discomfort and respiratory motion artifacts. Thus, one of the reasons that ^{31}P MRS is not used as a clinical tool is the amount of time needed to acquire data. Other techniques such as weighted k-space scans, spiral acquisitions, and parallel spectral imaging have been developed to reduce the amount of scan time needed [23,31,32]. Recently, our group has developed a parallel imaging approach to reduce the amount of time needed for a scan [21].

The long scan times of ^{31}P MRS also tends to cause reproducibility problems due to respiration. Typically, since ^{1}H MRS tends to be much shorter than ^{31}P MRS, respiratory motion artifacts are not a concern. However, respiration during a long scan will lead to variability in the data due to voxel shifting, thus leading researchers to believe the ROI (region of interest) is in one place, while in fact it's in another due to the expansion and contraction of the lungs and diaphragm. In the case of this research, the tumor can be physically displaced to different locations during respiration because of this. Clearly there is a need to speed up the ^{31}P MRS acquisition time to reduce the amount of variation due to patient motion and respiration, which will be the topic discussed throughout the remainder of this work.

2. Theory

(Please see Appendix B for a thorough derivation of the MRI physics used)

2.1 k-space

k-space is often used in physics and especially when doing imaging or spectroscopy. The concept of k-space has maintained a firm foothold in the field of MRS and MRI with it's ability to easily convey ideas that would be hard to do in real/image space.

Data obtained with MR is stored in what is called the k-space matrix. This matrix is divided into bins and has coordinates given by (k_x, k_y, k_z) which are the given frequencies in the x, y, and z directions of k-space, respectively. The limits of the k-space dimensions would be given by $\pm f_{max,x}$ in the k_x direction, $\pm f_{max,y}$ in the k_y direction, and $\pm f_{max,z}$ in the k_z direction. The separation between these points in k-space is given by:

$$\begin{aligned} \Delta k_x &= \frac{2\pi}{FOV_x} \\ \Delta k_y &= \frac{2\pi}{FOV_y} \\ \Delta k_z &= \frac{2\pi}{FOV_z} \end{aligned} \tag{2.1}$$

which is easily seen when we look at Figure 2.1.

Here we see the inverse relationship that exists between real space and k-space. The resolution in real space is determined by the FOV in k-space while the resolution in k-space is determined by the FOV in real space. We see that if we were to increase our Δk by 2, then we would decrease our FOV by half. This leads to fold-over artifacts and is a common concern when dealing with accelerating the acquisition time of MR data through under sampling the points of k-space. Figure 2.2 shows an example of "fold-over" artifacts for a decrease of collected points in the k_y direction. A "fold-

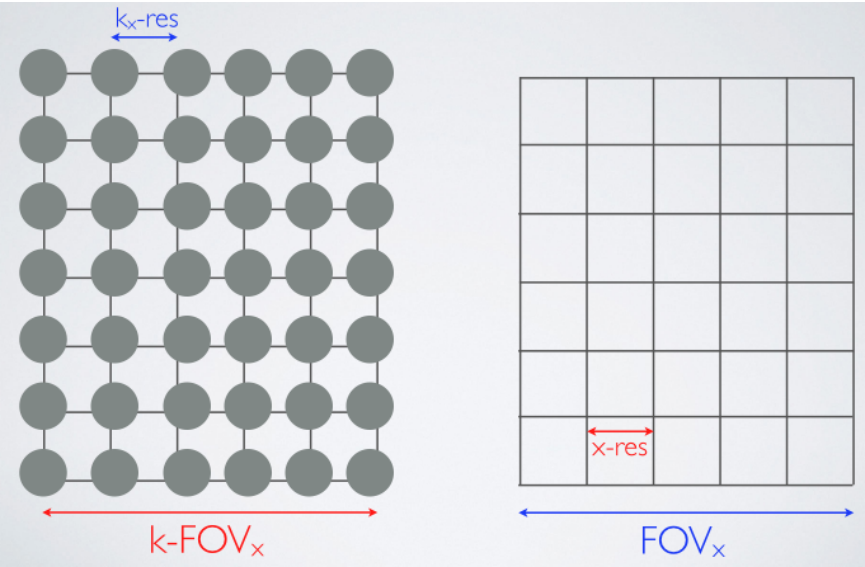

Figure 2.1. k-space is featured on the left and real/image space is on the right. Each grey dot on the left represents a k-space matrix data point and the k_x resolution is determined by the distance (in Hz or ppm) between each dot. The x-resolution in the real space is determined by the size of each box. Think of each box as a pixel on a screen.

over" artifact is one in which the image appears to have been folded over on itself.

The center of k-space holds the highest density of information and contains the contrast of the image while the larger frequencies, near the edge of the k-space matrix, provide the resolution and detail of the image [31]. This is easily understood when one thinks of the classic example of the Fourier Transform of a square wave. To get the sharp edge details, we need to add in higher and higher frequencies, with smaller amplitudes. This corresponds directly to our model of k-space: the brighter the spots, the bigger the amplitudes and the farther from the center, the higher the frequencies used. Thus, we see that the center of k-space holds the contrast information and most of the information, while the edges of k-space hold the finer, detailed information. See Figure 2.3 for a look at a fully sampled k-space and the resulting image after removal of the central region of k-space.

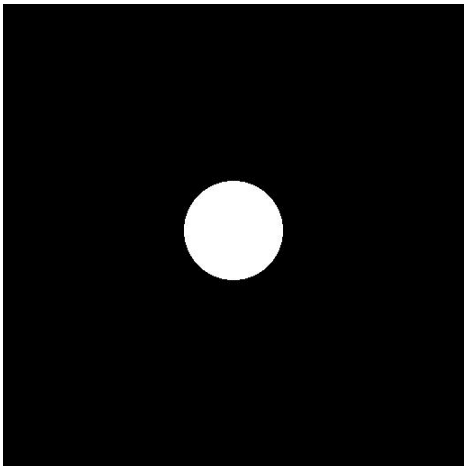

(a) Full FOV

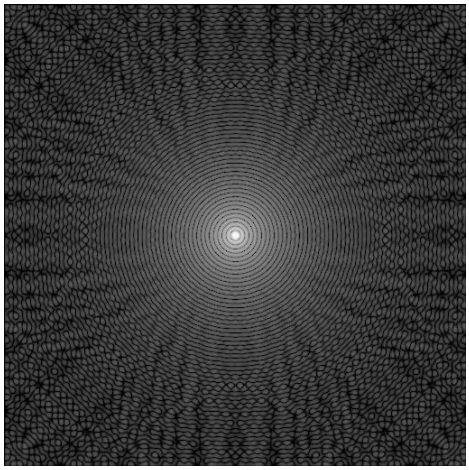

(b) FFT of image in Figure 2.2(a)

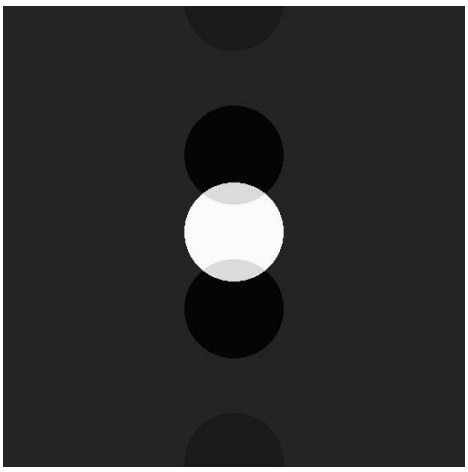

(c) Decreased real/image space FOV

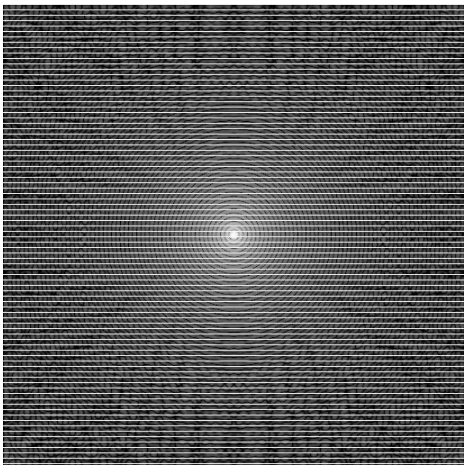

(d) FFT of image in Figure 2.2(a) with periodic removal of k_x lines in k-space

Figure 2.2. When working with MRI's, it is convenient to think of the image as repeating periodically throughout image space. If the data sampling density in the k_y direction is decreased (sampling less k-space points), then the FOV in real space is decreased, causing "fold-over" artifacts. To obtain Figure 2.2(d) every 6th line has been removed from Figure 2.2(b). Once Figure 2.2(d) has been fourier transformed, we obtain Figure 2.2(c) which shows the folder artifacts.

As mentioned in Appendix C, gradients allow us to "travel" through k-space so that the k-space information matrix can be filled in. In particular, the area under

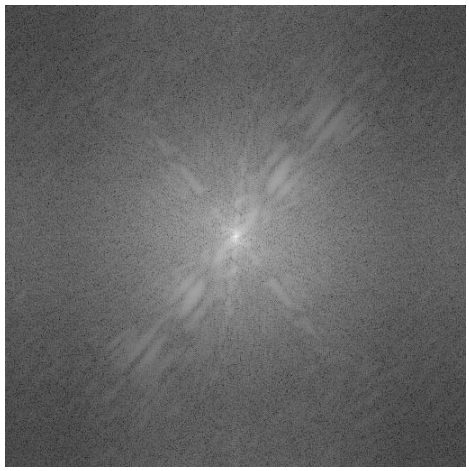

(a) FFT of the liver in Figure 2.3(b)

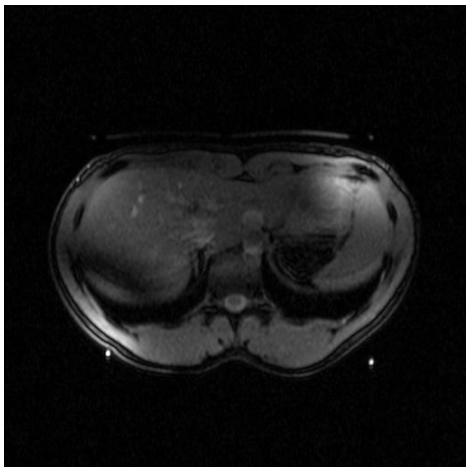

(b) Real Space image of a human liver

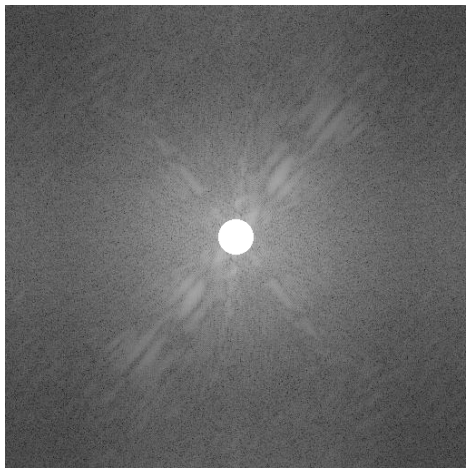

(c) Center region of k-space has been removed

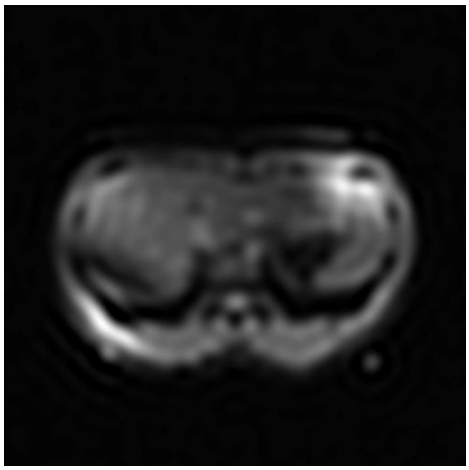

(d) Image of the liver after the center of k-space has been removed

Figure 2.3. A full sampling of k-space as seen in Figure 2.3(b) yields the image of the liver as seen in Figure 2.2(a). The center of k-space is bright and the intensity decreases as we move out from the center. The center holds the most information since it corresponds to the lower frequencies and can be considered the "first order" representations, while the outer edges of k-space holds the finer details, the "higher order" representations. Figure 2.3(c) shows the center of k-space removed, limiting the information held in k-space. We see that the last image, Figure 2.3(d), has been blurred due to the removal of the low frequencies, corresponding to the detail contained within the center of k-space.

the gradient curve will tell the position in k-space. Thus, applying a small gradient for a long time or applying a large gradient for a short time will result in the same movement through k-space. Specifically, two types of gradients are used: the Frequency Encoding Gradient (FEG) and the Phase Encoding Gradient (PEG). More information about these can be found in the Appendix. Typically, the scanner starts in the center of k-space as seen in Figure 2.4. When a negative FEG (G_x) is applied, the scanner has moved in the negative k_x direction. If a positive x gradient had been applied, we would have moved in the positive k_x direction.

A more realistic and useful pulse sequence is shown in Figure 2.5. This is a standard spin-echo sequence in which we flip the magnetization by 90° and then a short time later the nuclei is flipped by 180° obtaining the "echo" signal used to form images. At each point in the k-space matrix, the real and imaginary parts of the complex signal are recorded.

Below are the main points from papers on SMASH, AUTO-SMASH, and GRAPPA [33–35].

2.2 SMASH Review

In a 3D volume, V, the signal $S(k_x, k_y, k_z)$ obtained can be given by:

$$S\left(k_x, k_y, k_z\right) = \iiint_V \mathrm{d}x\,\mathrm{d}y\,\mathrm{d}z\, C(x,y,z)\, e^{-i(k_x x + k_y y + k_z z)}\, \rho\left(x,y,z\right) \tag{2.2}$$

where C is the coil sensitivity for a single coil, ρ is the spatial distribution of the MRS molecules, $k_x = \gamma G_x t_x$, $k_y = \gamma G_y t_y$, and $k_z = \gamma G_z t_z$, γ is the gyromagnetic ratio, and t_x, t_y, and t_z are the times within the magnetic field gradients G_x, G_y, and G_z, respectively. When using a multi-coil array with L coils, the coil sensitivity becomes:

$$C(x,y,z) \rightarrow C_0^{comp}(x,y,z) = \sum_{l=0}^{L} n_l^{(0)} C_l(x,y,z) \tag{2.3}$$

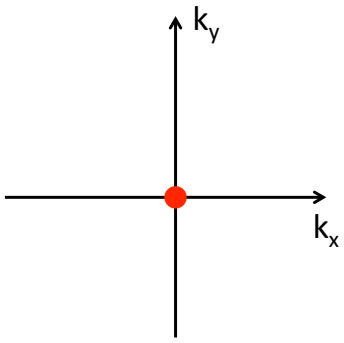

(a) The scanner starts in the center of k-space

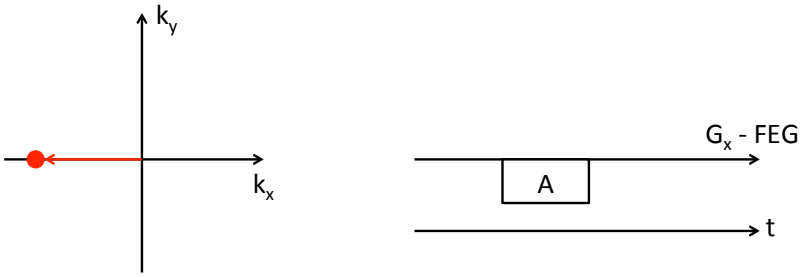

(b) After applying a FEG, the position within the k-space matrix moves in the k_x direction (a negative gradient is shown here) in proportion to the applied strength and time of the applied FEG

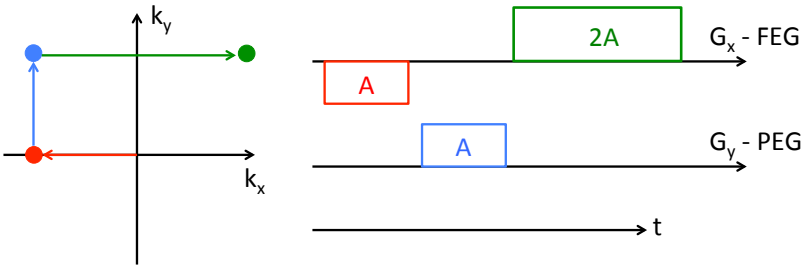

(c) The same ideas can be applied to move through the other Cartesian directions of k-space using both FEG's and PEG's.

Figure 2.4. Movement through the k-space matrix is done with gradients. The position within the matrix depends on the area under the gradient curve, and thus depends on both the strength and duration of the applied gradient. Shown here is one sequence of FEG's and PEG's to move a desired location in the k-space matrix.

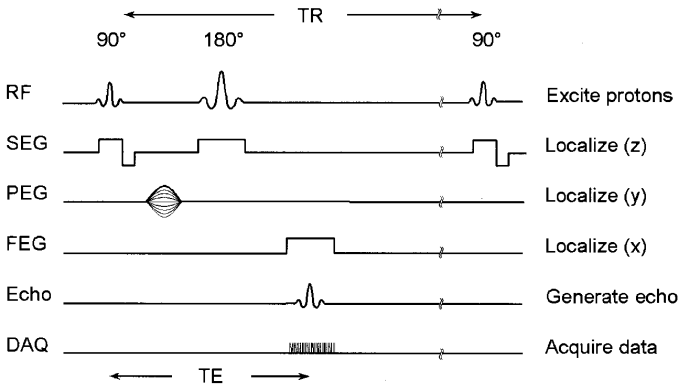

Figure 2.5. The applied PEG and FEG gradients are shown here. During the 90° excitation, the slice gradient is applied simultaneously and allows the appropriate section/slice of nuclei to be excited. The PEG and FEG move through the k-space matrix, filling it with the information from the acquired signal. Here, the FEG is considered the readout gradient and is applied during the echo acquisition to achieve spatial encoding. The PEG, as demonstrated in Figure 2.4, moves through the k_y direction and has different strengths applied, seen as multiple amplitudes on the PEG line. For each amplitude, a different acquisition is performed. This figure obtained from [31].

where $C_l(x, y, z)$ is the spatial sensitivity for one coil C_l, $C_0^{comp}(x, y, z)$ is the total spatial sensitivity for the whole array, and $n_l^{(0)}$ are the weights for each coil associated with its spatial proximity to the acquired signal. The closer the coil to the real image space signal, the larger the weight associated with the coil for that signal. These weights can be *chosen* to give a certain composite sensitivity, for example, a uniform spatial sensitivity. The SMASH technique uses these weights to build the composite sensitivity so that the spatial sensitivity of the coil array is sinusoidal:

$$\begin{aligned} C_m^{comp}(x, y, z) &= \sum_{l=0}^{L} n_l^{(m)} C_l(x, y, z) \\ &= C_0^{comp}(x, y, z) e^{im\Delta k_y y} \end{aligned} \tag{2.4}$$

where m (an integer) is the m^{th} order spatial harmonic across the volume of interest. $C_0^{comp}(x, y, z)$ is the original spatial coil sensitivity map without harmonic weighting.

Δk_y is the minimal k-space interval between points corresponding to the desired FOV, $\Delta k_y = 2\pi/$ FOV. With this, the acquired composite signal becomes:

$$S_m^{comp}(k_x, k_y, k_z) = \iiint_V \mathrm{d}x\,\mathrm{d}y\,\mathrm{d}z\, C_m^{comp}(x, y, z)\, e^{-i(k_x x + k_y y + k_z z)}\, \rho(x, y, z) \tag{2.5}$$

Substituting in for the composite coil sensitivity, we obtain:

$$S_m^{comp}(k_x, k_y, k_z) = \iiint_V \mathrm{d}x\,\mathrm{d}y\,\mathrm{d}z\, C_0^{comp}(x, y, z)\, e^{-i(k_x x + (k_y - m\Delta k_y) y + k_z z)}\, \rho(x, y, z) \tag{2.6}$$

The SMASH technique then requires that we find the weights $n_l^{(m)}$ using coil sensitivity maps. In the next iteration of this technique, it is shown that the weights can be automatically extracted from additionally acquired data.

2.3 AUTO-SMASH Review

The main difference between the SMASH and AUTO-SMASH techniques is that with AUTO-SMASH, the weights are automatically generated by acquiring additional lines within k-space. These small number of additional k-space lines are called the auto-calibration signals (ACS). The ACS lines are used to fit the weights from the remaining acquired data during a scan.

Without an m^{th} order harmonic generation (a zeroth order), the composite signal at k-space location $(k_x, k_y - m\Delta k_y, k_z)$ is given by:

$$S^{comp}(k_x, k_y - m\Delta k_y, k_z) = \sum_{l=1}^{L} n_l^{(0)} S_l^{ACS}(k_x, k_y - m\Delta k_y, k_z) \tag{2.7}$$

Where the composite signal is just the summation of the individual coil ACS signals, from the same location in k-space, $(k_x, k_y - m\Delta k_y, k_z)$. Here, each coil is weighted the same, as indicated by the weights, $n_l^{(0)}$.

Adding the weights, $n_l^{(m)}$, effectively produces an m^{th} order harmonic. This effective harmonic generation offsets the signal used to make the same composite signal

at a location $(k_x, k_y - m\Delta k_y, k_z)$ to a new k-space location (k_x, k_y, k_z), an offset of $m\Delta k_y$ in the k_y direction of k-space:

$$S^{comp}(k_x, k_y - m\Delta k_y, k_z) = \sum_{l=1}^{L} n_l^{(m)} S_l(k_x, k_y, k_z) \tag{2.8}$$

By comparing Equation 2.7 and Equation 2.8 we get the relation:

$$\sum_{l=1}^{L} n_l^{(m)} S_l(k_x, k_y, k_z) = \sum_{l=1}^{L} n_l^{(0)} S_l^{ACS}(k_x, k_y - m\Delta k_y, k_z) \tag{2.9}$$

Thus, we are now able to take our extra ACS lines and use them to fit the required $n_l^{(m)}$ weights. This is done by acquiring composite signals from one line in k-space, $S^{comp}(k_x, k_y, k_z)$, and an ACS line at another location a distance of $m\Delta k_y$ in the k_y direction of k-space $S_{ACS}^{comp}(k_x, k_y - m\Delta k_y, k_z)$. These lines now obey the relation in (2.9):

$$S_{ACS}^{comp}(k_x, k_y - m\Delta k_y, k_z) = \sum_{l=1}^{L} n_l^{(m)} S^{comp}(k_x, k_y, k_z) \tag{2.10}$$

Where the only unknowns in (2.10) are the weights, $n_l^{(m)}$, thus allowing us to solve for them. We can then use these same weights to fill out our k-space matrix since the harmonic relations between k-space points will not change throughout k-space and all spatial harmonics *produced* by the weights $n_l^{(m)}$ are integer multiples of the fundamental frequency of the k-space spacing, Δk_y.

2.4 GRAPPA

Generalized Autocalibrating Partially Parallel Acquisitions (GRAPPA) is a technique that has been used in magnetic resonance imaging for 10 years [35]. Recently, our group has been able to adapt GRAPPA towards MRS in both 1D and 2D and I built on this concept to take GRAPPA into the 3rd dimension for ^{31}P MRS.

GRAPPA builds off the ideas of AUTO-SMASH by expanding the information used to fit the lines and solve for the weights, $n_l^{(m)}$. AUTO-SMASH used the information from only one coil to fit a line of data to that same coil. GRAPPA expands

this by incorporating information from all coils to fit the weights, $n_l^{(m)}$. This additional information allows for a much improved fit. The governing equation used for GRAPPA is the following:

$$S_j(k_x, k_y - m\Delta k_y, k_z) = \sum_{l=1}^{L} \sum_{b=0}^{N_b-1} n(j, b, l, m) S_l(k_x, k_y - bA\Delta k_y, k_z) \tag{2.11}$$

Where j represents the coil of interest, at position in k-space $(k_x, k_y - m\Delta k_y, k_z)$, A represents the acceleration factor, and N_b is the number of blocks used for the reconstruction. A block is defined as a single acquired line and (A-1) missing lines in k-space. For this work, we used an acceleration factor of 2, thus making A=2 and defining a block as a single acquired line and a single missing line. The signals, S_j and S_l, and weights, n, follow the same concepts as the ones used in AUTO-SMASH. We can see from Equation 2.11 that the signal reconstructed in each coil is found using the information from all of the coils in the array.

Table 2.1
Sample ACS region of k-space matrix with known signals indicated as S_1 through S_{15}. These known signals are used to solve for the reconstruction weights used in the GRAPPA reconstruction. This would be the grey voxels indicated in Figure 2.6

Sample ACS Kernel of Central k-space Region		
S_1	S_2	S_3
S_4	S_5	S_6
S_7	S_8	S_9
S_{10}	S_{11}	S_{12}
S_{13}	S_{14}	S_{15}

Finding the weights is a simple matter of using the following equation with the known signals from the central k-space region, as shown in Table 2.4:

$$S_1 w_1 + S_7 w_2 = S_4 \tag{2.12}$$

The only unknowns in Equation 2.12 are the weights since the ACS region is fully sampled. If we repeat this scheme for each possible combination, we obtain 8 additional equations in which we can determine the weights, w_1 and w_2. The other 8 equations are:

$$\begin{aligned} S_2w_1 + S_8w_2 &= S_5 & \qquad S_3w_1 + S_9w_2 &= S_6 \\ S_4w_1 + S_{10}w_2 &= S_7 & \qquad S_5w_1 + S_{11}w_2 &= S_8 \\ S_6w_1 + S_{12}w_2 &= S_9 & \qquad S_7w_1 + S_{13}w_2 &= S_{10} \\ S_8w_1 + S_{14}w_2 &= S_{11} & \qquad S_9w_1 + S_{15}w_2 &= S_{12} \end{aligned} \tag{2.13}$$

This gives an overdetermined system of equations which allows for the acquisition of more accurate weights to be determined. This process is then repeated for each coil, for each data point within the FID, and then all weights are saved into a weights matrix. These weights are then used to reconstruct unknown, or unacquired, signals in the following way.

$$S_{top}w_1 + S_{bottom}w_2 = U_1 \tag{2.14}$$

	0	1	2	3	4	5	6	7	8	9	10	11	12	13	14	15
0	0	0	0	0	0	0	0	0	0	0	0	0	0	0	0	0
1	0	0	0	0	0	0	0	0	1	0	0	0	0	0	0	0
2	0	0	0	0	0	1	2	2	2	2	2	1	0	0	0	0
3	0	0	0	0	2	3	5	6	6	6	5	3	2	0	0	0
4	0	0	0	2	4	6	9	11	12	11	9	6	4	2	0	0
5	0	0	1	3	6	11	15	18	19	18	15	11	6	3	1	0
6	0	0	2	5	9	15	20	23	25	23	20	15	9	5	2	0
7	0	0	2	6	11	18	23	27	29	27	23	18	11	6	2	0
8	0	1	2	6	12	19	25	29	30	29	25	19	12	6	2	1
9	0	0	2	6	11	18	23	27	29	27	23	18	11	6	2	0
10	0	0	2	5	9	15	20	23	25	23	20	15	9	5	2	0
11	0	0	1	3	6	11	15	18	19	18	15	11	6	3	1	0
12	0	0	0	2	4	6	9	11	12	11	9	6	4	2	0	0
13	0	0	0	0	2	3	5	6	6	6	5	3	2	0	0	0
14	0	0	0	0	0	1	2	2	2	2	2	1	0	0	0	0
15	0	0	0	0	0	0	0	0	1	0	0	0	0	0	0	0

Figure 2.6. A 2D schematic for k-space under sampling. The red elements are k-space positions not sampled, the white elements are sampled, the grey central area is the ACS kernel used to determine the weights to be used to reconstruct data. First the k_y direction is reconstructed, followed by the k_x direction. The numbers indicate the number of averages that the particular element is sampled.

This would then give us the unknown signal, U_1. With this method, missing k-space information matrix elements can be reconstructed. Figure 2.6 shows a layout of 2D undersampling with the undersampled elements colored as red, the sampled elements as white, and the ACS kernel as grey. The yellow elements in the outer regions of k-space are not sampled as this is a weighted scheme, which samples the central region of k-space more heavily than the outer edges.

The previous steps can be more compactly and elegantly understood by using matrix notation:

$$\underline{S^{comp}}(k_x, k_y, k_z) = \underline{n^{(m)}}\ \underline{S^{comp}_{ACS}}(k_x, k_y - \Delta k_y, k_z) \tag{2.15}$$

where $\underline{S^{comp}_{ACS}}$ stands for the matrix that contains the ACS lines acquired during the scan and $\underline{S^{comp}}$ stands for the matrix that contains the composite signal at the point of interest. To solve for the weights matrix, we use the pseudo-inverse solution:

$$\underline{n^{(m)}} = \underline{S^{comp}}\ \underline{S^{comp,H}_{ACS}} \left(\underline{S^{comp}_{ACS}}\ \underline{S^{comp,H}_{ACS}}\right)^{-1} \tag{2.16}$$

where the H in the superscript of $\underline{S^{comp,H}_{ACS}}$ represents the Hermitian conjugate of $\underline{S^{comp}_{ACS}}$. With this solution we obtain a matrix of weights that can then be used to solve for the unknown, or uncollected, data throughout the rest of the k-space data matrix, outside of the ACS region. It is worth noting that for Cartesian and other lattice based sampling schemes, the weights in the appropriate direction are shift invariant [36].

3. Materials and Methods

3.1 Materials

3.1.1 ^{31}P/^{1}H Coil and Scanner

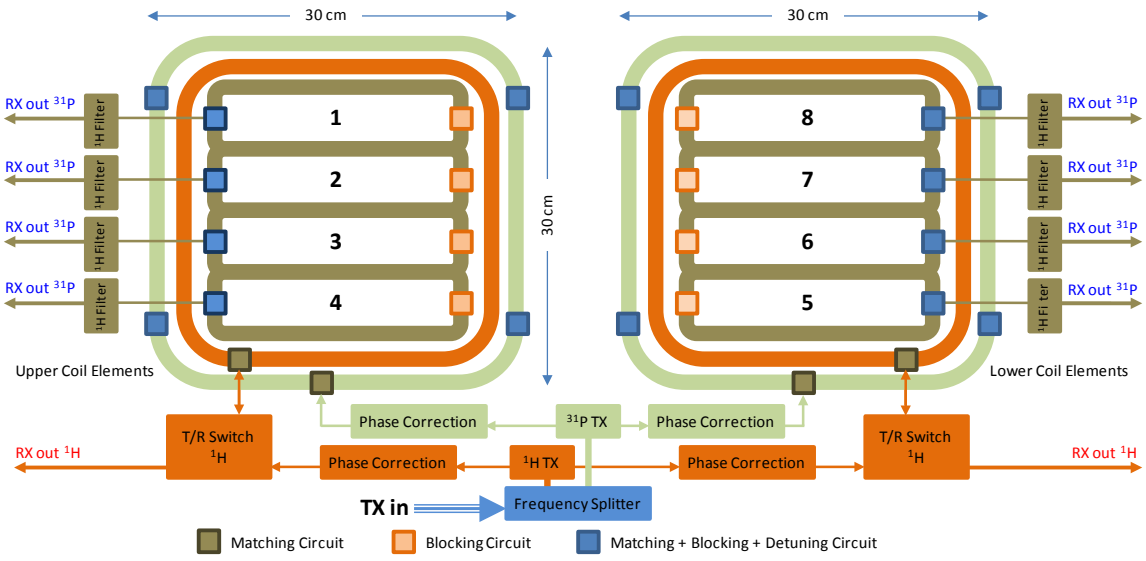

Figure 3.1. A schematic of the dual tuned ^{1}H/^{31}P coil is shown in the first figure. The eight individual ^{31}P RX coils can be seen as well as the single ^{31}P TX coil and the single TX/RX ^{1}H coil.

Our group has designed an 8-channel, dual-tuned, phased-array coil and worked with Stark Contrast MRI Coils Research from Erlangen, Germany to have it built. The coil consists of two plates to be placed on the back and chest of the patient, wrapping around the torso. Each plate has one ^{1}H transmit (TX)/receive (RX) coil, one ^{31}P TX coil, and 4 ^{31}P RX coils. The ^{1}H TX/RX coil has an area of approximately 27x30 cm^2, the ^{31}P TX coils have an area of approximately 30x30 cm^2, and the 4 ^{31}P RX coils have a total area of approximately 24x20 cm^2 in each plate [20]. This

gives us a total of 8 ^{31}P RX coils which allows us to do parallel acquisitions. See Figure 3.1 for a schematic of the coil used. Not shown in this figure are the fiducial markers that have been placed onto both plates of the coil. These fiducial markers can be seen in Figure 3.2 and consist of two square tubes on each plate filled with 1M phenylphosphonic acid (PPA) and water. These markers appear in the anatomical images as the four bright spots outside the volume of interest (seen in Figure 3.2) and are used as patient placement reproducibility markers for the localizing images and as a spectral reference signal.

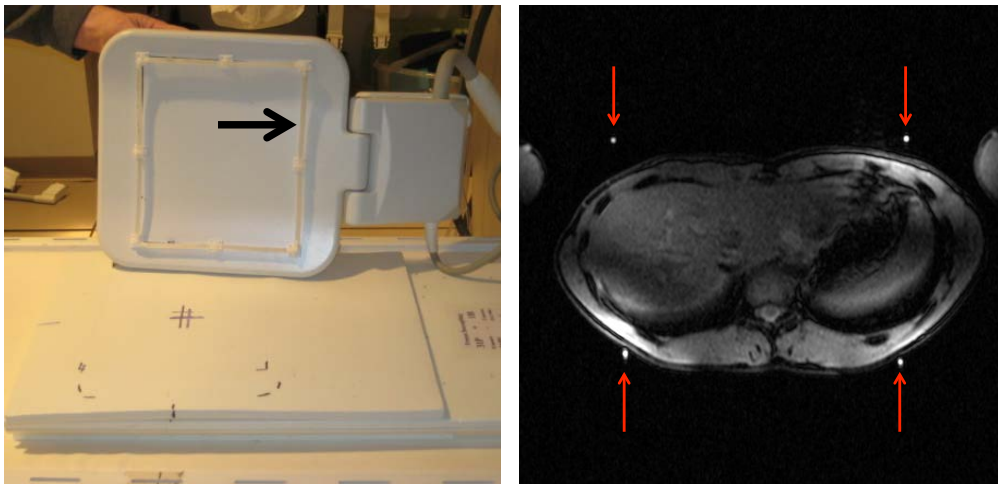

(a) Fiducial marker tube indicated by the solid black arrow

(b) Fiducial markers as seen in the MRI

Figure 3.2. The first figure shows the fiducial marker located on the top plate with the black arrow (note that the identical bottom fiducial marker is located under the pad in the bottom of the image and is not shown). This image was taken from [21]. The second figure shows how the markers appear in the anatomical localizing images as the four bright dots indicated by the red arrows.

All data acquired for this study was obtained on a Siemens MAGNETOM Tim Trio 3T Scanner [37]. The scanner is located in Indianapolis, IN at the Indiana University School of Medicine. This particular scanner has the capability to do multi-nuclear scans, allowing us to acquire ^{31}P MRS data as well as ^{1}H anatomical images .

3.1.2 Developmental Phantoms

Though numerous phantoms exist for development purpose of this project, focus will be applied to just one primary phantom. This phantom, codenamed Polly, was filled with distilled water along with 75 millimole per liter NaCl and 0.04 grams per liter $NiCl_2$ as to satisfy the ACR recommendations of in-vivo simulations [38] and to reduce the T_1 relaxation time of ^{31}P [39], respectively.

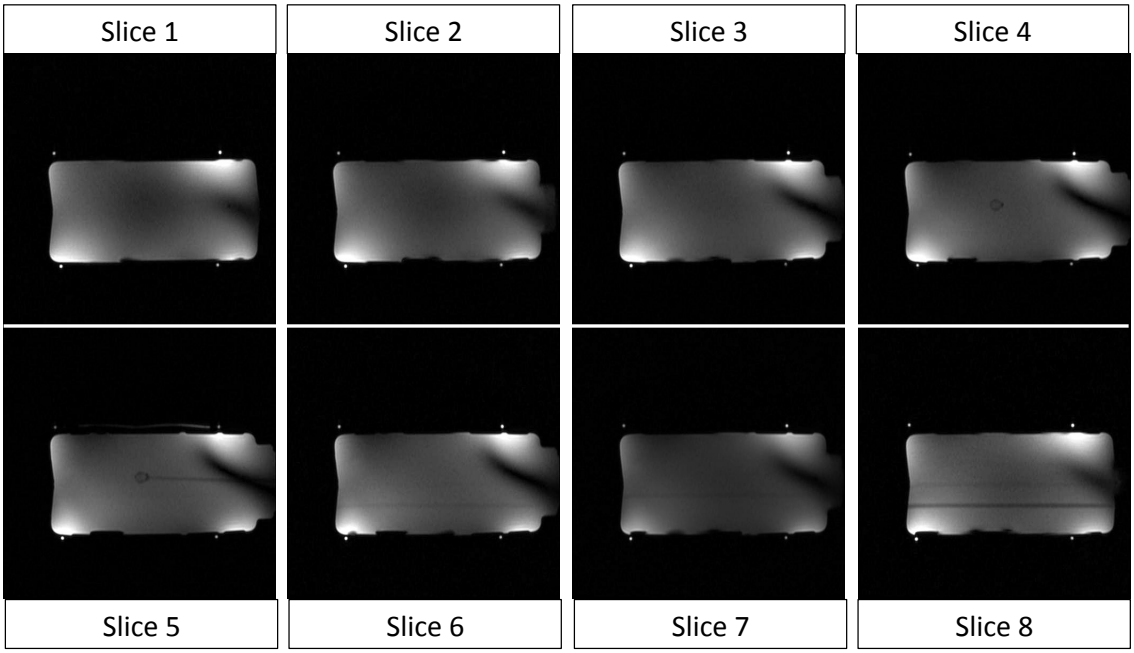

Figure 3.3. The Polly phantom, seen from the axial view in eight MRI images.

The Polly phantom contains a single, small insert 1.85 centimeters in diameter. This insert was filled with 1 mole per liter Pi solution and can be seen in Figure 3.3. Polly was created for a test of the point spread function (PSF) of our coil and the sequence and therefore the insert extends over one single (nominal) voxel. Polly has another added benefit of yielding a very simple spectrum to analyze and quantify. Since Polly contains a single insert with a single metabolite, Pi, the foldover artifacts created with undersampling of the k-space matrix are more easily understood. Figure

3.3 shows that the insert is only located in the central slices, and these are the ones that will be presented in this work. Due to voxel bleeding, slices 3 through 6 will be analyzed.

3.1.3 Healthy Volunteers

For this study, we have so far acquired the consent of two adult, healthy, male volunteers to test the in-vivo feasibility of this 3D GRAPPA sequence. The volunteers will be denoted as HVOL1, HVOL2, etc. The average age, weight, and height of the volunteers were 26.5 years, 165 pounds, and 5 feet and 11 inches. Eight slices of

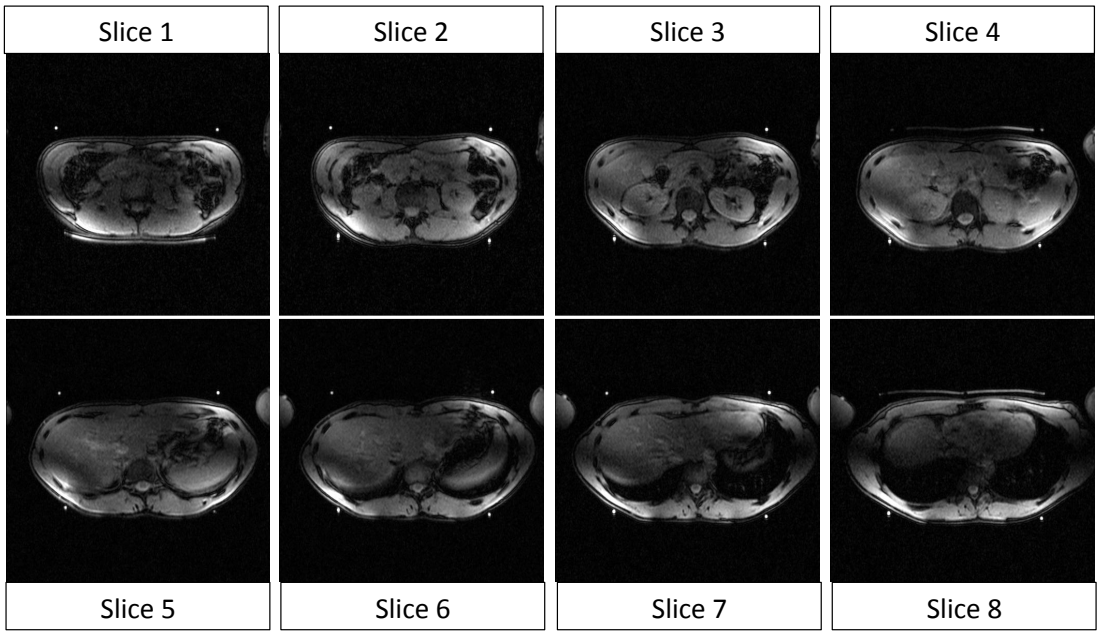

Figure 3.4. Eight axial images of the first volunteer, HVOL1. Note that the liver is easily visible in slices 4 through 7.

HVOL1 are shown in Figure 3.4. The liver is easily visible in slices 4 through 7, the bottom of the heart is seen in slice 8, while the kidneys are seen in slices 2 through 4, to name a few anatomical features. Eight slices of HVOL2 are shown in Figure 3.5. The same anatomical features are visible in these slices.

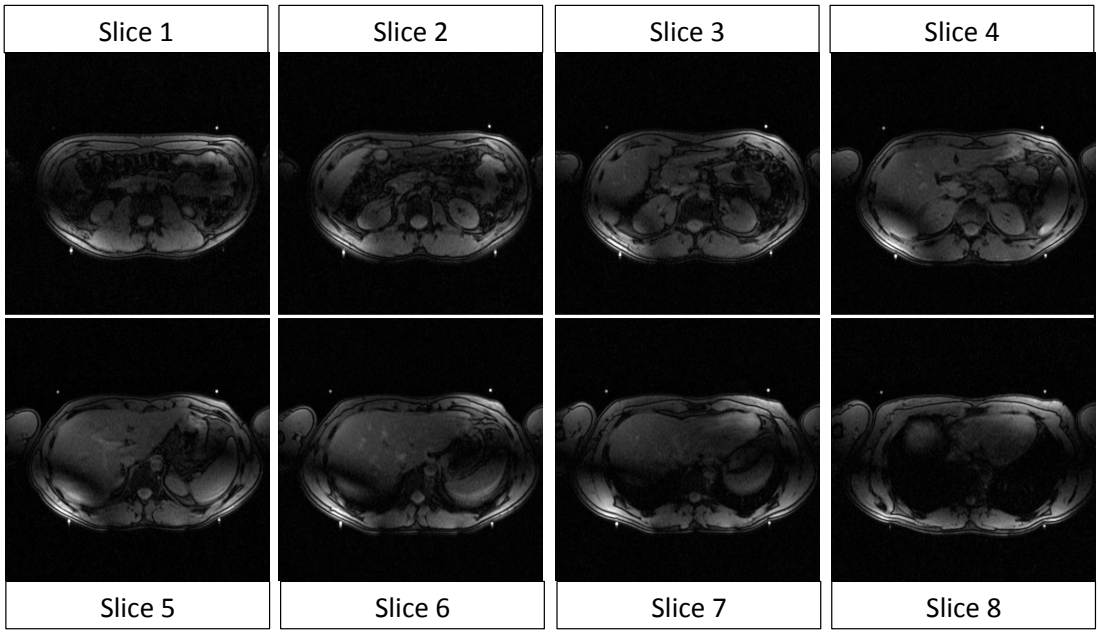

Figure 3.5. Eight axial images of the second volunteer, HVOL2. Note that the liver is easily visible in slices 4 through 7.

In both volunteers, the axial view is seen as if the patient were laid in the supine position, with the back being on the bottom of the image and the patients right side being on the left side of the image, as if looking at the volunteer from the feet up. In both sets, the back and abdominal muscles are visible on the anterior and posterior sides of the volunteer. These will later be used for their PCr concentrations to analyze the foldover artifacts of the GRAPPA reconstructions.

3.2 Data Acquisition

All data has been acquired on a 3T Siemens whole body scanner (Siemens Tim Trio). The eight-channel, dual-tuned $^{31}P/^{1}H$ coil developed by our group [20] was used for all data acquisitions. The acquisition protocol for ^{1}H imaging contains pre-acquisition localization and post-acquisition analysis images to visually test for motion

during the ^{31}P MRSI scan. ^{31}P MRSI data was obtained by using a 3D free-induction-decay (FID) sequence, with parameters matching those shown in Table 3.2.

Table 3.1
List of scan parameters for clinical 3D ^{31}P MRS acquisition

Parameter	**Value**
TR	1000 ms
TE	2.3 ms
Sampling Type	Weighted
N_{avg}	12
Phase Encoding Steps	16 x 16 x 8
FOV	40 x 40 x 20 cm^3
Slice Thickness	2.5 cm
No. of Slices	2.5 cm
Nominal Voxel Size	15.63 cm^3
Voxels per Scan	2048
Total Volume	3200 cm^3
Total Scan Time	31 min 48 sec

In order to obtain the undersampled data, new code was written for the MRI scanner. The easiest and most robust way to implement the new sequence was to take advantage of the "Sequence/Special" tab, provided by Siemens software. This special tab (seen in Figure 3.6) is available with C++ macros and was successfully introduced into our experiments to provide an integrated protocol that allows us to undersample and/or reconstruct in any of the Cartesian coordinate directions. Table 3.2 shows the protocol parameters for the fully sampled, 1 dimensional, and 2 dimensional (in the third direction; i.e., 2D undesampling per slice) directions. Notice that the acquisition time decreases for each subsequent undersampling scheme.

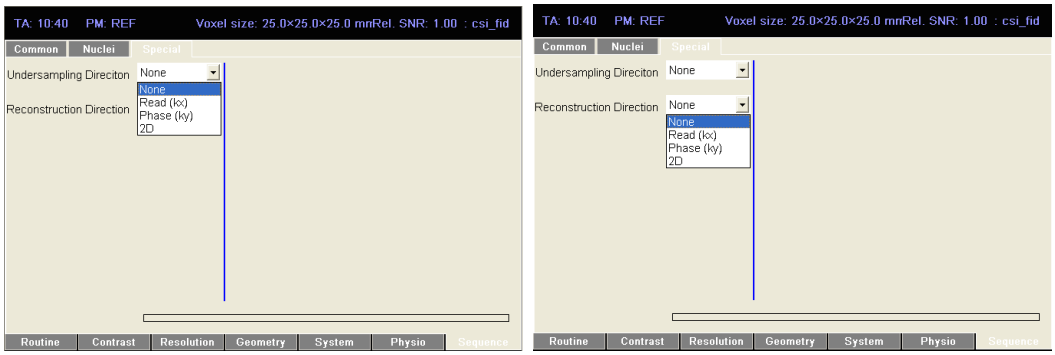

(a) Implementation of combined undersampling protocols

(b) Implementation of combined reconstruction protocols

Figure 3.6. Combining protocols for various undersampling and reconstruction schemes

Table 3.2
List of scan parameters for GRAPPA 3D ^{31}P MRS acquisitions

Parameter	**Fully**	**1D**	**2D**
Sampling Type	Weighted	Weighted, 1D US	Weighted, 2D US
TR	1000 ms	1000 ms	1000 ms
TE	2.3 ms	2.3 ms	2.3 ms
N_{avg}	12	12	12
Phase Encoding Steps	16 x 16 x 8	16 x 16 x 8	16 x 16 x 8
FOV	40 x 40 x 20 cm^3	40 x 40 x 20 cm^3	40 x 40 x 20 cm^3
Slice Thickness	2.5 cm	2.5 cm	2.5 cm
No. of Slices	8	8	8
Nominal Voxel Size	15.63 cm^3	15.63 cm^3	15.63 cm^3
Voxels per Scan	2048	2048	2048
Total Volume	3200 cm^3	3200 cm^3	3200 cm^3
Total Scan Time	31 min 48 sec	17 min 12 sec	10 min 04 sec

3.2.1 3D GRAPPA

Figure 3.7 shows two possible sampling schemes from one slice of k-space. Figure 3.7(a) shows the full sampling scheme of k-space, acquiring each point with the same number of averages. Figure 3.7(b), on the other hand, shows a weighted acquisition scheme, decreasing in averages the farther away from the center of k-space we move. The weighting factors in the weighted acquisition slice derive from the equation:

$$w(k_x, k_y, k_z) = \frac{1}{2} N_{avg} \left(1 + \cos\left(\pi d\right)\right) \tag{3.1}$$

where d is the normalized distance away from the k-space center. Similarly to the 2D slices seen in Figure 3.7, we can map out the weighted acquisition for a 3D data set, which is just a set of adjacent 2D slices. Figure 3.8 shows the different slices for a weighted, eight slice, 3D acquisition. Notice that the eighth slice of k-space has no information. The reason for this is the even number of slices. When weighting factors get calculated, they are symmetrical around the center of k-space, slice four in this example. Similarly, with an even number of voxels in each column and row of the k-space matrix, the first column and row of each slice is set with a zero weighting and are thus not acquired. With this initial information, a plan can be devised to optimize the acquisition scheme of 3D k-space and improve the SNR per unit time of data acquisition.

Figure 3.9 shows the undersampling scheme used in this study. The central slice (Slice 4) contains the ACS kernel used to find the weights for GRAPPA reconstruction, shown as grey. The rest of the slices continue the general, weighted sampling outline shown in Figure 3.8, shown as white. The red voxels shown in Figure 3.9 indicate non-sampled k-space elements, thus reducing the time needed for a scan.

Figure 3.10 shows the reconstruction process of the k-space matrix of the fourth slice of an eight slice acquisition. This figure shows that the reconstruction is done in different steps. Due to the size and shape of the ACS kernel we must reconstruct in the k_x direction first, skipping every other row followed by reconstruction in the k_y direction. Note in this figure that the reconstructed elements have been colored

	0	1	2	3	4	5	6	7	8	9	10	11	12	13	14	15
0	12	12	12	12	12	12	12	12	12	12	12	12	12	12	12	12
1	12	12	12	12	12	12	12	12	12	12	12	12	12	12	12	12
2	12	12	12	12	12	12	12	12	12	12	12	12	12	12	12	12
3	12	12	12	12	12	12	12	12	12	12	12	12	12	12	12	12
4	12	12	12	12	12	12	12	12	12	12	12	12	12	12	12	12
5	12	12	12	12	12	12	12	12	12	12	12	12	12	12	12	12
6	12	12	12	12	12	12	12	12	12	12	12	12	12	12	12	12
7	12	12	12	12	12	12	12	12	12	12	12	12	12	12	12	12
8	12	12	12	12	12	12	12	12	12	12	12	12	12	12	12	12
9	12	12	12	12	12	12	12	12	12	12	12	12	12	12	12	12
10	12	12	12	12	12	12	12	12	12	12	12	12	12	12	12	12
11	12	12	12	12	12	12	12	12	12	12	12	12	12	12	12	12
12	12	12	12	12	12	12	12	12	12	12	12	12	12	12	12	12
13	12	12	12	12	12	12	12	12	12	12	12	12	12	12	12	12
14	12	12	12	12	12	12	12	12	12	12	12	12	12	12	12	12
15	12	12	12	12	12	12	12	12	12	12	12	12	12	12	12	12

(a) Full k-space acquisition; 12 averages per element

	0	1	2	3	4	5	6	7	8	9	10	11	12	13	14	15
0	0	0	0	0	0	0	0	0	0	0	0	0	0	0	0	0
1	0	0	0	0	0	0	0	0	1	0	0	0	0	0	0	0
2	0	0	0	0	0	1	1	1	2	1	1	1	0	0	0	0
3	0	0	0	0	1	2	2	3	3	3	2	2	1	0	0	0
4	0	0	0	1	2	3	4	5	5	5	4	3	2	1	0	0
5	0	0	1	2	3	5	6	7	8	7	6	5	3	2	1	0
6	0	0	1	2	4	6	8	9	10	9	8	6	4	2	1	0
7	0	0	1	3	5	7	9	11	11	11	9	7	5	3	1	0
8	0	1	2	3	5	8	10	11	12	11	10	8	5	3	2	1
9	0	0	1	3	5	7	9	11	11	11	9	7	5	3	1	0
10	0	0	1	2	4	6	8	9	10	9	8	6	4	2	1	0
11	0	0	1	2	3	5	6	7	8	7	6	5	3	2	1	0
12	0	0	0	1	2	3	4	5	5	5	4	3	2	1	0	0
13	0	0	0	0	1	2	2	3	3	3	2	2	1	0	0	0
14	0	0	0	0	0	1	1	1	2	1	1	1	0	0	0	0
15	0	0	0	0	0	0	0	0	1	0	0	0	0	0	0	0

(b) Weighted acquisition

Figure 3.7. A fully sampled k-space acquisition is a uniform sampling over all of k-space. A weighted acquisition is one in which the center of k-space is sampled more heavily than the edges.

white with red zeroes. The elements in red were not reconstructed due to being on the outer edges of the k-space elements.

One thing to note that can be seen in Figure 3.10 is that we obtain *more* elements after the reconstruction. This is because the reconstruction method looks through the k-space matrix element by element for missing elements that have information in the spaces next to it. If there are adjacent elements that have data, either from the acquisition or the previous reconstruction, then it will reconstruct data at that point without the acquired data. This may seem counterintuitive at first, but since we have established that the weights allow us to reconstruct data based on their offset from the element of interest, this does not hurt the results, but instead may enhance them.

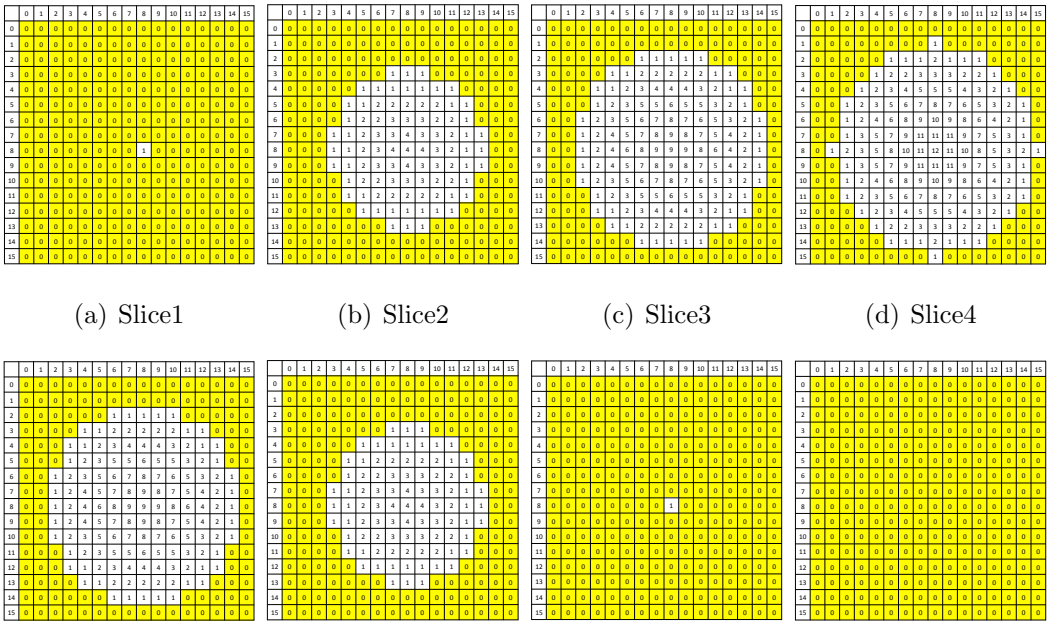

(a) Slice1 (b) Slice2 (c) Slice3 (d) Slice4

(e) Slice5 (f) Slice6 (g) Slice7 (h) Slice8

Figure 3.8. A fully sampled k-space acquisition is a uniform sampling over all of k-space. Here, we see a fully-weighted acquisition, one in which the center of k-space is sampled more heavily than the edges. The center of k-space is found in the fourth slice. The first row shows the first four slices while the second row shows the last 4 slices.

3.3 Quantification

Data was quantified using the AMARES (Advanced Method for Accurate, Robust, and Efficient Spectral fitting of MRS data with use of prior knowledge) routine in jMRUI (Java-based Magnetic Resonance User Interface) [40, 41]. The AMARES package works in the time-domain and fits the FID by minimizing the difference between the data and the fitted model. It allows us to incorporate fixed or absolute prior knowledge (frequency shifts, linewidths, amplitudes, etc.) about the data to minimize the time needed for quantification [42]. AMARES fits the data and gives the following results from the fit: amplitude, frequency position (in ppm), linewidth, phases, and errors, in the form of Cramer-Rao Lower Bounds (CRLB), on each pa-

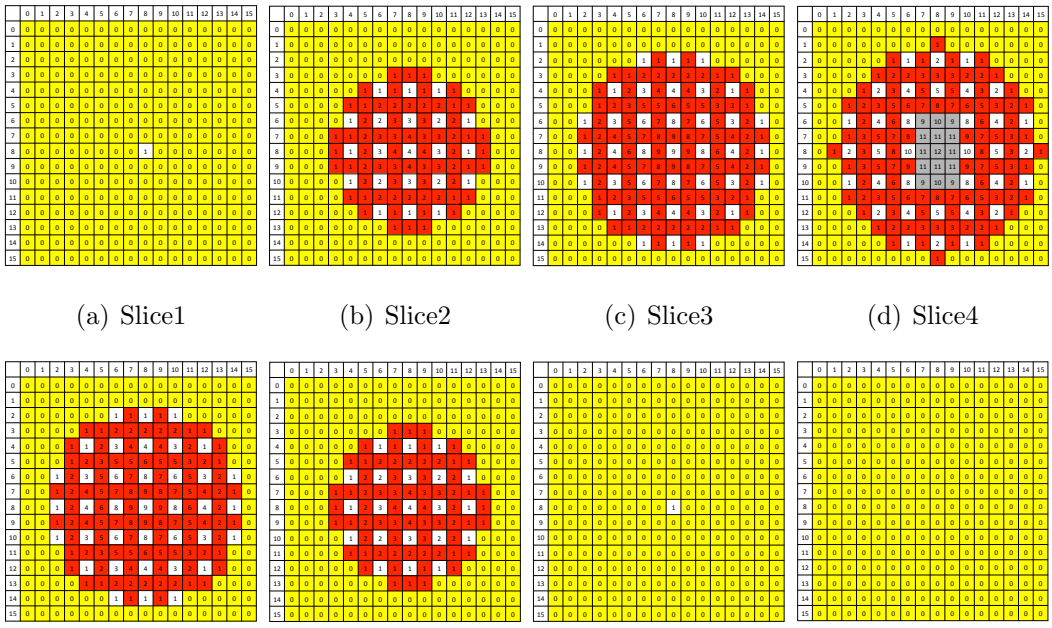

(a) Slice1 (b) Slice2 (c) Slice3 (d) Slice4

(e) Slice5 (f) Slice6 (g) Slice7 (h) Slice8

Figure 3.9. Undersampling k-space in two dimensions for every slice. The yellow voxels indicate unsampled k-space elements, the white voxels indicate the k-space elements that were sampled, and the red voxels indicate elements that would normally have been sampled but were not due to the undersampling scheme introduced with this GRAPPA reconstruction. It is because of these unsampled averages that a faster scan time can be achieved.

rameter [43]. It is worth noting a point of terminology here: the amplitude fitted by jMRUI is *not* the amplitude of the spectroscopy peak, but instead is the amplitude of the first FID data point to be fit. This amplitude is proportional to the concentration of the metabolite of interest, and thus is more closely related to the area under the spectroscopic peak than the height. Before the spectra can be accurately quantified, preprocessing procedures must be applied to filter out artifacts and noise and to correct for field inhomogeneities and frequency shifts. These steps include removal of the PPA reference peak, removal of the β-ATP peak to be used as a reference marker for field inhomogeneities, phase corrections, and apodization to improve the SNR. The before and after results can be seen in Figure 3.11.

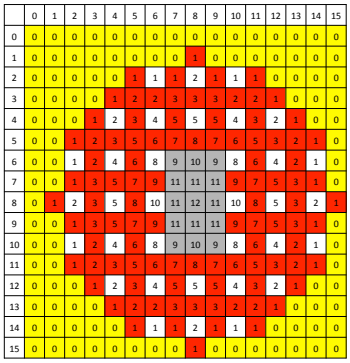

(a) 2D undersampled slice of k-space

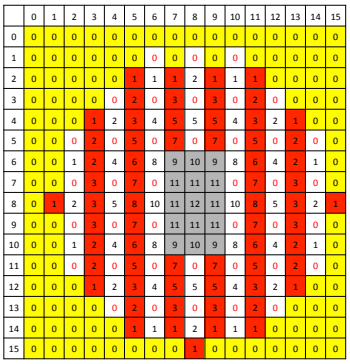

(b) 2D undersampling with kx elements reconstructed

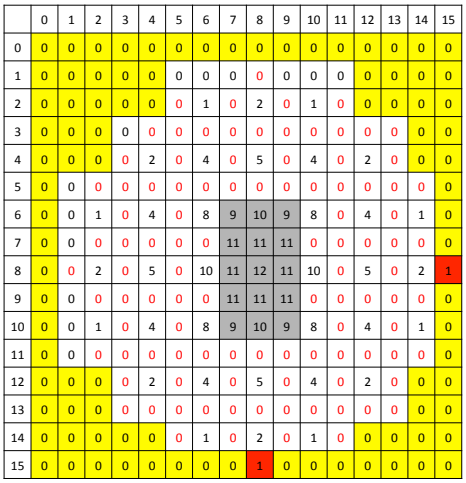

(c) 2D undersampling with elements reconstructed

Figure 3.10. A 2D undersampled k-space is shown in Figure 3.10(a) while k_x reconstruction step is shown in Figure 3.10(b), after some elements have been reconstructed. Grey voxels indicate the central ACS kernel, yellow voxels indicate unsampled elements due to weights, red voxels indicate elements that would normally have been sampled but were skipped during the GRAPPA acquisition, and the white voxels indicate acquired or reconstructed elements.

Once the preprocessing is complete, then the data is quantified using AMARES where a fit is produced as mentioned before for each desired voxel of interest. The result of the fitting is shown in Figure 3.12 where the bottom spectrum shows the

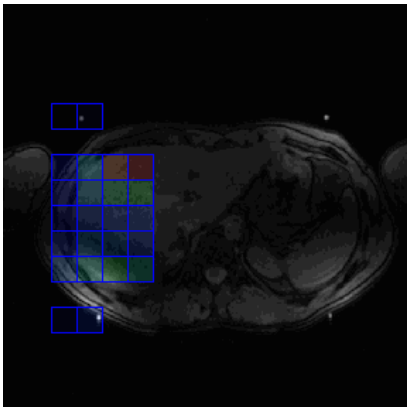

(a) Anatomical image with selected voxels shown

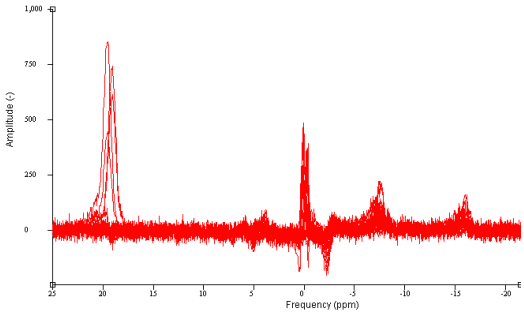

(b) Spectrum before the preprocessing

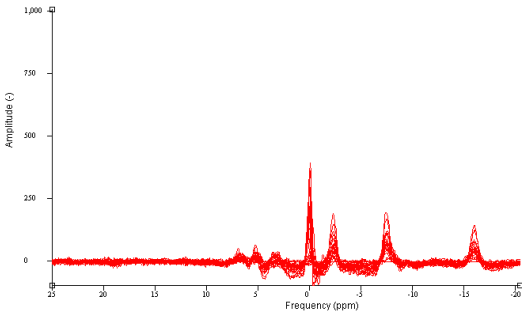

(c) Spectrum after the preprocessing

Figure 3.11. The first image shows the anatomical image with the selected voxels. Figure 3.11(b) shows the superposition of the spectra from the selected voxels before preprocessing. Figure 3.11(c) shows the superposition of the selected spectra after the preprocessing where the metabolite peaks are more distinguishable from the noise. To get these spectra, the preprocessing steps done included removal of PPA peaks, 15 Hz apodization, phase corrections, and β-ATP field inhomogeneity corrections.

original data (red) with the estimated fit overlaid (blue). The middle spectrum is the fit produced by AMARES and then the top spectrum shows the residue of the fit which is just the subtraction of the estimate from the original data. This tool provides an easy visual analysis of the estimated fit for each spectrum.

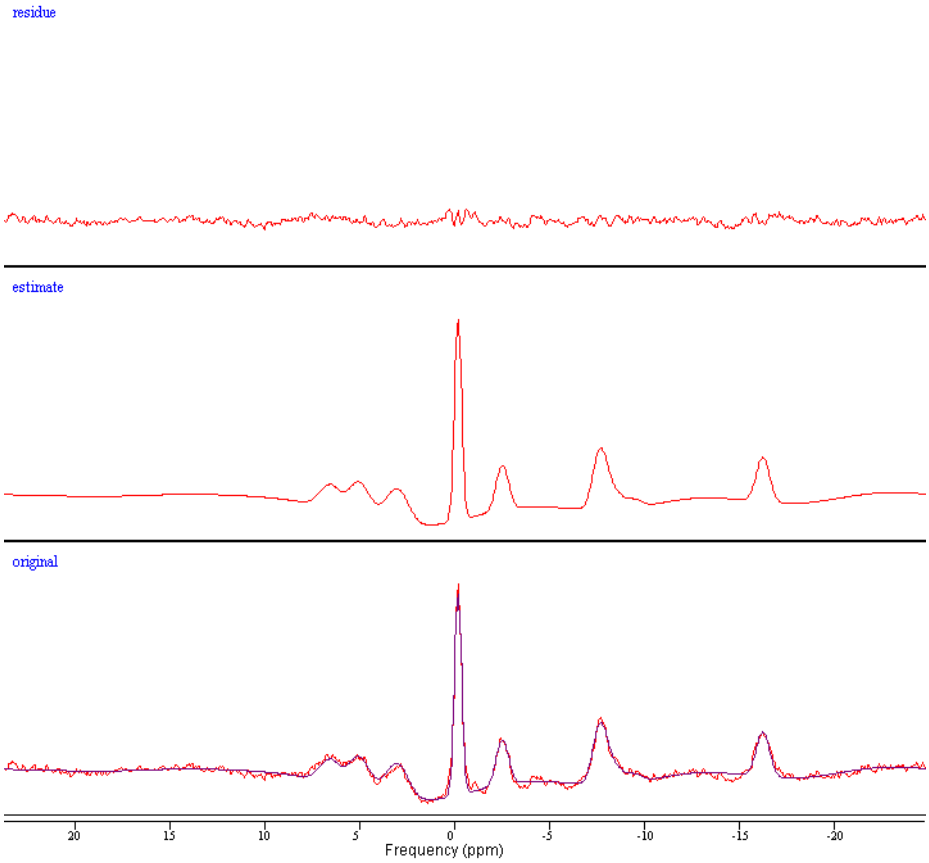

Figure 3.12. Spectra fitting results. The bottom spectrum shows the original data signal with the estimate overlaid on it. The middle spectrum is the estimate and the top image is the residue of the estimated fit subtracted from the original spectrum. The vertical axis is not shown, but consists of arbitrary units.

3.4 GRAPPA Validation

Dr. Scott Jones found in [22] that the 1st and 8th slice in a 3D acquisition suffered from poor reproducibility. For this reason, I have excluded the analysis and fitting of these slices from this work. He also found in the same study that the in-vivo reproducibility of the ^{31}P spectrum could vary as much as 60% in extreme cases while being significantly less in others, depending on the metabolite being studied. Thus,

an average of a 20% threshold was used here meaning that any change greater than 20% was considered to be statistically relevant.

One thing to note: the artifacts found outside of the volume defined by the PPA markers introduced in Section 3.1.1 will be viewed with less significance than the signal compared within the region of the PPA markers. The reason for this is that the signal outside of the markers is clearly an artifact as all of the signal will be coming from the subjects body, which only lies within the PPA markers. Thus, the artifacts will be quantified but can be confidently discarded based on spatial positioning.

The validation of this acquisition will be based upon the following: reconstruction of the signal found within the body, artifact amplitude reduction, SNR, and SNR per second. The reconstruction of the signal will be defined as the ratio of the fitted reconstructed peak to the fitted baseline peak. Similarly, the artifact reduction will be defined as the ratio of the fitted reconstructed artifact amplitude to the fitted amplitude of the peak without GRAPPA reconstruction. The SNR will be defined as the ratio of the jMRUI amplitude of the fitted peak to the noise that is generated by jMRUI, found from the last 10% of the original FID signal, which is considered to be only noise. The SNR per second will be defined as the SNR divided by the total number of seconds needed for the entire acquisition.

4. Results

The following results require the definition of a few additional terms. First, we will define foldover artifacts/peaks as peaks resulting from the undersampling of k-space, violating the Nyquist theorem, and were not found in the baseline acquisition. Reconstructed peaks will be defined as the peaks from within the volume of interest (VOI) that are reconstructed by the GRAPPA algorithm and should, in the ideal case, be equal to the peaks seen in the baseline scan.

4.1 Phantom Results

Before undertaking in-vivo experiments, phantoms were used for validation of GRAPPA undersampling and reconstruction. For this work, I have included an analysis of the Polly phantom, whose details can be found in Section 3.1.2. Note that all metabolite maps given in this section, Section 4.1, are of inorganic phosphate (Pi), as this is the only metabolite in the Polly insert. The voxels indicated in Figure 4.1, which shows four slices out of eight, will be used in the following analysis. The red voxels show the original signal from the insert and will be referred to as the baseline signal for the conventional scans and the reconstructed signals for the GRAPPA scans. The blue voxels are areas of foldover artifacts. When analyzing just the k_y GRAPPA foldover effects, the blue voxels on the right will be excluded.

4.1.1 Phantom GRAPPA Reconstruction Implementation

Figure 4.2 shows the reconstructed Pi metabolite maps of the fifth slice, out of eight, for the Polly phantom. A visual inspection gives a qualitative result that the artifacts have been greatly reduced and the signal from the insert has been ad-

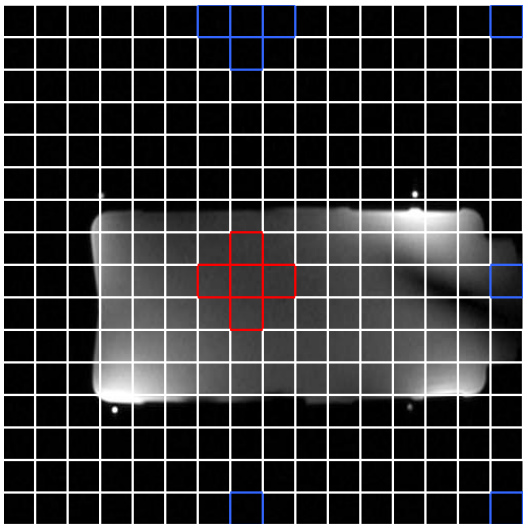

(a) Voxels of interest for the Polly phantom, slice 3

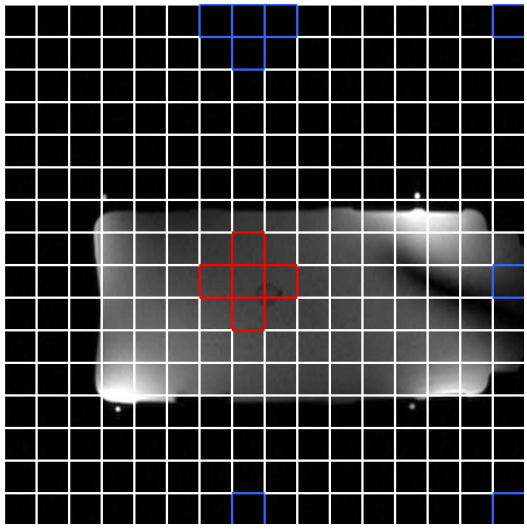

(b) Voxels of interest for the Polly phantom, slice 4

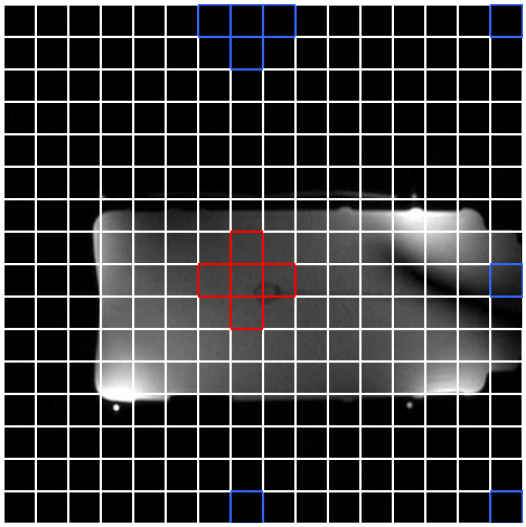

(c) Voxels of interest for the Polly phantom, slice 5

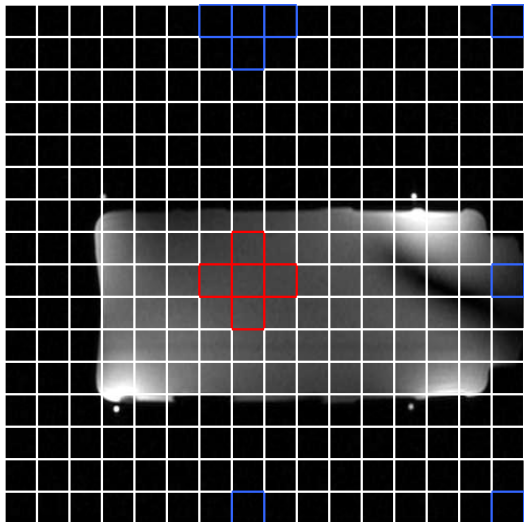

(d) Voxels of interest for the Polly phantom, slice 6

Figure 4.1. Voxels of interest for foldover artifacts for the Polly phantom for the 2D GRAPPA reconstruction. When only interested in the k_y GRAPPA reconstruction, the blue voxels on the right can be excluded. The red voxels indicate the reconstructed/main signal, while the blue voxels indicate the regions of foldover artifacts.

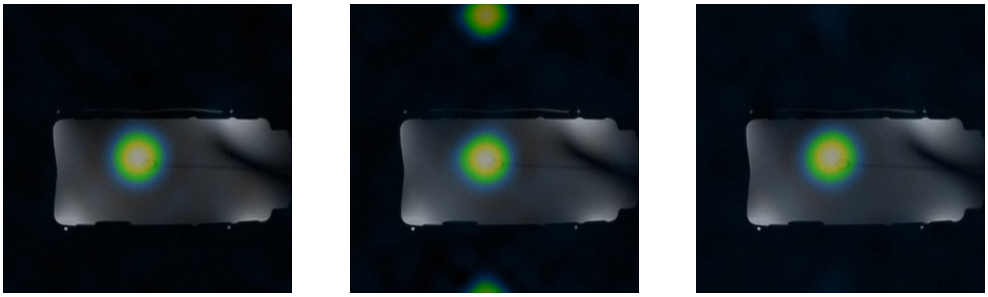

(a) Baseline (31:48)

(b) k_y undersampling without GRAPPA reconstruction (17:12)

(c) k_y undersampling with GRAPPA reconstruction (17:12)

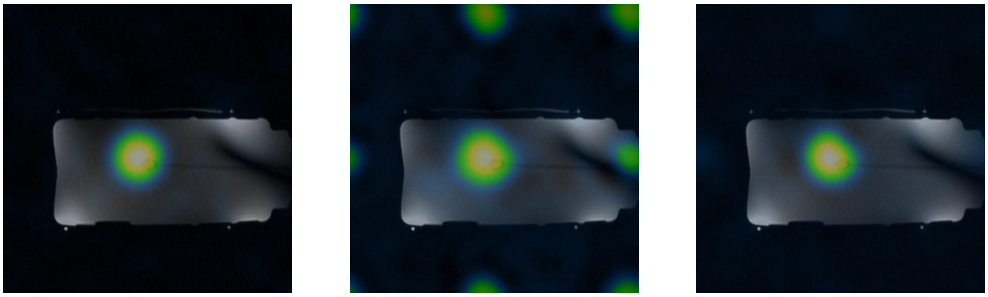

(d) Baseline (31:48)

(e) 3D undersampling without GRAPPA reconstruction (10:04)

(f) 3D undersampling with GRAPPA reconstruction (10:04)

Figure 4.2. Slice 5 of baseline ^{31}P MRS scan (left), undersampling without GRAPPA reconstruction (middle), and undersampling with GRAPPA reconstruction (right) with the time comparisons for each as (mm:ss). See Table A for results for all eight slices

equately reconstructed. Figure 4.3 shows the ratio of the amplitudes of the fitted reconstructed peaks with the fitted baseline peaks. In all slices that contain signal from the Pi insert, the ratio of the amplitudes is within 10% or less of the baseline peak amplitude. However, due to the setup in this phantom, undersampling only causes foldover artifacts outside of the object. Thus, this value is to be interpreted as a general reproducibility of the signal from the insert.

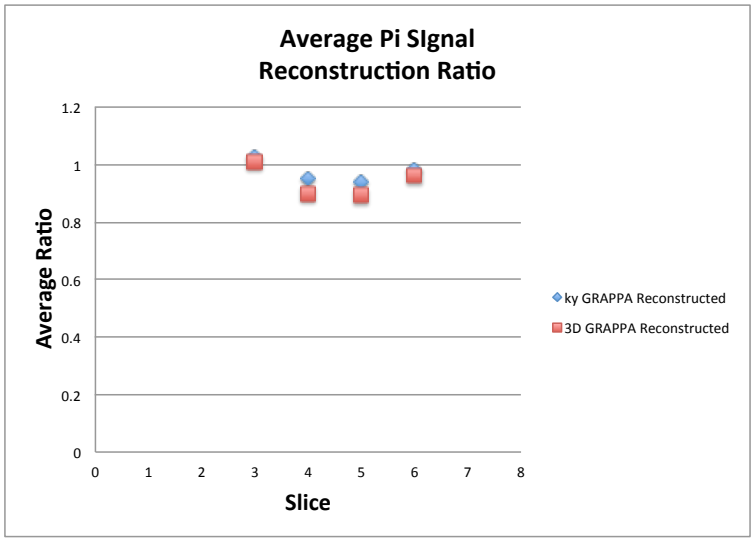

Figure 4.3. Pi signal reconstruction comparison using k_y and 2D GRAPPA reconstruction by taking the ratio of the average GRAPPA reconstructed signal to the weighted acquisition signal. The amplitude of the reconstructed peaks were divided by the amplitude of the baseline peaks, averaging the voxels indicated in red in Figure 4.1.

4.1.2 SNR and Effective Voxel Size

The SNR per second of this acquisition is seen in Figure 4.4(b) where it is shown that the SNR/s of the 2D GRAPPA reconstruction on this volume is over 2 times greater than that of the SNR/s of the baseline scan. The reason for this is evident when we look at the SNR of the scans, noting that similar SNR is achieved for all types of acquisitions. The decreased acquisition time for the k_y and 2D reconstruction schemes give the greater SNR/s desired.

The effective voxel size is indicative of the effective resolution of a protocol, which usually differs from the nominal size. The nominal voxel size was defined to be 2.5 x 2.5 x 2.5 cm^3 = 15.63 cm^3. Zero-filling the FID signal from the Polly phantom achieved a 32x32 element MRS grid. Since the Polly phantom contained a small insert with the Pi metabolite, it can be thought of effectively as a delta source of signal. Thus, taking a signal profile in any direction will show the blurring associated with the acquistion and reconstruction scheme and allows for the calculation of the

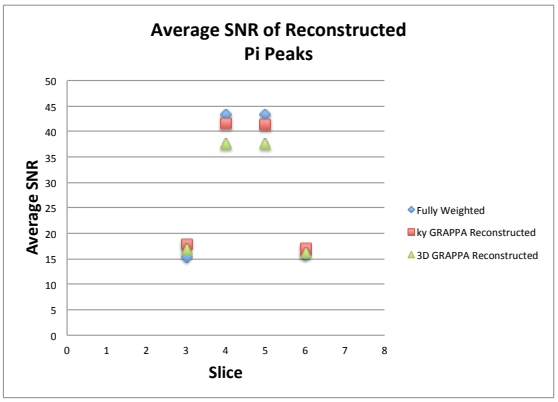

(a) Average SNR using GRAPPA reconstructions

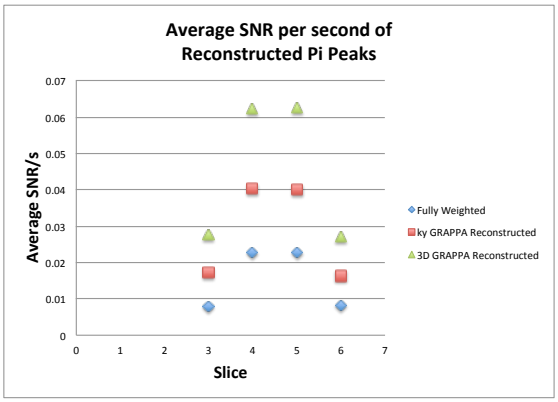

(b) Average SNR per second using GRAPPA reconstructions

Figure 4.4. SNR and SNR per second for the two different reconstruction methods. Note that both the k_y and 3D GRAPPA reconstruction methods give similar SNR for the relevant slices. Slices 3 and 4 only contain signal at all due to the blurring (PSF) of the weighted acquisition scheme. The SNR per second of the 3D GRAPPA reconstruction is over 2 times greater than that of the fully sampled scan.

effective voxel size for this acquisition. A signal profile was created by projecting the total signal along each axis to show the effective voxel size. Pohmann has shown that the effective voxel size could be found by the full width at 64% the maximum value of the spectral peak [44]. Figure 4.5 shows the projected signals from the fourth slice of the Polly phantom and their effective voxel dimensions. Combining the dimensions found in Figure 4.5, the effective voxel volume for the conventional acquisition is 4.27 x 4.27 x 5.64 = 102.9 cm^3, which is 6.5 times larger than the nominal voxel size, and the effective voxel volume of the GRAPPA reconstructed acquisition is 4.34 x 4.19 x 5.84 = 106.1 cm^3, an increase in size of 3.2% from the conventional acquisition and 7 times larger than the nominal voxel size.

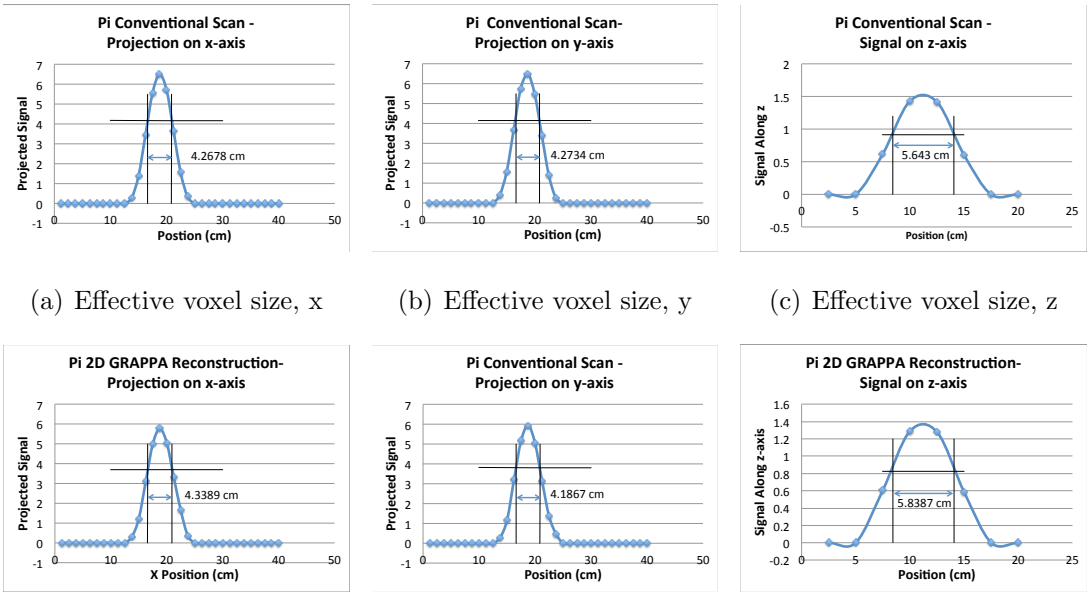

(a) Effective voxel size, x (b) Effective voxel size, y (c) Effective voxel size, z

(d) Effective voxel size, x (e) Effective voxel size, y (f) Effective voxel size, z

Figure 4.5. PSF analysis of the Polly phantom. Shown here is the projected signal along the x-, y-, and z-axis for the fourth slice from the Polly phantom. The top row is from the conventional weighted acquisition while the bottom row shows the voxel size for the 2D GRAPPA reconstruction.

4.1.3 Artifacts

When the Polly phantom has been undersampled in one direction without GRAPPA reconstruction, the foldover artifacts are clearly visible, as seen in Figure 4.2. Figure 4.2(e) shows the foldover artifacts for undersampling in both the k_x and k_y directions. Since the Polly phantom has a single spherical insert centered at the isocenter of the scanner, the only signal should come from the middle of these slices.

A successful reduction of scan time would also entail that the resulting spectra would not have any significant foldover artifacts. Quantifying the data using the methods described in Section 3.3, we can obtain amplitudes of the foldover peaks for both the reconstructed and undersampled scans in the voxels indicated in Figure 4.1. By taking the ratio of the amplitudes of the reconstructed peak to the foldover peak, we can obtain a percentage of the reduction of the foldover artifacts. Looking at

Figure 4.6, we see that the highest peak amplitude after the GRAPPA reconstruction is approximately 20% of the amplitude before reconstruction, with most points being under that mark.

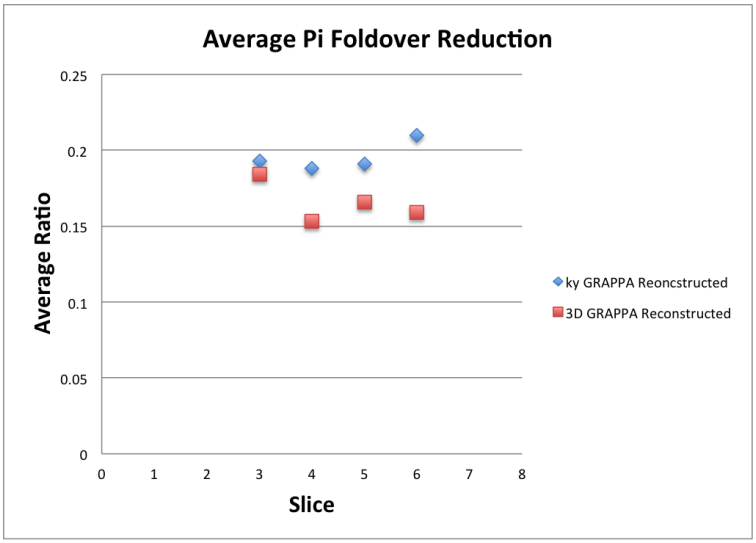

Figure 4.6. Pi signal ratio of the GRAPPA reconstructed foldover peak to the nonreconstructed foldover peak.

4.2 in-vivo Results

Two healthy volunteers were scanned to test the in-vivo capabilities of the 3D GRAPPA acquisition. For this analysis, all ^{31}P peaks mentioned in Table 1.2 will be quantified. To analyze the performance of the GRAPPA reconstruction with respect to foldover artifacts, focus will only be on the PCr peak. The reasoning for this is that the PCr peak is localized to the muscles, meaning it won't be found outside of a muscular region except due to voxel "bleeding". A similar analysis to that performed on the Polly phantom will be done here.

The first healthy volunteer is codenamed HVOL1 and was an adult male (age of 26). Three scans were performed for HVOL1: baseline, k_y undersampling without GRAPPA reconstruction, and k_y undersampling with GRAPPA reconstruction.

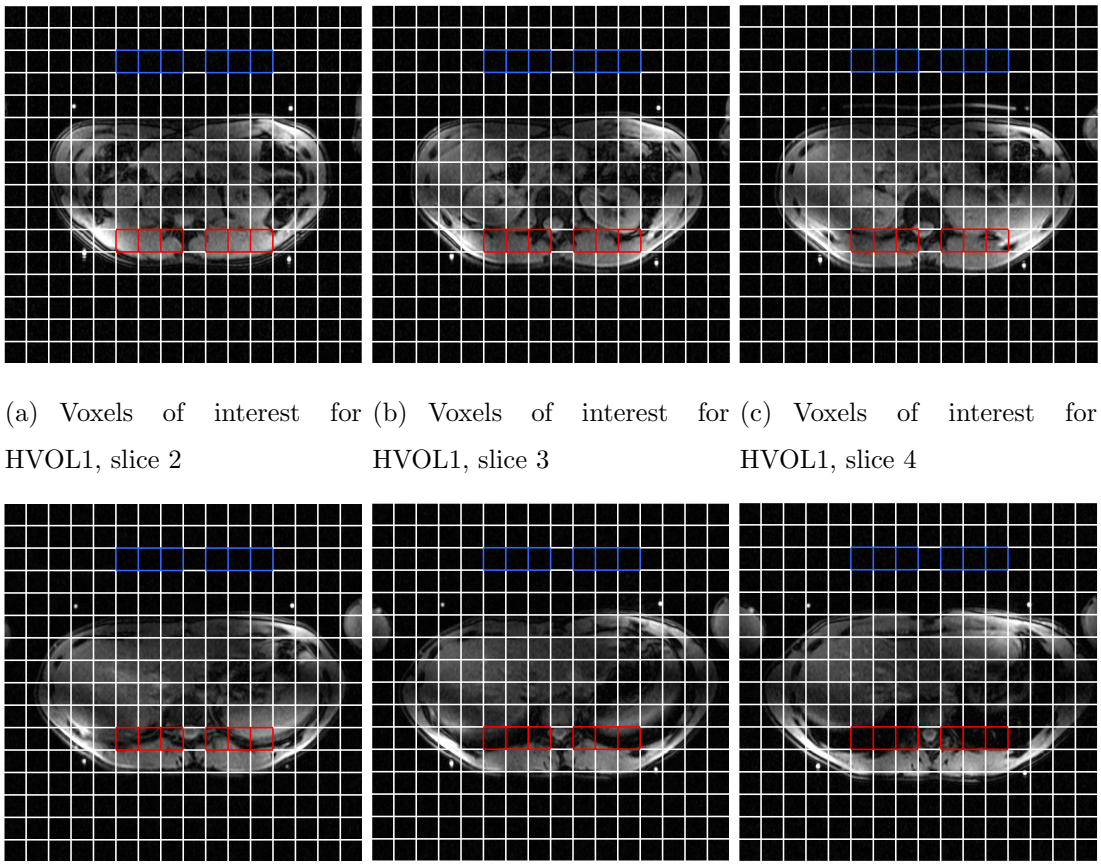

(a) Voxels of interest for HVOL1, slice 2

(b) Voxels of interest for HVOL1, slice 3

(c) Voxels of interest for HVOL1, slice 4

(d) Voxels of interest for HVOL1, slice 5

(e) Voxels of interest for HVOL1, slice 6

(f) Voxels of interest for HVOL1, slice 7

Figure 4.7. Voxels of interest for foldover artifacts for HVOL1 using k_y GRAPPA reconstruction on a 3D acquisition. The red voxels indicate the main/reconstructed PCr signal, while the blue voxels indicate the regions of foldover artifacts. When only interested in the conventional reconstruction, the blue voxels can be excluded.

The second healthy volunteer was codenamed HVOL2 and was an adult male (age of 27). Five scans were performed for HVOL2: a baseline scan with conventional weighted acquisitions, k_y undersampling with and without GRAPPA reconstruction, 2D undersampling on a 3D volume with and without GRAPPA reconstruction.

For the following analysis, slices 1 and 8 will not be taken into account. Jones found that the two edge slices (1 and 8) had the highest variation and was the least

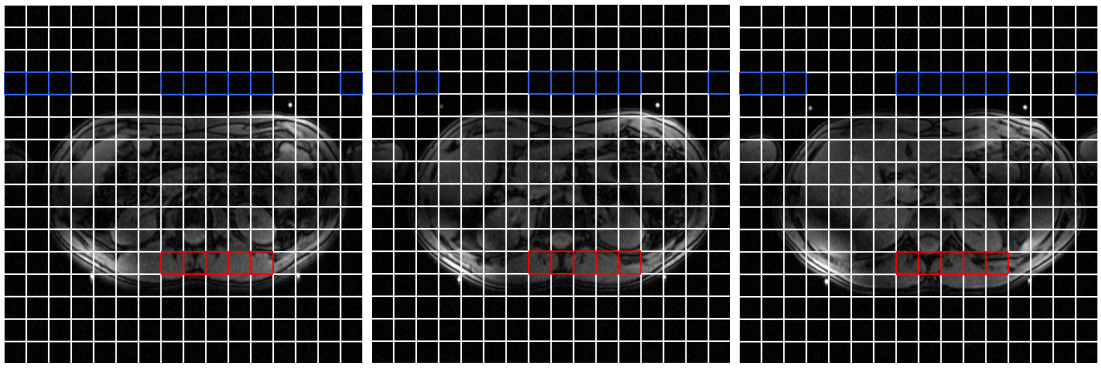

(a) Voxels of interest for HVOL2, slice 2

(b) Voxels of interest for HVOL2, slice 3

(c) Voxels of interest for HVOL2, slice 4

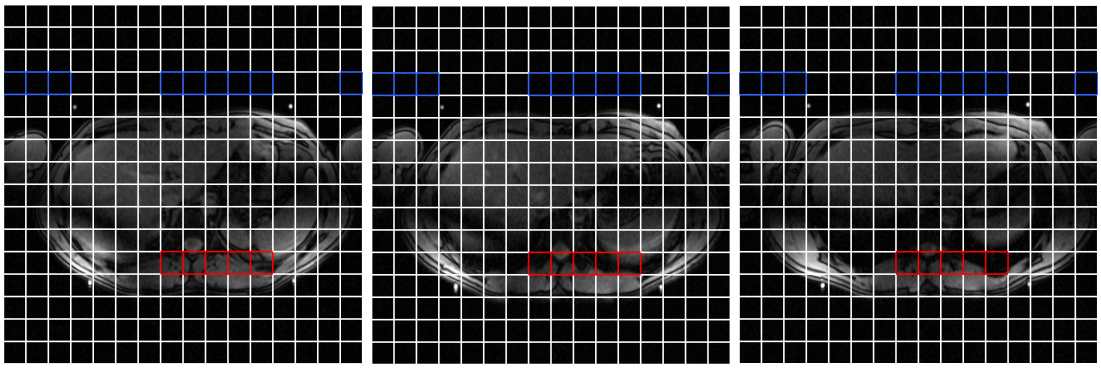

(d) Voxels of interest for HVOL2, slice 5

(e) Voxels of interest for HVOL2, slice 6

(f) Voxels of interest for HVOL2, slice 7

Figure 4.8. Voxels of interest for foldover artifacts for HVOL2 using k_y and 2D GRAPPA reconstruction on a 3D acquisition. The red voxels indicate the main/reconstructed PCr signal, while the blue voxels indicate the regions of foldover artifacts. When only interested in the conventional reconstruction, the blue voxels can be excluded. When only interested in the k_y GRAPPA reconstruction the edge voxels can be excluded.

reproducible using the same coil and baseline 3D acquisition protocol [22]. For this reason, slices 1 and 8 will be excluded from this analysis.

Figure 4.7 shows the different voxels of interest that will be used in the following analysis of HVOL1 for slices 2 through 7. The red voxels indicate the original PCr signal origin and the blue voxels show the voxels that will contain foldover artifacts.

Figure 4.8 shows all of the voxels of interest used for HVOL2. The voxels shown include both the k_y and 2D GRAPPA reconstruction voxels that will be used in the following analysis. The coloring scheme follows the same rules as those in Figure 4.7. When only viewing the k_y GRAPPA reconstruction data, exclude the voxels on the edges.

4.2.1 in-vivo GRAPPA Reconstruction Implementation

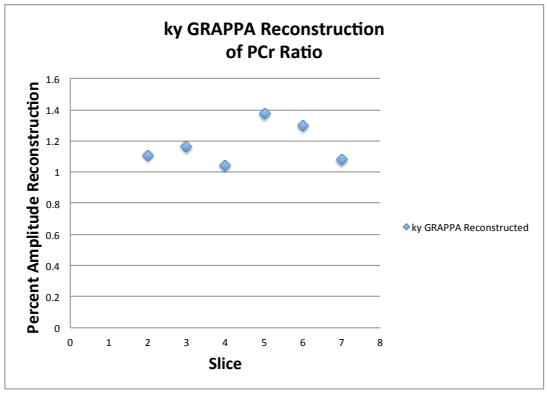

(a) Percent reconstruction of PCr amplitude for HVOL1

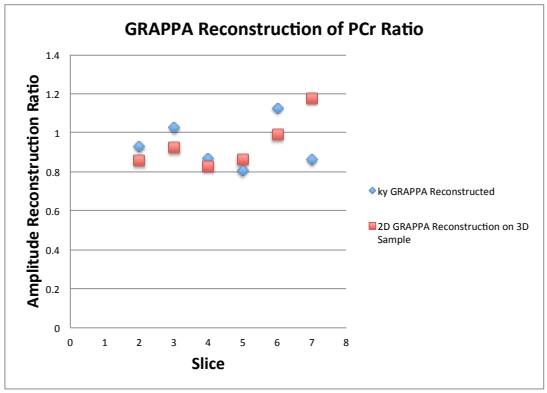

(b) Percent reconstruction of PCr amplitude for HVOL2

Figure 4.9. Reconstruction amplitude ratio for HVOL1 and HVOL2 using k_y GRAPPA reconstructions and 2D GRAPPA reconstruction.

Figure 4.9 shows that the reconstructed amplitude of the PCr peaks fall within a range of about 20% around the true value of the fully weighted data. This is in close agreement with what we have found previously with the Polly phantom. Similarly to that phantom, there will be no foldover artifacts will occur in this setup within the anatomical volume due to the red voxels, so this 20% is a measure of the reproducibility and SNR of the the reconstructed voxels.

One method of verification is to show a faithful reconstruction of certain metabolite maps in the liver. Figure 4.10 shows both the β-ATP metabolite maps obtained

from conventional scans and the 2D GRAPPA reconstruction scans. β-ATP is, theoretically, spread evenly throughout the whole liver. Figure 4.10 shows that this is the case, with the liver clearly outlined with the β-ATP maps in slices 5 and 6. These maps were created by quantifying the ^{31}P MRS spectra and interpolating the fitted amplitudes using a bilinear interpolation up to a 512x512 image.

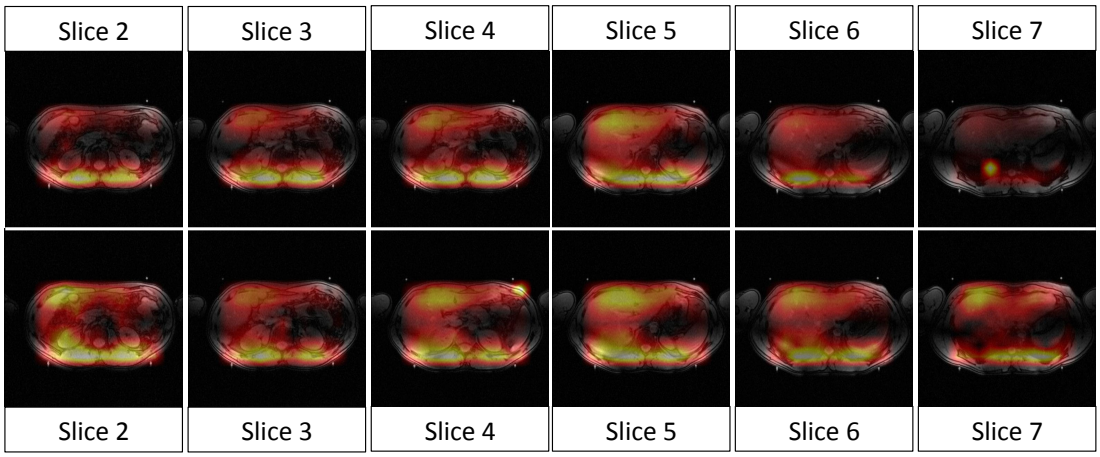

Figure 4.10. HVOL2 β-ATP metabolite maps of slices 2 through 7 using conventional and 2D GRAPPA reconstruction acquisitions. The top row shows the metabolite maps of the conventional acquisition and the bottom row shows the GRAPPA reconstructed metabolite maps.

Figure 4.10 indicates that this reconstruction method is not confined to Pi and PCr, the two major metabolites focused on in this work. Figure 4.11 shows the conventional and 2D GRAPPA reconstructed spectrum for a voxel located deep within the liver. It shows that the liver spectrum is reproducible with the ^{31}P GRAPPA acquisition, even deep within the liver. Note that the PCr resonance peak is missing from these spectra due to the fact that this voxel is not located near muscular regions. Therefore, the GRAPPA reconstruction presented here is feasible across the entire ^{31}P liver spectrum.

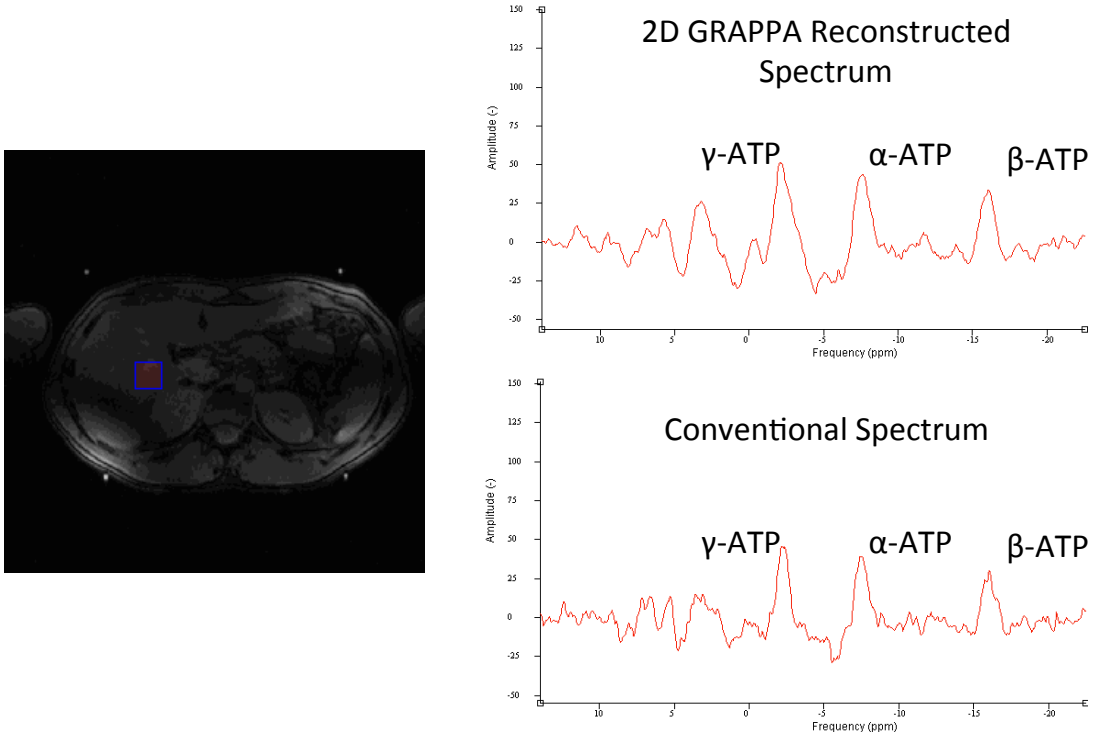

Figure 4.11. Conventional and 2D GRAPPA reconstructed spectra for the indicated voxel. These spectra came from the fourth slice of HVOL2

4.2.2 in-vivo SNR Results

Figure 4.12 shows both the SNR and the SNR per second plots, averaged over the red voxels, of slices 2 through 7 for both HVOL1 and HVOL2. Note that, as with the Polly phantom, the SNR per second shown in Figure 4.13(a) is almost double the SNR per second of the fully weighted acquisition in certain slices. This, again, agrees with what was found using the developmental phantoms.

What truly stands out is shown in Figure 4.13(b). Here we see that the fully weighted acquisition has a lower SNR per second than the other two acquisition schemes while the k_y reconstructed acquisition produced the expected SNR per second between the fully weighted and the 3D GRAPPA scheme. The 3D GRAPPA acquisition can be as much as three times greater than the fully weighted SNR per second!

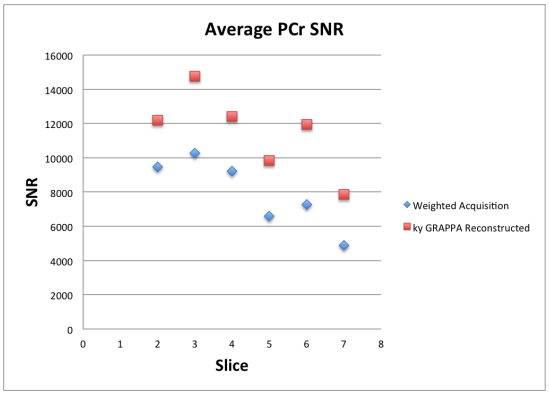

(a) Average PCr SNR using k_y GRAPPA reconstruction for HVOL1

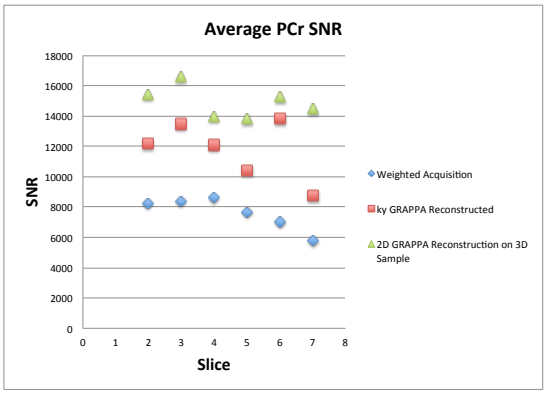

(b) Average PCr SNR using GRAPPA reconstructions for HVOL2

Figure 4.12. Average SNR and SNR per second of select voxels for both HVOL1 and HVOL2 using k_y GRAPPA recosntruction

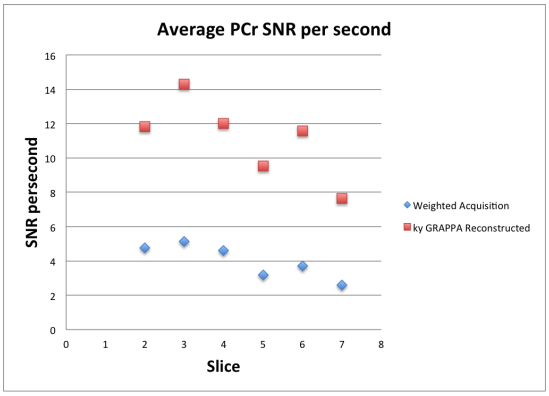

(a) Average SNR per second using k_y GRAPPA reconstruction for HVOL1

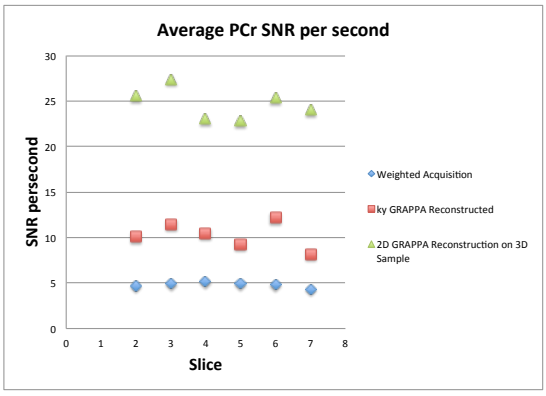

(b) Average SNR per second using GRAPPA reconstruction for HVOL2

Figure 4.13. Average PCr SNR per second for both HVOL1 and HVOL2. We see here that with each new implementation of a GRAPPA direction, we gain SNR/s.

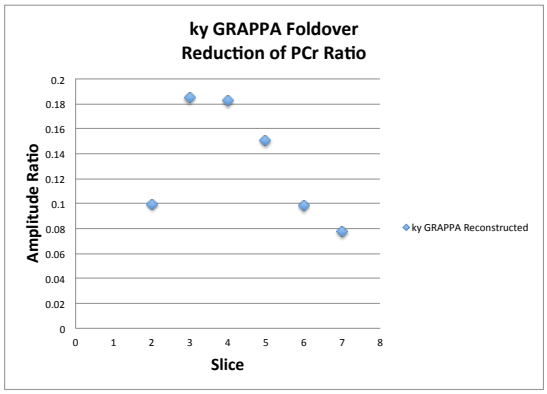

(a) Foldover artifact reduction ratios for HVOL1 using k_y GRAPPA reconstruction

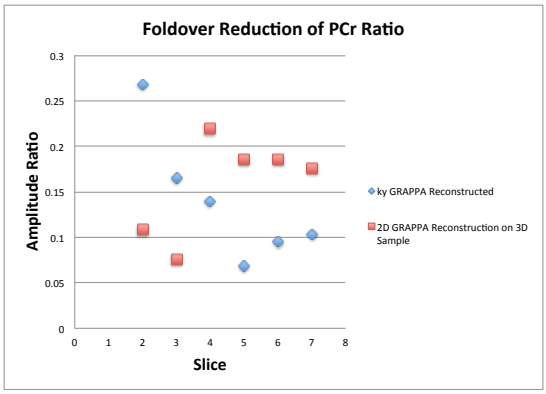

(b) Foldover artifact reduction ratios for HVOL2 using GRAPPA reconstruction

Figure 4.14. Average foldover artifact reduction ratios of PCr signals using GRAPPA reconstructions for HVOL1 (Figure 4.14(a)) and HVOL2 (Figure 4.14(b))

4.2.3 in-vivo Artifacts

Figure 4.15 presents PCr metabolite maps for HVOL1 and HVOL2. The images presented here are from the fifth slice out of eight for both volunteers and first show the k_y foldover artifacts present without the k_y GRAPPA reconstruction. The last column in Figure 4.15 show the different GRAPPA reconstructions and the reduction of the foldover artifacts. The 2D GRAPPA reconstruction of HVOL2 is "greener" than the other images. This is caused for two reasons: higher background signal and lower reconstructed PCr signal.

The artifacts are reduced to the point of minimal, if any, visibility in these overlays. This is seen quantitatively in Figure 4.14 which shows the amplitudes of the foldover artifacts being reduced by 80% or more for HVOL1 and reduced by 70% or better for HVOL2. Figure 4.16 shows the 2D undersampling and reconstruction effects on different spectra from HVOL2.

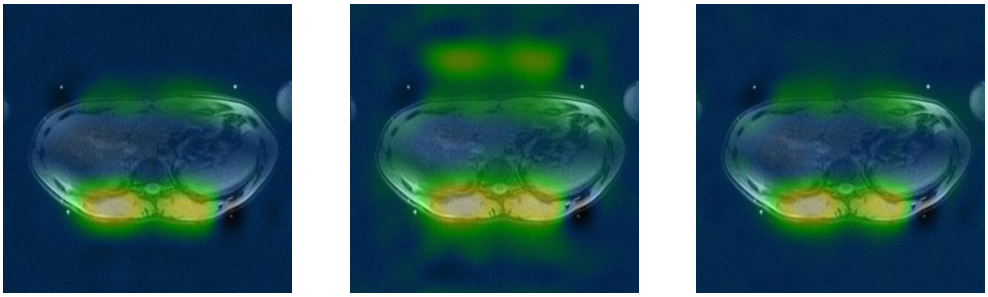

(a) Baseline scan of conventional acquisition of HVOL1 (31:48)

(b) k_y undersampling without GRAPPA reconstruction of HVOL1 (17:12)

(c) k_y undersampling with GRAPPA reconstruction of HVOL1 (17:12)

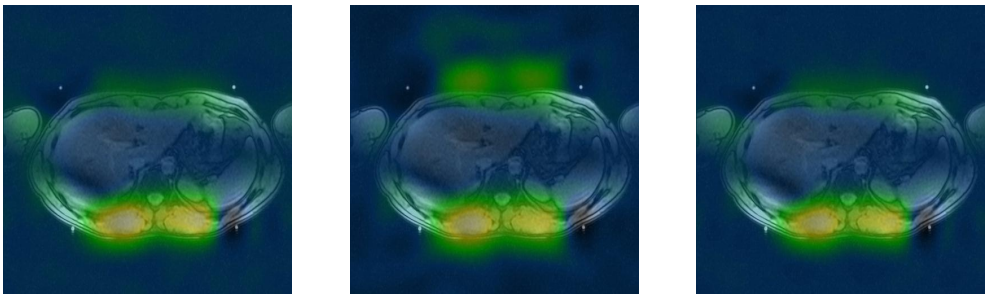

(d) Baseline scan of conventional acquisition of HVOL2 (31:48)

(e) k_y undersampling without GRAPPA reconstruction of HVOL2 (17:12)

(f) k_y undersampling with GRAPPA reconstruction of HVOL2 (17:12)

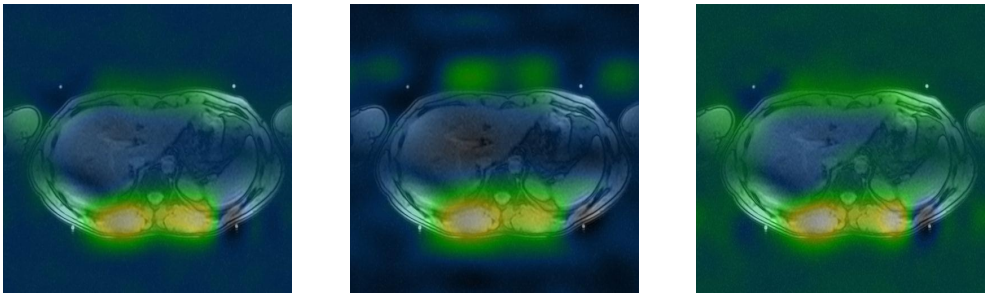

(g) Baseline (31:48)

(h) 2D undersampling without GRAPPA reconstruction (10:04)

(i) 2D undersampling with GRAPPA reconstruction (10:04)

Figure 4.15. Large versions of metabolite overlay maps for baseline, k_y undersampling, and k_y reconstruction. Refer to Table A.5, Table A.7, and Table A.8 in the appendix for the complete set of eight slices from each volunteer.

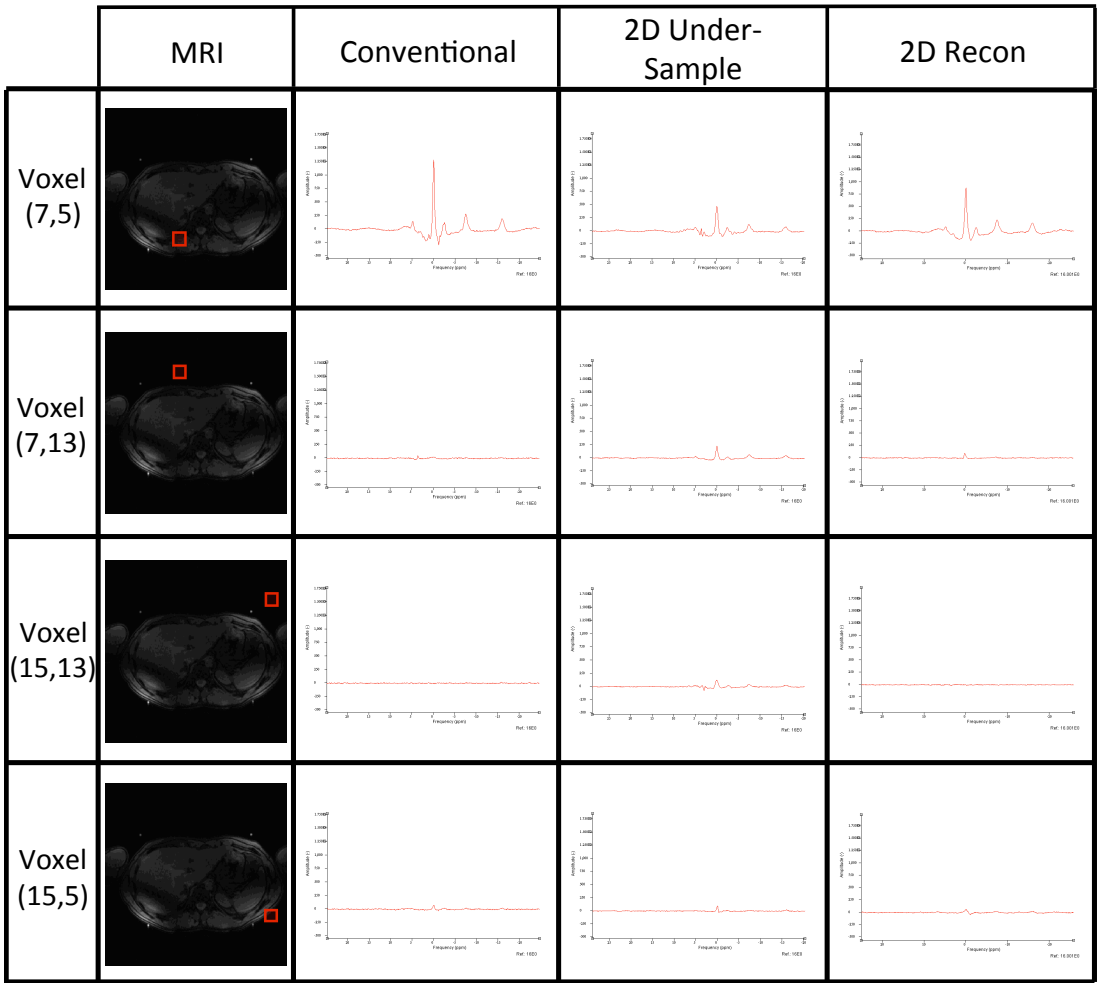

Figure 4.16. The effects of 2D undersampling and reconstruction on the in-vivo spectra are shown for the indicated voxels. These voxels contain the original spectra as well as the foldover signals.

5. Discussion and Conclusion

5.1 Discussion

Dr. Anshuman Panda found that undersampling a single slice of ^{31}P MRS k-space matrix as seen in Figure 2.6 leads to significant decrease in acquisition time and an increase in SNR per unit time for a single slice, 2D scan of a human liver [21]. Using a similar method, I was able to achieve a greater decrease in the scan time and increase the SNR per unit time for a three dimensional, volume acquisition. An acquisition scheme as seen in Figure 3.9 was used. This method used one set of weights to reconstruct *all* the slices in the k-space matrix in the k_y direction and then repeats for the k_x with a different set of weights. This significantly reduces the number of averages taken during the acquisition which in turn reduces the time needed to acquire the necessary data, since the filling of the k-space matrix can be done post-scan. It can be seen from (2.16) that the weights only depend on the k-space offset in the direction of interest. This means that we can reduce the reconstruction of the k-space matrix into individual reconstructions along the x, y, and z directions of the matrix.

This acquisition improves upon the original method seen in the thesis of Dr. Panda [21] in the following ways:

1. Increased SNR due to a larger excitation volume (3D acquisition versus a 2D acquisition) [22]

2. Decreased total scan time from 11 minutes and 48 seconds to 10 minutes and 4 seconds while sampling eight slices instead of one

3. Increased SNR per unit time due to the combination of the previous two items

With the completion of this work, a major step towards introducing ^{31}P MRS into a clinical environment has been achieved. This work has shown that with 3D GRAPPA, the scan time of a ^{31}P MRS data acquisition can be reduced to just 10 minutes. This is a major breakthrough as the previous ^{31}P MRS scan times had heretofore been 30 minutes or more.

The first aim of this work was to implement and validate a 2D GRAPPA reconstruction on a 3D volume. This was shown in Section 4.1. There it was shown that both types of GRAPPA reconstruction used in this work were able to reproduce the Pi insert signal within 10% or better. The SNR/s was found to increase for each dimensional implementation used, increasing as much as 2-3 times compared to the conventional scan. A larger SNR per second is that a similar signal can be achieved via reconstruction in a smaller amount of time, leading to a much faster and more comfortable scan for patients.

The tradeoff for an increase in SNR and SNR/s is a loss in voxel spatial resolution due to a broadening of the PSF. It has been shown that the nominal voxel size is not the true, effective voxel size. By looking at the PSF in all three dimensions, it was shown that the effective voxel size of a conventional weighted scan was 4.27 x 4.27 x 5.64 cm^3 while the GRAPPA reconstructed voxel size was 4.34 x 4.19 x 5.84 cm^3, an increase in voxel volume of 3%. This is in close agreement with what Panda found in his work, that the voxel volume had increased by 6.6% for a 2D reconstruction on single slice acquisition [21].

Finally, it was shown that the foldover reductions were reduced after GRAPPA reconstruction, but in some cases there remained a residual signal. Though the artifacts are greatly reduced, in our phantom trials, we can neglect them as the FOV was so much larger than the actual phantom that all foldover artifacts lie outside the phantom. Any signal found outside of the volume defined by the PPA fiducial markers must come from artifacts as the only origin of signal lies within the PPA defined volume. In cases in which the foldover artifacts fold over the object itself, i.e. when a patient is large enough that the artifacts lay over actual anatomy, we may

need to consider other options. One such option would be further optimization of the current sequence. Similar foldover artifacts found in this work were also shown to not be completely removed in Figures 3.10 and 3.11 of Panda's work [21].

Improper fitting of the ACS lines, seems to be the most likely suspect as to the residual foldover artifact signal. The explanation for this is that the signal towards the middle of the anatomy decreases [20] leading to signals that become more challenging to find a correct fit for the ACS. If there had been incorrect fitting of ACS lines, this would result in incorrect reconstruction of all of the reconstructed lines of k-space and artifacts would thus be seen throughout the entire FOV. These artifacts would be seen as additional noise or blurring of the ^{31}P MRS signal. This is can be seen in the figures of the different reconstructions in Appendix A.

The second aim was to validate the new ^{31}P GRAPPA technique on healthy volunteers. Data from two volunteers was obtained and PCr metabolite maps were created to show the feasibility of the GRAPPA reconstruction. For HVOL2, it was shown that the ^{31}P GRAPPA acquisition was still able to faithfully reproduce β-ATP metabolite maps throughout the whole liver at a scan time that was one third the time needed to create the β-ATP metabolite map with the conventional acquisition.

An SNR analysis of the PCr signal shows that for both volunteers, the SNR decreased from slice two through slice seven. This is easily explained when we look at the anatomy contained within these slices. The PCr peak is an indicator of the amount of muscle within the voxel. As we move through the slices from two to eight, we are moving *up* the torso from the intestines to the heart. The farther up we move, the less abdominal and lower back muscles there are. The volume of interest does not go high enough on the torso to get back to the upper back muscles and the pectoral muscles on the chest. Thus, the PCr SNR decreases due to the anatomy, not due to the acquisition as seen in Figure 4.12 and Figure 4.13.

Again, it was shown that the SNR/s value for 2D GRAPPA reconstruction on a 3D volume was the highest out of the three reconstruction methods tested (conventional, k_y GRAPPA, 2D GRAPPA). This value was shown to be roughly five times greater

for the 2D GRAPPA reconstruction than the conventional scan. The artifacts for the in-vivo volunteers were reduced in amplitude by approximately 80% or more, agreeing with what was found with the developmental phantoms.

5.2 Future Work

The next logical step with the validation of the ^{31}P GRAPPA reconstruction would be to first acquire more healthy volunteers. These volunteers should at first be similar to the volunteers used already to test for reproducibility of the GRAPPA sequence. Following this, another set of volunteers should be tested, ranging in size, sex, age, etc. to test the limits of this new ^{31}P 3D GRAPPA acquisition. Finally, a trial using liver cancer patients should be tested for the feasibility of the use for that population.

The motivation of this work was to decrease the scan time of ^{31}P MRS to increase patient comfort and potentially decrease motion or respiration artifacts due to the lower scanning time. By doing this, the feasibility of using ^{31}P MRS for clinical applications would improve. Though, this is a great breakthrough, there is still much more that could be done. I believe the next step towards making ^{31}P MRS a viable clinical application would be to incorporate respiratory gating into the scans. Doing this would potentially reduce any artifacts or degradation of ^{31}P signal due to respiration. Respiratory gating could be used in tandem with the 3D GRAPPA technique to achieve a scan time similar to that of the conventional protocol, i.e., about 30 minutes. Since the respiratory gating technique would more than likely double or triple the acquisition time, the GRAPPA acquisition would negate this increase in time. This would also increase the patients comfort in the scanner by allowing data to be acquired in the supine position as opposed to the prone position that is currently in use.

Future work for this project should also include a comparison to other fast, parallel acquisition methods such as PILS, CAIPIRINHA, and compressed sensing [45–47] along with optimization of the sampling scheme used. These other fast acquisitions

have proven useful for different imaging instances and it would be of great interest to compare with the GRAPPA reconstruction presented here. In particular, CAIPIRINHA has been shown to help differentiate between adjacent slices in a multislice acquisition [46], while compressed sensing seems to be the latest breakthrough in MR imaging, allowing for fast acquisitions [48]. The optimization of the sampling scheme could include adding additional weighting factors to the k-space matrix in order to increase the acquired strength of the MR signal obtained as well as modifications to the current sequence to completely reduce the foldover artifacts obtained in this work.

One thing that I would suggest to potentially add to a new coil design would be additional channels along the z axis. A major drawback encountered in this work was being unable to do a third GRAPPA reconstruction direction due to the ambiguously acquired signal along the z direction. The current coil only has spatially different coil sensitivities along the x and y directions and thus the overlapped coil sensitivities will only allow for reconstruction along the k_x and k_y directions. By adding additional coils along the z axis, this would potentially improve the ability to more accurately reconstruct the data using a true three dimensional GRAPPA. Tests would have to be done to test if this is a viable option, as the increase in channels within the coil could mean smaller areas of the individual elements. This, in turn, could reduce the depth to which the channels can reliably see.

5.3 Conclusion

In conclusion, this work has shown that the ^{31}P MRS acquisition time can be reduced from 30 minutes to 10 minutes using a new GRAPPA reconstruction technique. This technique was validated using developmental phantoms and healthy volunteers. It was shown to reliably reproduce signal from the volume of interest to within approximately 10%. The SNR per second was shown to increase with each direction of GRAPPA reconstruction used, achieving about 2 times better SNR per second for the k_y GRAPPA reconstruction and for a 2D GRAPPA reconstruction applied to a

3D volume of interest. With these results, using a 2D GRAPPA reconstruction on a 3D volume has been shown to be a viable option to accelerate the acquisition of ^{31}P MRS data, leading to potential benefits in furthering ^{31}P MRS as a clinical tool.

APPENDICES

A. Large Figures from Results

Table A.1

The top row of images contains eight MRI "anatomical" images of the Polly phantom that correspond to the middle of the eight MRS slices; the middle row contains the metabolite maps of Pi; the bottom row contains an interpolated, overlaid image of the first two rows.

Polly Baseline Scans								
	Slice 1	Slice 2	Slice 3	Slice 4	Slice 5	Slice 6	Slice 7	Slice 8
MRI	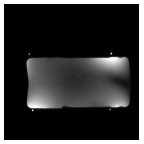	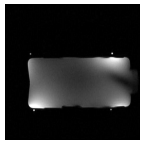	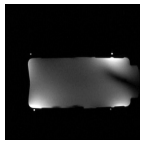	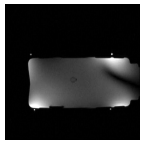	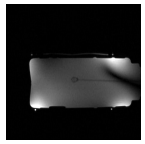	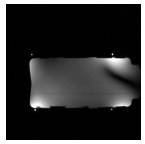	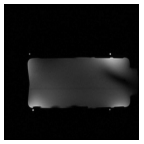	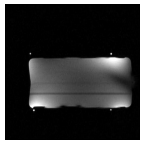
Metabolite Map	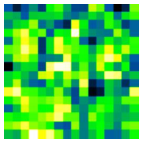	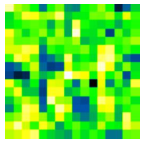	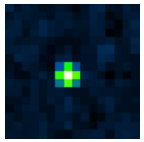	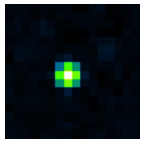	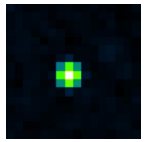	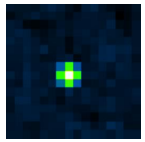	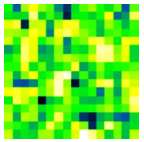	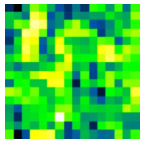
Interpolated Overlay			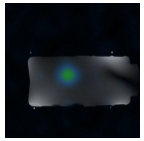	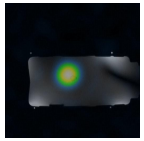	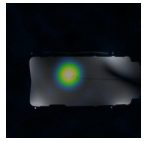	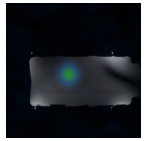		

Table A.2

The top row of images contains the eight slices of the fully weighted metabolite map overlay; the middle row contains the k_y undersampled metabolite maps; the bottom row contains an overlaid image of the k_y reconstructed data

Polly k_y GRAPPA Reconstruction Scans								
	Slice 1	Slice 2	Slice 3	Slice 4	Slice 5	Slice 6	Slice 7	Slice 8
Baseline			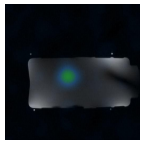	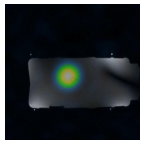	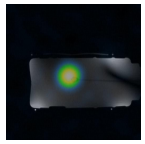	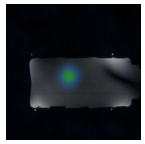		
k_y Undersample			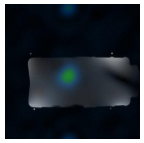	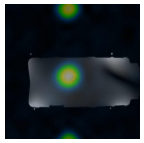	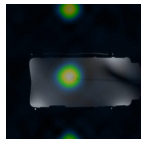	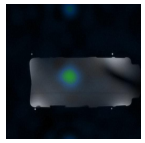		
k_y Reconstruction			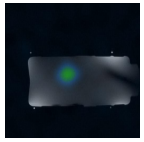	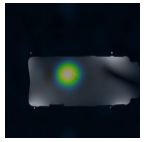	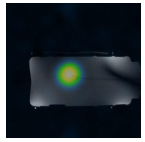	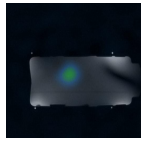		

Table A.3

The top row of images contains the eight slices of the fully weighted metabolite map overlay; the middle row contains the 2D undersampled (in three dimensions) metabolite maps; the bottom row contains an overlaid image of the 2D reconstructed (in three dimensions) data

Polly Phantom, 2D GRAPPA Reconstruction on a 3D Volume								
	Slice 1	Slice 2	Slice 3	Slice 4	Slice 5	Slice 6	Slice 7	Slice 8
Baseline			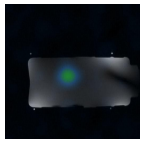	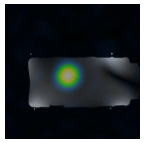	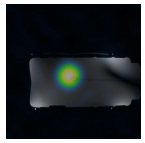	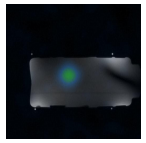		
2D Under-sample on 3D Volume		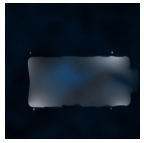	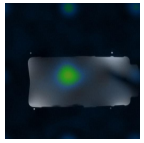	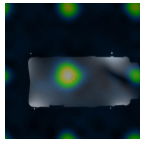	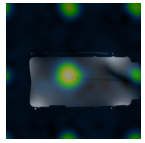	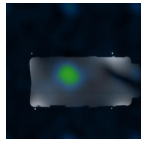	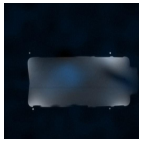	
2D Recon-struction on 3D Volume			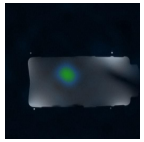	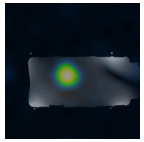	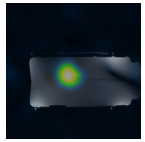	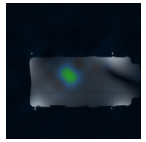		

Table A.4

The top row of images contains eight MRI anatomical images of HVOL1 that correspond to the middle of the eight MRS slices; the middle row contains the metabolite maps of PCr; the bottom row contains an overlaid image of the first two rows.

HVOL1 Baseline Scans								
	Slice 1	Slice 2	Slice 3	Slice 4	Slice 5	Slice 6	Slice 7	Slice 8
MRI	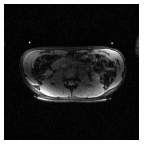	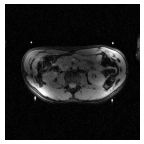	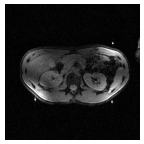	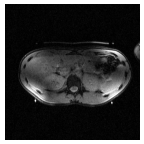	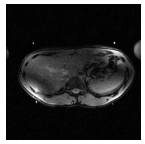	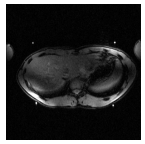	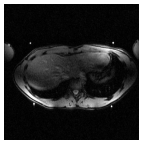	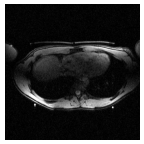
Metabolite Map	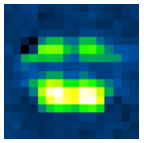	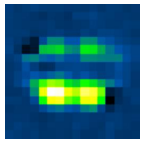	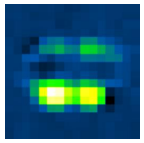	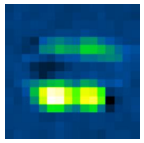	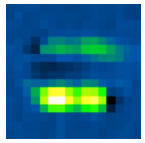	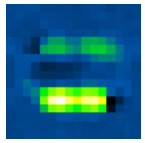		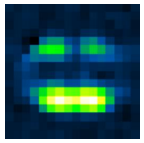
Interpolated Overlay	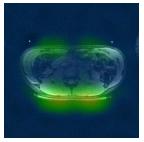	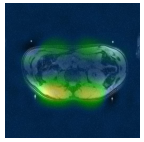	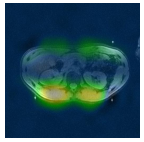	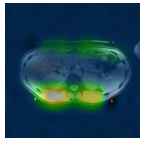	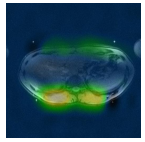	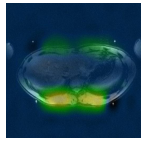	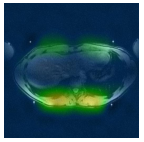	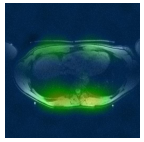

Table A.5

The top row shows the baseline metabolite maps overlaid on the anatomical images while the second and third row show the k_y undersampled, with no reconstruction, and k_y reconstructed metabolite maps, respectively. The foldover artifacts are easily seen in the middle row with the PCr peaks clearly seen outside of the abdomen of the subject. In the last row, we see the the reconstruction scheme has sufficiently suppressed the foldover aliasing.

HVOL1 Reconstruction Overlay Comparisons								
	Slice 1	Slice 2	Slice 3	Slice 4	Slice 5	Slice 6	Slice 7	Slice 8
Baseline	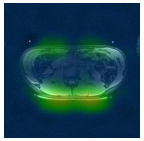	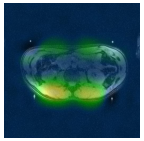	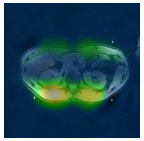	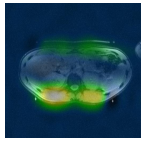	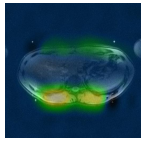	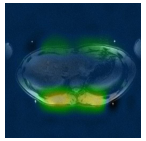	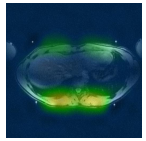	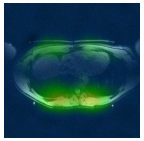
k_y No Reconstruction	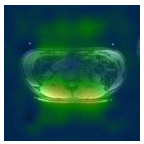	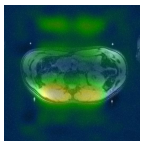	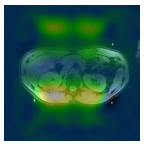	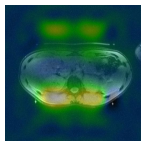	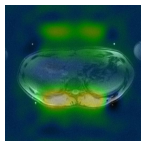	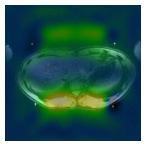	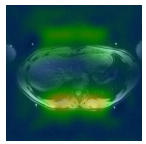	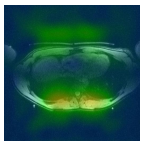
k_y Reconstruction	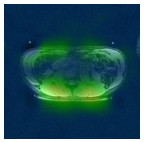	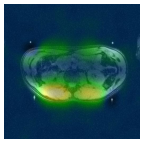	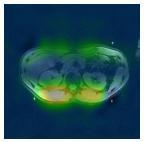	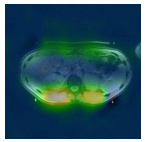	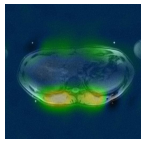	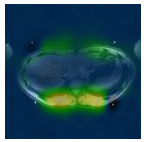	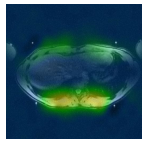	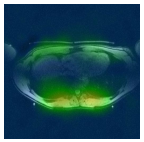

Table A.6

The top row of images contains eight MRI anatomical images of HVOL2 that correspond to the middle of the eight MRS slices; the middle row contains the metabolite maps of PCr; the bottom row contains an overlaid image of the first two rows.

HVOL2 Baseline Scans								
	Slice 1	Slice 2	Slice 3	Slice 4	Slice 5	Slice 6	Slice 7	Slice 8
MRI	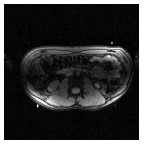	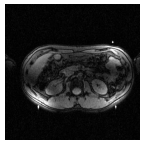	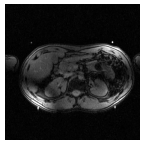	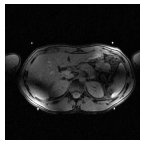	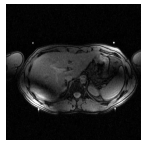	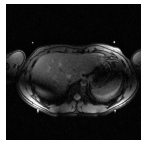	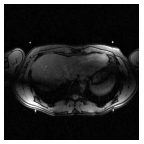	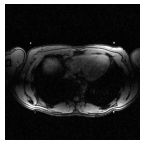
Metabolite Map	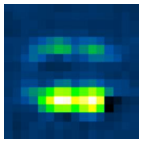	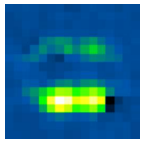	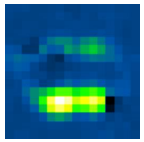	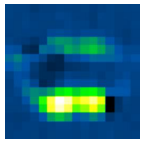	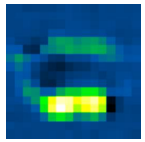	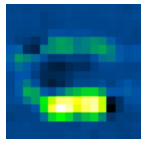	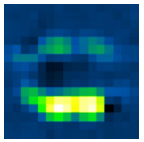	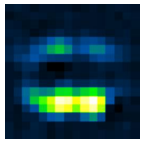
Interpolated Overlay	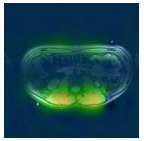	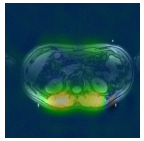	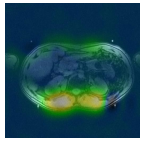	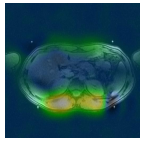	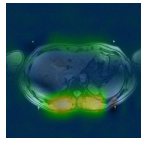	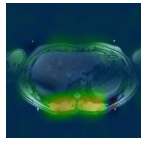	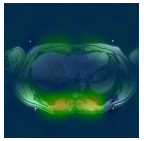	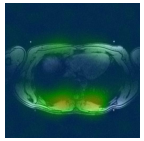

Table A.7

The top row shows the baseline metabolite maps overlaid on the anatomical images while the second and third row show the k_y undersampled, with no reconstruction, and k_y reconstructed metabolite maps, respectively. The foldover artifacts are easily seen in the middle row with the PCr peaks clearly seen outside of the abdomen of the subject. In the last row, we see the the reconstruction scheme has sufficiently suppressed the foldover aliasing.

HVOL2 k_y Reconstruction Overlay Comparisons								
	Slice 1	Slice 2	Slice 3	Slice 4	Slice 5	Slice 6	Slice 7	Slice 8
Baseline	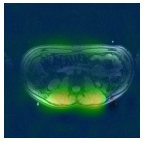	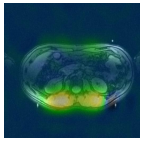	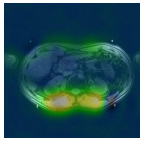	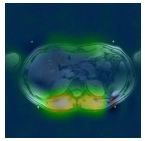	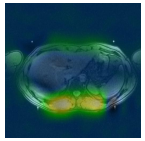	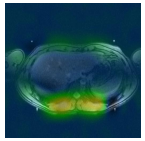	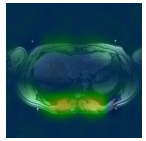	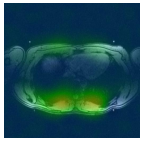
k_y No Reconstruction	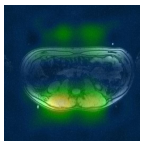	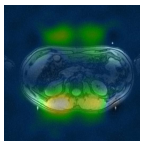	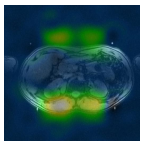	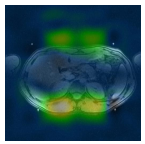	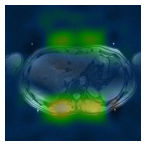	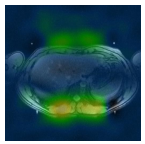	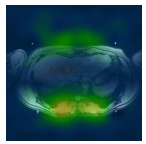	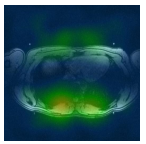
k_y Reconstruction	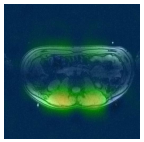	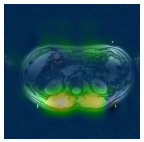	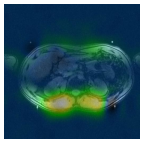	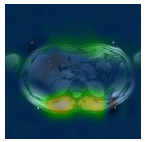	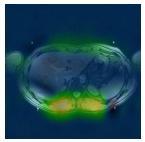	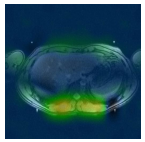	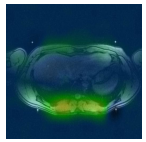	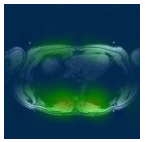

Table A.8

The top row shows the baseline metabolite maps overlaid on the anatomical images while the second and third row show the 2D undersampled, with no reconstruction, and 2D reconstructed metabolite maps, respectively. The foldover artifacts are easily seen in the middle row as the PCr peaks are clearly seen outside of the abdomen. In the last row, the reconstruction scheme has sufficiently suppressed the foldover aliasing. Note that the PCr signal is still only located in the muscular regions of the subject, absent in the liver.

HVOL2 2D GRAPPA Reconstruction on 3D Volume Comparisons								
	Slice 1	Slice 2	Slice 3	Slice 4	Slice 5	Slice 6	Slice 7	Slice 8
Baseline	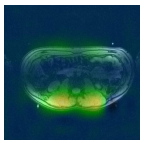	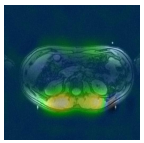	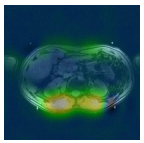	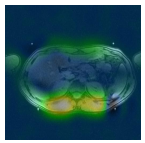	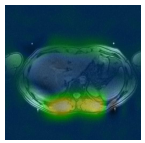	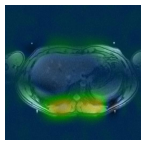	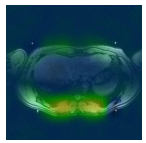	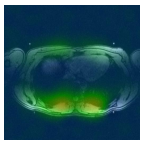
3D No Reconstruction	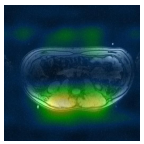	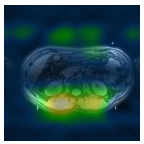	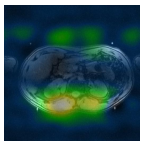	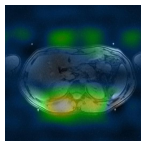	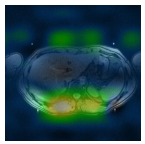	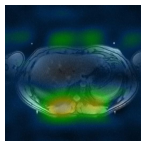	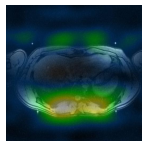	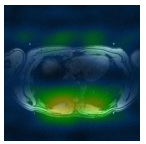
3D Reconstruction	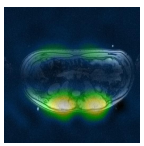	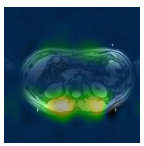	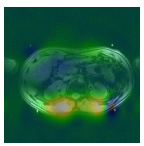	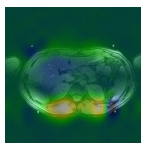	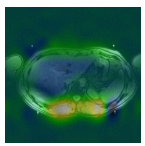	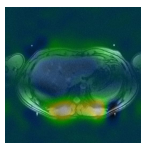	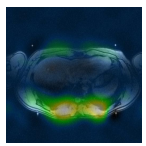	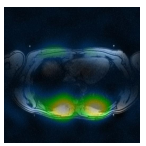

Table A.9

Spectral fitting of baseline scans compared to GRAPPA reconstructed scans

HVOL2 Fitting Results of Baseline Scans Compared to GRAPPA Reconstructions					
	Voxel (8,5)	Voxel (9,5)	Voxel (10,5)	Voxel (11,5)	Voxel (12,5)
Fully Sampled	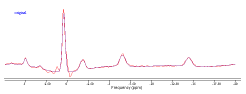	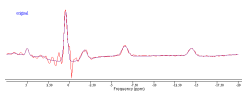	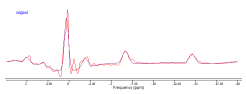	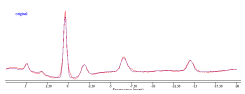	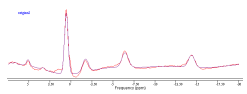
3D Reconstruction	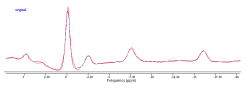	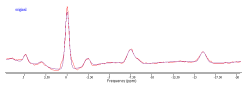	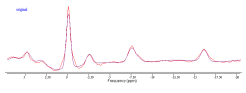	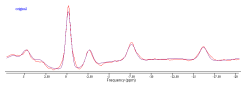	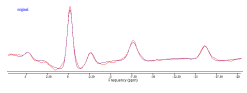

B. MRI Physics

B.1 Quantum Mechanics Review

Quantum mechanics plays an important role in the physics of NMR. With this being said, let's look at relevant NMR physics theory behind NMR. Please refer to Sections 4.3 and 4.4 of [49] for more information on the following basic fundamentals of quantum mechanics.

The governing equation for all of quantum mechanics is the time-dependent Schrödinger Equation which reads:

$$i\hbar\frac{\partial\Psi}{\partial t} = \hat{H}\Psi \tag{B.1}$$

Where Ψ is the wave function of a particle, $\hbar$ is defined as Planck's constant, h, divided by 2π:

$$\hbar = \frac{h}{2\pi} = 1.054572 \text{ x } 10^{-34} Js \tag{B.2}$$

and $\hat{H}$ is the Hamiltonian of the system, found by adding the kinetic energy and the potential energy of a system, giving the total energy of the system. Using the Dirac "bra-ket" notation, we could write the Schrödinger equation as:

$$i\hbar\frac{\partial}{\partial t}\left|\Psi(t)\right\rangle = \hat{H}\left|\Psi(t)\right\rangle \tag{B.3}$$

where $\left|\Psi(t)\right\rangle$ is the state of the system at a particular time, t.

One of the fundamental physical ideas behind NMR is the concept of angular momentum. According to classical mechanics, orbital angular momentum is given by:

$$\vec{L} = \vec{r} \times \vec{p} \tag{B.4}$$

If we replace the classical meanings of these with the quantum mechanical operator forms, we get the following equation:

$$\hat{\vec{L}} = \hat{\vec{r}} \times -i\hbar\vec{\nabla} \tag{B.5}$$

where $\vec{\hat{r}} = \langle x, y, z \rangle$ is the short hand notation for the quantum operator that multiplies a function by x, y, or z and $\vec{\nabla} = \langle \frac{\partial}{\partial x}, \frac{\partial}{\partial y}, \frac{\partial}{\partial z} \rangle$ is the short hand notation for the gradient operator.

The orbital angular momentum operators obey the following commutation relations:

$$\begin{aligned} [L_x, L_y] &= i\hbar L_z \\ [L_y, L_z] &= i\hbar L_x \\ [L_z, L_x] &= i\hbar L_y \\ \left[L^2, \vec{L}\right] &= 0 \end{aligned} \tag{B.6}$$

where we define $L^2 \equiv L_x^2 + L_y^2 + L_z^2$. Thus, since L^2 commutes with all components of $\vec{L}$, we can find eigenstates that are eigenstates of both L^2 and L_z with eigenvalues of $\hbar^2 l(l+1)$ and $\hbar m_l$, respectively. Where

$$\begin{aligned} l &= 0, \frac{1}{2}, 1, \frac{3}{2}, \ldots, n-1 \\ m_l &= -l, -l+1, \ldots, 0, \ldots, l-1, l \end{aligned} \tag{B.7}$$

We can see that these are three of the principal quantum numbers: n, l, and m_l.

Classical mechanics allows for two types of angular momentum: orbital and rotational. The rotational angular momentum is what we associate with spinning. So, for a particle such as an electron, we can say that it has an intrinsic spin, though it's not actually spinning. Quantum mechanics treats spin angular momentum similarly to that of orbital angular momentum. Thus, we can find the same relationships mentioned above:

$$\begin{aligned} [S_x, S_y] &= i\hbar S_z \\ [S_y, S_z] &= i\hbar S_x \\ [S_z, S_x] &= i\hbar S_y \\ \left[S^2, \vec{S}\right] &= 0 \end{aligned} \tag{B.8}$$

Similarly, we can define eigenstates for both S^2 and a component of S, S_z, such that they have eigenvalues $\hbar^2 s(s+1)$ and $\hbar m_s$, respectively. Here, s is the spin of the particle and can take on values:

$$\begin{aligned} s &= 0, \frac{1}{2}, 1, \frac{3}{2}, \dots \\ m_s &= -s, -l+1, \dots, 0, \dots, l-1, l \end{aligned} \tag{B.9}$$

Let us now introduce some notation which will allow us to proceed easier. Equations (B.10) through (B.13) were obtained from reference [50]. If there exists an observable, A, then the expectation value as a function of time is given by:

$$\langle A \rangle(t) = \langle \psi(t) | \, A \, | \psi(t) \rangle \tag{B.10}$$

where $|\psi(t)\rangle$ is the state vector describing the system at a time, t. The state vector can be expressed in terms of an orthonormal basis given by

$$|\psi(t)\rangle = \sum_n c_n(t) \, |u_n\rangle \tag{B.11}$$

Thus we see that the matrix elements of the observable, A, is given by

$$\langle u_n | \, A \, | u_p \rangle = A_{np} \tag{B.12}$$

And Equation B.10 can be rewritten as

$$\langle A \rangle(t) = \sum_{n,p} c_n^*(t) c_p(t) A_{np} \tag{B.13}$$

Often encountered in NMR is the idea of rotations. Hence, it's convenient to introduce rotation operators. They are defined as follows [51]:

$$\begin{aligned} \hat{R}_x(\Omega) &= \mathrm{e}^{\frac{-i\Omega \hat{S_x}}{\hbar}} \\ \hat{R}_y(\Omega) &= \mathrm{e}^{\frac{-i\Omega \hat{S_y}}{\hbar}} \\ \hat{R}_z(\Omega) &= \mathrm{e}^{\frac{-i\Omega \hat{S_z}}{\hbar}} \end{aligned} \tag{B.14}$$

where Ω is the angle about which we are going to rotate through and x, y, or z is the axis about which we rotate around.

B.2 Single spin-$\frac{1}{2}$ Particle

Let's now turn our attention to a specific case of a single particle of spin-$\frac{1}{2}$. In this case $s = \frac{1}{2}$ and from Equation B.9 we see that we can have two states of the form $|s, m_s\rangle$:

$$\begin{aligned} |u_+\rangle &= \left|\frac{1}{2}, +\frac{1}{2}\right\rangle \\ |u_-\rangle &= \left|\frac{1}{2}, -\frac{1}{2}\right\rangle \end{aligned} \tag{B.15}$$

Where we define $|u_+\rangle$ as spin-up and $|u_-\rangle$ as spin-down. One common notation is to define $|u_+\rangle$ as $|\alpha\rangle$ and $|u_-\rangle$ as $|\beta\rangle$ [23, 51]. This notation will be used throughout the remainder of this document.

For a spin-$\frac{1}{2}$ particle, we can write the state vector as

$$|\psi\rangle = c_\alpha |\alpha\rangle + c_\beta |\beta\rangle \tag{B.16}$$

where we normalize Equation B.16, giving $|c_\alpha|^2 + |c_\beta|^2 = 1$. This says that the spin-$\frac{1}{2}$ particle MUST be in either the spin-up state or the spin-down state or some combination of the two. If we define $|\alpha\rangle$ and $|\beta\rangle$ as two column vectors

$$|\alpha\rangle = \begin{pmatrix} 1 \\ 0 \end{pmatrix} \quad \text{and} \quad |\beta\rangle = \begin{pmatrix} 0 \\ 1 \end{pmatrix} \tag{B.17}$$

then it can be shown [49] that we can write the spin operators in the following form

$$\vec{S} = \frac{\hbar}{2}\vec{\sigma} \tag{B.18}$$

where $\vec{\sigma}$ is the shorthand notation for writing the Pauli matrices:

$$\sigma_x = \begin{pmatrix} 0 & 1 \\ 1 & 0 \end{pmatrix} \quad \sigma_y = \begin{pmatrix} 0 & -i \\ i & 0 \end{pmatrix} \quad \sigma_z = \begin{pmatrix} 1 & 0 \\ 0 & -1 \end{pmatrix} \tag{B.19}$$

We can now see that if we take Equation B.14 and we want to rotate a spin-$\frac{1}{2}$ particle around an arbitrary vector $\vec{u}$ through an angle Ω, then we can write [50]:

$$\begin{aligned} \hat{R}_{\vec{u}}(\Omega) &= \mathrm{e}^{\frac{-i}{\hbar}\Omega\hat{\vec{S}}\cdot\hat{\vec{u}}} \\ &= \mathrm{e}^{\frac{-i}{2}\Omega\hat{\vec{\sigma}}\cdot\hat{\vec{u}}} \end{aligned} \tag{B.20}$$

and has the matrix form, using the spin-$\frac{1}{2}$ basis of $|\alpha\rangle$ and $|\beta\rangle$:

$$\hat{R}_{\vec{u}}(\Omega) = \begin{pmatrix} \cos\left(\frac{\Omega}{2}\right) - iu_z \sin\left(\frac{\Omega}{2}\right) & (-iu_x - u_y)\sin\left(\frac{\Omega}{2}\right) \\ (-iu_x + u_y)\sin\left(\frac{\Omega}{2}\right) & \cos\left(\frac{\Omega}{2}\right) + iu_z \sin\left(\frac{\Omega}{2}\right) \end{pmatrix} \tag{B.21}$$

The rotation matrix has the property that it's inverse is the rotation through the given angle in the opposite direction:

$$\hat{R}_{\vec{u}}^{-1}(\Omega) = \hat{R}_{\vec{u}}(-\Omega) \tag{B.22}$$

The idea of rotation will become more important later when we talk about "flipping" the magnetization of molecules within the human body to acquire MRI or MRS data and the precession of spins about the magnetic field.

To see that there will be some spin precession about some axis (we will choose the $\hat{z}$ axis by convention) we look back at Equation B.1 to view the dynamics of a particular spin state. For a spin-$\frac{1}{2}$ particle at rest in a magnetic field pointing along the $\hat{z}$ axis, the Hamiltonian becomes just the potential of the system (since the kinetic energy term is zero). From classic electromagnetism, we know that this will be given by

$$\hat{H}_{static} = -\vec{\mu} \cdot \vec{B} \tag{B.23}$$

where $\vec{\mu}$ is the magnetic dipole moment and is related to the spin of a particle by:

$$\vec{\mu} = \gamma \vec{S} \tag{B.24}$$

where γ is the gyromagnetic ratio and is dependent on the particle in question. So, replacing $\vec{\mu}$ in Equation B.23 we get

$$\begin{aligned} \vec{H}_{static} &= -\gamma \vec{B} \cdot \vec{S} \\ &= -\gamma(B_x \hat{S}_x + B_z \hat{S}_x + B_z \hat{S}_z) \\ &= -\gamma B_0 \hat{S}_z \\ &= -\omega_L \hat{S}_z \end{aligned} \tag{B.25}$$

The last two lines are found from assuming a magnetic field directed along the z-axis with strength B_0 and ω_L is called the Larmor frequency. Substituting this result into

Equation B.1 and solving the first order differential equation, we obtain a solution of the form:

$$|\psi(t)\rangle = \hat{R}_z(\omega_L t)\,|\psi_0\rangle \tag{B.26}$$

This result shows that there will be some rotation of the initial spin $|\psi_0\rangle$ about the $\hat{z}$ axis through the angle ωt. ω is referred to as the Larmor frequency and plays a vital role in the acquisition of MRI data.

Now let's take a look at a special case of the rotation operator acting on the $|\alpha\rangle$ state (pointed along the $\hat{z}$ direction), rotating it around the $\hat{z}$ axis through the angle ωt. The result of this rotation is that our spin remains in the $|\alpha\rangle$ state but picks up an additional phase factor, as seen from Equation B.21 and substituting $u_z = 1$ [51]:

$$|\psi(t)\rangle = \mathrm{e}^{-\frac{i}{2}\omega t}\,|\alpha\rangle \tag{B.27}$$

This phase factor plays an important role in the T_2 dephasing time constant, discussed later.

It is sometimes easier and more convenient to analyze our system from the perspective of a rotating lab frame. What we have looked at up until this point is from a stationary lab frame, allowing the spin to move about a stationary z-axis. Now, if we choose a frame in which we move at the same frequency, ω, as our spins, they will look stationary. Let's call the stationary frame coordinates: $\langle x, y, z\rangle$ and the rotating frame coordinates $\langle x', y', z'\rangle$. We can relate these coordinates by [51]:

$$\begin{aligned} \hat{x}' &= \hat{x}\cos\left(\Phi(t)\right) + \hat{y}\sin\left(\Phi(t)\right) \\ \hat{y}' &= -\hat{x}\sin\left(\Phi(t)\right) + \hat{y}\cos\left(\Phi(t)\right) \\ \hat{z}' &= \hat{z} \end{aligned} \tag{B.28}$$

where $\Phi(t)$ is defined as

$$\Phi(t) = \omega_{ref} t + \phi_{ref} \tag{B.29}$$

and ϕ_{ref} is the phase angle of the reference frame.

With these definitions in place we can find the wave function of our spin in the rotating frame as well as the rotating frame Schrödinger equation [51]:

$$\begin{aligned} \underline{|\psi(t)\rangle} &= \hat{R}_z(-\Phi)\,|\Psi\rangle \\ i\hbar\frac{\mathrm{d}}{\mathrm{d}t}\underline{|\Psi(t)\rangle} &= \underline{\hat{H}}\ \underline{|\Psi(t)\rangle} \end{aligned} \tag{B.30}$$

where the underline notation represents values with respect to the rotating frame of reference. It remains to define $\underline{\hat{H}}$:

$$\underline{\hat{H}} = \hat{R}_z(-\Phi)\hat{H}\hat{R}_z(\Phi) - \omega_{ref}\hat{S}_z \tag{B.31}$$

Which was obtained by combining Equation B.30, it's inverse, and Equation B.1. Also of note is that this is any Hamiltonian that may be appropriate for whatever system is under study. We will come back to use this equation later.

A spin can precess in the rotating frame as well if the Larmor frequency does not match that of the rotating frame of reference. A spin with a Larmor frequency greater than that of the angular frequency of the rotating frame ($\omega_L > \omega_{ref}$) will appear to precess slowly about the z-axis while a spin with a Larmor frequency less than the angular frequency of the rotating frame ($\omega_L < \omega_{ref}$) will appear to spin backwards around the z-axis. This can be summarized with the relative Larmor frequency (also called the frequency offset or the resonance offset) [51]

$$\Omega_L = \omega_L - \omega_{ref} \tag{B.32}$$

Thus, for a stationary spin-$\frac{1}{2}$ particle, the rotating spin Hamiltonian can be written:

$$\underline{\hat{H}_{static}} = -\Omega_L\hat{S}_z \tag{B.33}$$

which is analogous to the last line of Equation B.25.

B.3 External RF Fields

(Please see [51] for more information on this section)

Up until this point we have only looked at situations where the only magnetic field in question was the one produced by the MRI scanner itself, also known as the static

B_0 field. A required factor in performing MRI or MRS experiments is the external RF field that we subject our spins to. This field is provided by an external source, called a coil. This coil produces an "external" RF field within the specimen that interacts with the spin, applies a torque, and flips the spin. The external field must be directed perpendicular to the main field. Generally, the B_0 field points along the z-axis and the RF field will be in the xy-plane.

Let's investigate the case in which the RF B-field oscillates along the x-axis. Then the magnetic field would be given by:

$$\vec{B}_{RF}(t) = B_{RF}\cos\left(\omega_{coil}t + \phi_p\right)\hat{x} \tag{B.34}$$

where B_{RF} is the amplitude of the RF pulse, ϕ_p is the phase angle of the pulse, and ω_{coil} is the angular frequency of the receiving coil. This RF field will only act during the time of the RF pulse and ω_{coil} should closely match the resonant frequency of the molecule used for MRI or MRS (i.e., ^{1}H or ^{31}P).

It is often convenient to think of the oscillating RF field as two vectors rotating in opposite directions:

$$\begin{gathered}\vec{B}_{RF}(t) = \vec{B}^{res}_{RF}(t) + \vec{B}^{non-res}_{RF}(t) \\ \text{where} \\ \vec{B}^{res}_{RF}(t) = \frac{1}{2}B_{RF}\left[\cos\left(\omega_{coil}t + \phi_p\right)\hat{x} + \sin\left(\omega_{coil}t + \phi_p\right)\hat{y}\right] \\ \vec{B}^{non-res}_{RF}(t) = \frac{1}{2}B_{RF}\left[\cos\left(\omega_{coil}t + \phi_p\right)\hat{x} - \sin\left(\omega_{coil}t + \phi_p\right)\hat{y}\right]\end{gathered} \tag{B.35}$$

$\vec{B}^{res}_{RF}(t)$ will rotate in the same direction as the Larmor frequency and gives the desired resonance effect. $\vec{B}^{non-res}_{RF}(t)$, on the other hand, rotates in the opposite direction as the Larmor frequency and tends to have no effect on the spins of the system. Hence, we can ignore it and write the RF Hamiltonian using Equation B.25 and ignoring the non-resonant rotation:

$$\hat{H}_{RF} \cong -\frac{1}{2}\gamma B_{RF}\left[\cos\left(\omega_{coil}t + \phi_p\right)\hat{S}_x + \sin\left(\omega_{coil}t + \phi_p\right)\hat{S}_y\right] \tag{B.36}$$

This gives the full Hamiltonian as the summation of the spin Hamiltonian, given in Equation B.25, and the RF Hamiltonian:

$$\hat{H}_{static,RF} = \hat{H}_{static} + \hat{H}_{RF} \tag{B.37}$$

We can use the following formula for cyclicly commuting operators $\hat{A}, \hat{B}$, and $\hat{C}$ to simplify the expression for the RF field Hamiltonian.

$$\mathrm{e}^{-i\theta\hat{A}}\hat{B}\mathrm{e}^{i\theta\hat{A}} = \hat{B}\cos(\theta) + \hat{C}\sin(\theta) \tag{B.38}$$

This equation tells us that we rotate the operator $\hat{B}$ about operator $\hat{A}$ through some angle θ. With this relationship in hand, and replacing $\hat{A}, \hat{B}$, and $\hat{C}$ with $\hat{S}_x, \hat{S}_y$, and $\hat{S}_z$ respectively, we can write this as

$$\mathrm{e}^{-i\theta\hat{S}_x}\hat{S}_y\mathrm{e}^{i\theta\hat{S}_x} = \hat{S}_y\cos(\theta) + \hat{S}_z\sin(\theta) \tag{B.39}$$

Looking at Equation B.36, we see that the RHS is just a cyclic permutation of the above equation with $\theta = \omega_{coil}t + \phi_p$ which we will now define as

$$\Phi_p(t) \equiv \omega_{coil}t + \phi_p \tag{B.40}$$

Giving us, dropping the time dependence for convenience

$$\begin{aligned}\hat{H}_{RF} &\cong -\frac{1}{2}\gamma B_{RF}\left[\cos(\Phi_p)\hat{S}_x + \sin(\Phi_p)\hat{S}_y\right] \\ &= -\frac{1}{2}\gamma B_{RF}\left[\mathrm{e}^{-i\Phi_p\hat{S}_z}\hat{S}_x\mathrm{e}^{i\Phi_p\hat{S}_z}\right]\end{aligned} \tag{B.41}$$

Now, if we recognize that the exponentials in the bracket are just the rotation operators, then we can again rewrite this as:

$$\hat{H}_{RF} = -\frac{1}{2}\gamma B_{RF}\hat{R}_z(\Phi_p)\hat{S}_x\hat{R}_z(-\Phi_p) \tag{B.42}$$

which gives us a simplified expression for the combined static and RF fields Hamiltonian:

$$\hat{H}_{static,RF} = \omega_L\hat{S}_z - \frac{1}{2}\gamma B_{RF}\hat{R}_z(\Phi_p)\hat{S}_x\hat{R}_z(-\Phi_p) \tag{B.43}$$

Now, if we want to know what this Hamiltonian looks like in the rotating reference frame, then we use Equation B.31 with our Hamiltonian being the simplified form of the combined static/RF pulse Hamiltonian:

$$\underline{\hat{H}_{static,RF}} = -\frac{1}{2}\gamma B_{RF}\hat{R}_z(\Phi_p - \Phi)\hat{S}_x\hat{R}_z(\Phi - \Phi_p) + (\omega_L - \omega_{ref})\hat{S}_z \tag{B.44}$$

and substituting in equations (B.40), (B.32), and (B.29) we get:

$$\underline{\hat{H}_{static,RF}} = -\frac{1}{2}\gamma B_{RF}\hat{R}_z(\phi_p - \phi_{ref})\hat{S}_x\hat{R}_z(\phi_{ref} - \phi_p) + \Omega_L\hat{S}_z \tag{B.45}$$

after substituting $\omega_{coil} = \omega_{ref}$. Notice that once we do this, we have gotten rid of the time dependence. This seems an appropriate substitution because our rotating reference frame should be rotating at the Larmor frequency of the nucleus in question, ^{31}P in our case. The coil is set to the appropriate frequency, so ω_{coil} should also be set to the Larmor frequency, ω_L. With this substitution the magnetization no longer seems to precess around the z-axis, but instead is stationary.

One final simplification can be made to Equation B.45. According to reference [51], we can set ϕ_{ref}=0 or $\phi_{ref} = \pi$, either of which will give the same equation below:

$$\underline{\hat{H}_{static,RF}} \cong \omega_{nut}\hat{R}_z(\phi_p)\hat{S}_x\hat{R}_z(-\phi_p) + \Omega_L\hat{S}_z$$
$$\text{where} \tag{B.46}$$
$$\omega_{nut} = |\frac{1}{2}B_{RF}|$$

B.4 Chemical Shift

(Please see [51] for more information on this section)

The static B_0 field made by the scanner will have an important effect on molecules inside the scanner. The electrons inside the electron cloud surrounding the molecule will begin to flow around the molecule and produce currents within the electron cloud, which in turn induces a magnetic field around the molecule. This induced magnetic field will either shield or enhance the B_0 field felt by the nucleus of the molecule in question. This process is known as the chemical shift. The local magnetic field felt by the nucleus is then:

$$\vec{B}_{loc} = \vec{B}_0 + \vec{B}_{ind} \tag{B.47}$$

We can approximate the induced B-field as being linear with respect to the B_0 field and define it as:

$$\vec{B}_{ind} = \vec{\delta}(\theta) \cdot \vec{B}_0 \tag{B.48}$$

where $\vec{\delta}(\theta)$ is called the chemical shift tensor and can be written as

$$\vec{\delta}(\theta) = \begin{pmatrix} \delta_{xx}(\theta) & \delta_{xy}(\theta) & \delta_{xz}(\theta) \\ \delta_{yx}(\theta) & \delta_{yy}(\theta) & \delta_{yz}(\theta) \\ \delta_{zx}(\theta) & \delta_{zy}(\theta) & \delta_{zz}(\theta) \end{pmatrix} \tag{B.49}$$

and so we can rewrite Equation B.48 as, using the B_0 field pointing along the z-axis:

$$\begin{pmatrix} B_{ind,x} \\ B_{ind,y} \\ B_{ind,z} \end{pmatrix} = \begin{pmatrix} \delta_{xx}(\theta) & \delta_{xy}(\theta) & \delta_{xz}(\theta) \\ \delta_{yx}(\theta) & \delta_{yy}(\theta) & \delta_{yz}(\theta) \\ \delta_{zx}(\theta) & \delta_{zy}(\theta) & \delta_{zz}(\theta) \end{pmatrix} \cdot \begin{pmatrix} 0 \\ 0 \\ B_0 \end{pmatrix}$$

$$\text{thus} \tag{B.50}$$

$$\begin{pmatrix} B_{ind,x} \\ B_{ind,y} \\ B_{ind,z} \end{pmatrix} = \begin{pmatrix} \delta_{xz}(\theta)B_0 \\ \delta_{yz}(\theta)B_0 \\ \delta_{zz}(\theta)B_0 \end{pmatrix}$$

The Hamiltonian for a chemically shifted molecule then becomes, again referring back to Equation B.25:

$$\begin{aligned} \hat{H}_{CS} &= -\hat{\vec{\mu}} \cdot \vec{B}_{ind} \\ &= -\gamma[\delta_{xz}(\theta)B_0\hat{S}_x + \delta_{yz}(\theta)B_0\hat{S}_y + \delta_{zz}(\theta)B_0\hat{S}_z] \end{aligned} \tag{B.51}$$

With the secular approximation, we can reduce this equation to a more simplified form:

$$\hat{H}_{CS} \cong -\gamma\delta_{zz}(\theta)B_0\hat{S}_z \tag{B.52}$$

which only takes into account the z-component of the induced field.

For isotropic liquids we can write the isotropic chemical shift Hamiltonian

$$\hat{H}_{CS,iso} = -\gamma B_0\delta_{iso}\hat{S}_z \tag{B.53}$$

where

$$\delta_{iso} = \frac{1}{3}\left[\delta_{xx} + \delta_{yy} + \delta_{zz}\right] \tag{B.54}$$

which gives us the combined Hamiltonian for a single spin in an isotropic liquid

$$\begin{aligned} \hat{H}_{spin,CS} &= \hat{H}_{spin} + \hat{H}_{CS,iso} \\ &= -\gamma B_0 \left[\hat{S}_z + \delta_{iso}\hat{S}_z\right] \\ &= \omega_{L,CS}\hat{S}_z \end{aligned} \tag{B.55}$$

where $\omega_{L,CS}$ is called the chemically shifted Larmor frequency and is defined as

$$\omega_{L,CS} = -\gamma B_0(1 + \delta_{iso}) \tag{B.56}$$

We can see from Equation B.51 that the induced field isn't always going to be parallel to the B_0 field. In fact, the induced field depends on the geometry of the molecule within the B_0 field as well as the location of the nucleus within the molecule. This position and orientation has been emphasized by adding (θ) to each term within the tensor. It's because of the dependence upon position that helps explain why molecules can have different peaks in a spectrum (ATP, for example). This molecule affects it's different nuclear centers through shielding and will shift the peaks from different nuclear sites to different spectrum positions (α-ATP, β-ATP, and γ-ATP). Not only is the chemical shift dependent on orientation and position, but it is also dependent on the environment that contains the molecule in question [52].

This shift in peaks allows us to plot the different resonance peaks on a spectrum, with different molecules having different peak positions. For example, α-ATP is located at a position -7.52 ppm; β-ATP at -16.26 ppm; γ-ATP at -2.48 ppm. Here, ppm stands for part per million and is a typical unit for the chemical shift spectrum, instead of measurements made in Hz. We can relate ppm to Hz by the following equation:

$$\text{ppm} = \frac{f - f_{ref}}{f_{ref}} \text{ x } 10^6 \tag{B.57}$$

where f_{ref} is the frequency of a reference molecule. When using ^{31}P, PCr is typically used as the reference molecule since it does not have any pH dependence (which could

potentially shift the peaks even more) like some other ^{31}P molecules. Since PCr will be used as the reference, it will be located at 0 ppm in all ^{31}P spectra.

B.5 Density Operator

In Section B.2, we looked at single particles of spin-$\frac{1}{2}$ and now we turn to the more physical case of an ensemble of spin-$\frac{1}{2}$ particles. In doing so, it is convenient to introduce the concept of the density operator. With the definitions from Section B.1, it can be shown, see reference [50], that we can rewrite Equation B.13 in terms of the density operator, $\hat{\rho}$:

$$\langle A \rangle(t) = \mathrm{Tr}\{\hat{\rho}(t)A\} \tag{B.58}$$

A more formal definition of the density operator is given by:

$$\begin{aligned} \hat{\rho} &= \sum_i p_i \hat{\rho}_i \\ \hat{\rho}_i &= |\psi_i\rangle \langle\psi_i| \end{aligned} \tag{B.59}$$

where p_i is the probability of finding the system in the state $|\psi_i\rangle$. Since $\hat{\rho}$ is an operator we can find a matrix representation for it where the elements are given by:

$$\begin{aligned} \hat{\rho}_{nm} &= \sum_i p_i \langle u_n \,|\, \psi_i\rangle \langle \psi_i \,|\, u_m\rangle \\ &= \sum_i p_i c_n^{(i)*} c_m^{(i)} \end{aligned} \tag{B.60}$$

where $c_m^{(i)}$ is the component or projection of $|u_m\rangle$ onto $|\psi_i\rangle$ given by $\langle u_m \,|\, \psi_i\rangle$.

The diagonal elements of $\hat{\rho}$ are called the "pure" states and the off-diagonal terms are called the "coherence" states. The diagonal elements give the population of the state in question. For example, the element $\hat{\rho}_{mm}$ gives the population of the state $|u_m\rangle$. When the off diagonal elements, or the coherence states elements, are nonzero, there is a coherence between the states in question.

For the case of an ensemble of spin-$\frac{1}{2}$ particles then the states in question are still $|\alpha\rangle$, $|\beta\rangle$, or some superposition of the two states. Thus, a physical meaning to the pure states would be an ensemble of spin-$\frac{1}{2}$ particles whose net magnetization is

either $|\alpha\rangle$, the upper diagonal element, or $|\beta\rangle$, the lower diagonal element. A physical interpretation of the coherence states would be that of transverse magnetization. If the off-diagonal elements are nonzero, then we can say that the net magnetization lies somewhere in the xy-plane (either rotating or stationary frame). The actual direction can be found by looking at the imaginary plane, since the coherences are complex numbers, and finding in where the coherence lies on the imaginary plane. Since the off diagonal terms are just complex conjugates of one another, then we don't obtain new information by looking at both elements: we need only look at one of them.

One final matter of note is the definition of the density operator in the rotating frame. From the last line of Equation B.59 we can similarly say that the rotating frame density operator is:

$$\begin{aligned} \underline{\hat{\rho}} &= \sum_i p_i \underline{\hat{\rho}_i} \\ \underline{\hat{\rho}_i} &= \underline{|\psi_i\rangle\langle\psi_i|} \\ &= \hat{R}_z(-\Phi)\hat{\rho}\hat{R}_z(\Phi) \end{aligned} \tag{B.61}$$

An important example, found in numerous textbooks [50, 51, 53], is that of thermal equilibrium. If we consider a system at thermal equilibrium with a reservoir at temperature T, then we can say that the density operator is given by [50]

$$\hat{\rho} = Z^{-1}\mathrm{e}^{-\frac{\hat{H}}{k_B T}} \tag{B.62}$$

where $\hat{H}$ is the Hamiltonian of our system , k_B is the Boltzmann constant, and Z is the partition function and is defined as:

$$Z = \mathrm{Tr}\left[\mathrm{e}^{-\frac{\hat{H}}{k_B T}}\right] \tag{B.63}$$

For an ensemble of spin-$\frac{1}{2}$ particles with the basis states of $|\alpha\rangle$ and $|\beta\rangle$, we can write the density matrix elements as:

$$[\hat{\rho}] = \begin{pmatrix} \langle\alpha|\,\hat{\rho}\,|\alpha\rangle & \langle\alpha|\,\hat{\rho}\,|\beta\rangle \\ \langle\beta|\,\hat{\rho}\,|\alpha\rangle & \langle\beta|\,\hat{\rho}\,|\beta\rangle \end{pmatrix} \tag{B.64}$$

Recall that:

$$\begin{aligned} \hat{\rho}\,|\alpha\rangle &= Z^{-1}\mathrm{e}^{-\frac{E_\alpha}{k_B T}}\,|\alpha\rangle \\ \hat{\rho}\,|\beta\rangle &= Z^{-1}\mathrm{e}^{-\frac{E_\beta}{k_B T}}\,|\beta\rangle \end{aligned} \tag{B.65}$$

and that $|\alpha\rangle$ and $|\beta\rangle$ are orthonormal to each other. Therefore, the coherences are zero and we only have pure states at thermal equilibrium. We can simplify things with the following substitutions:

$$Z = \mathrm{e}^{-\frac{E_\alpha}{k_B T}} + \mathrm{e}^{-\frac{E_\beta}{k_B T}} \tag{B.66}$$

where

$$\begin{aligned} E_\alpha &= -\hbar\omega_L \\ E_\beta &= \hbar\omega_L \end{aligned} \tag{B.67}$$

giving us

$$\begin{aligned} Z &= \mathrm{e}^{\frac{\hbar\omega_L}{k_B T}} + \mathrm{e}^{-\frac{\hbar\omega_L}{k_B T}} \\ &= \mathrm{e}^{\frac{\hbar\gamma B_0}{k_B T}} + \mathrm{e}^{-\frac{\hbar\gamma B_0}{k_B T}} \end{aligned} \tag{B.68}$$

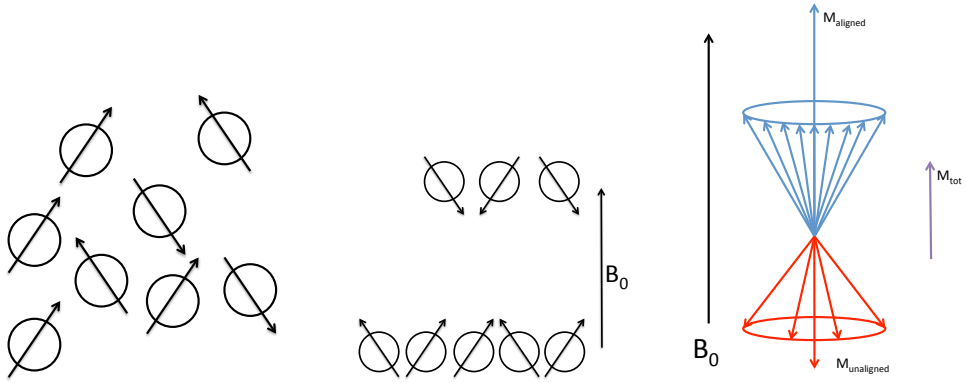

(a) No B_0 field (b) B_0 field applied (c) M_{tot} points along B_0

Figure B.1. Here we see that the applied laboratory field, B_0, separates the molecules into aligned and anti-aligned molecules. This is mathematically demonstrated in Equation B.69. The last figure shows that the total magnetization is the sum of the magnetic moments of all the individual particles in the ensemble.

Therefore, the general density matrix operator for an ensemble for spin-$\frac{1}{2}$ particles at thermal equilibrium, with an applied B_0 field, can be written as:

$$[\hat{\rho}] = \frac{1}{\mathrm{e}^{\frac{\hbar\gamma B_0}{k_B T}} + \mathrm{e}^{-\frac{\hbar\gamma B_0}{k_B T}}} \begin{pmatrix} \mathrm{e}^{\frac{\hbar\gamma B_0}{k_B T}} & 0 \\ 0 & \mathrm{e}^{-\frac{\hbar\gamma B_0}{k_B T}} \end{pmatrix} \tag{B.69}$$

Simplification can be made by expanding the exponentials in a power series and ignoring the higher order terms, the denominator becomes approximately 2, and the matrix operator becomes

$$\begin{aligned}[\hat{\rho}] &= \begin{pmatrix} \frac{1}{2} + \frac{1}{4}\frac{\hbar\gamma B_0}{k_B T} & 0 \\ 0 & \frac{1}{2} - \frac{1}{4}\frac{\hbar\gamma B_0}{k_B T} \end{pmatrix} \\ &= \frac{1}{2}\hat{I} + \frac{1}{2}\frac{\gamma B_0}{k_B T}\hat{S}_z \end{aligned} \tag{B.70}$$

where $\hat{I}$ is the identity matrix. This result shows that a subject at thermal equilibrium will have a slightly higher population in the $|\alpha\rangle$ state. This means that the net magnetization will point along the B_0 field axis. In the next section the magnetization will be discussed in more detail.

B.6 Magnetization

We can define the magnetization in terms of the density operators. First we define the magnetization (in the rotating frame) as

$$\underline{\vec{M}} = M_x\hat{x}' + M_y\hat{y}' + M_z\hat{z}' \tag{B.71}$$

The z-component of the magnetization vector can be thought of as the difference in the $|\alpha\rangle$ and $|\beta\rangle$ states, M_x is the real portion of the coherence states, and M_y is the imaginary part of the coherence states. Mathematically, these can be written as:

$$\begin{aligned} M_z &= \rho_\alpha - \rho_\beta \\ M_x &= \mathrm{Re}(\rho_{coh}) \\ M_y &= \mathrm{Im}(\rho_{coh}) \end{aligned} \tag{B.72}$$

where ρ_α is the population of the spin-up state, $|\alpha\rangle$, ρ_β is the population of the spin-down state $|\beta\rangle$, and ρ_{coh} is the population of the coherence states, the off-diagonal terms of the density matrix. See Figure B.2 for a graphical description. We can

(a) Schematic showing the graphical descriptions of M_x and M_y

(b) The direction of M_{trans} is determined by ρ_{coh}

Figure B.2. M_{trans} is determined by the real and imaginary parts of the off-diagonal density matrix elements, the coherence states, as described in Equation B.72

normalize these factors so that the magnetization vector at thermal equilibrium is a unit vector pointing along the z-axis. This gives the following:

$$\begin{aligned} \vec{M}_{eq} &= \hat{z}' \\ M_z &= \frac{2k_BT}{\hbar\gamma B_0}(\rho_\alpha - \rho_\beta) \\ M_x &= \frac{4k_BT}{\hbar\gamma B_0}\mathrm{Re}(\rho_{coh}) \\ M_y &= \frac{4k_BT}{\hbar\gamma B_0}\mathrm{Im}(\rho_{coh}) \end{aligned} \tag{B.73}$$

Thus we can write the spin density operator as:

$$\hat{\rho} = \frac{1}{2}\hat{I} + \frac{1}{2}\frac{\gamma B_0}{k_BT}\vec{M}\cdot\vec{S} \tag{B.74}$$

Now, if we were to apply an external RF pulse in such a way as described in Section B.3, then the net result of this action will be to "flip" the magnetization vector. Two important examples of magnetization transformation/rotation follow.

The $\hat{R}_x(\pi)$ rotation will have the affect of rotating the thermal equilibrium magnetization vector around the x-axis by an angle of π. This is known as one possible

180° The new density matrix can be found by applying the rotation, using Equation B.21 [51]:

$$\begin{aligned}\rho_f &= \hat{R}_x(\pi)\rho_{eq}\hat{R}_x(-\pi) \\ &= \begin{pmatrix} 0 & -i \\ -i & 0 \end{pmatrix} \begin{pmatrix} \frac{1}{2}+\frac{1}{4}\frac{\hbar\gamma B_0}{k_B T} & 0 \\ 0 & \frac{1}{2}-\frac{1}{4}\frac{\hbar\gamma B_0}{k_B T} \end{pmatrix} \begin{pmatrix} 0 & i \\ i & 0 \end{pmatrix} \\ &= \begin{pmatrix} \frac{1}{2}-\frac{1}{4}\frac{\hbar\gamma B_0}{k_B T} & 0 \\ 0 & \frac{1}{2}+\frac{1}{4}\frac{\hbar\gamma B_0}{k_B T} \end{pmatrix}\end{aligned} \tag{B.75}$$

Thus, the magnetization vector has been flipped by 180 degrees, inverting the populations of the $|\alpha\rangle$ and $|\beta\rangle$ states. This can be seen in Figure B.3. Figure B.4 shows how

(a) Pre-RF Pulse; M_0 is aligned with B_0

(b) Post-RF Pulse; M_0 is now anti-aligned with B_0

Figure B.3. Before the RF pulse with energy ΔE is absorbed, the majority of particles are in the lower energy state: aligned with B_0. After the 180° pulse M_0 is anti-aligned with B_0 due to the majority of particles moving to the upper energy state after absorption of the RF pulse.

the M_{long}, or rather the M_z, component evolves with time. After the 180° pulse, the longitudinal magnetization exponentially grows back towards it's equilibrium value, M_0. This relaxation is covered in more detail in Section B.7.

Another important example is that of a 90º pulse. One can achieve this result, in one way, by using the rotation operator, $\hat{R}_x(\frac{\pi}{2})$. This will flip the magnetization to point along the negative y-axis [51]:

$$\begin{aligned}\rho_f &= \hat{R}_x(\frac{\pi}{2})\rho_{eq}\hat{R}_x(-\frac{\pi}{2}) \\ &= \begin{pmatrix} \cos\left(\frac{\pi}{4}\right) & -i\sin\left(\frac{\pi}{4}\right) \\ -i\sin\left(\frac{\pi}{4}\right) & \cos\left(\frac{\pi}{4}\right) \end{pmatrix} \begin{pmatrix} \frac{1}{2}+\frac{1}{4}\frac{\hbar\gamma B_0}{k_B T} & 0 \\ 0 & \frac{1}{2}-\frac{1}{4}\frac{\hbar\gamma B_0}{k_B T} \end{pmatrix} \begin{pmatrix} \cos\left(\frac{-\pi}{4}\right) & -i\sin\left(\frac{-\pi}{4}\right) \\ -i\sin\left(\frac{-\pi}{4}\right) & \cos\left(\frac{-\pi}{4}\right) \end{pmatrix} \\ &= \begin{pmatrix} \frac{1}{2} & i\frac{\hbar\gamma B_0}{k_B T} \\ -i\frac{\hbar\gamma B_0}{k_B T} & \frac{1}{2} \end{pmatrix}\end{aligned} \tag{B.76}$$

Thus the longitudinal magnetization is now zero because there are just as many spin-$\frac{1}{2}$ particles in the spin-up state as there are in the spin-down state. Notice that the coherence states now contain only imaginary terms and therefore the magnetization only points along the y-axis. It is in this state that the transverse magnetization is the strongest.

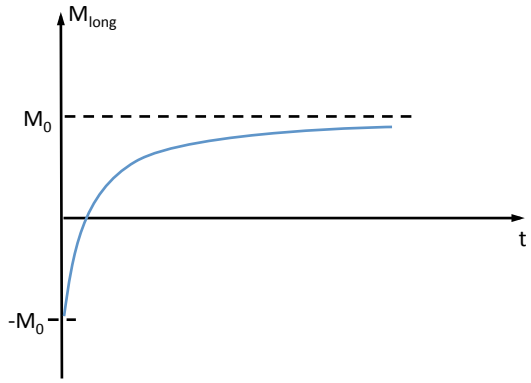

Figure B.4. For a 180° RF pulse the M_{long} is flipped from it's original M_0 position to the -M_0 position and exponentially grows back to M_0 over time.

B.7 Relaxation

Before taking relaxation effects into account, first we shall ignore these effects for simplicity. As mentioned before, if we subject a spin-$\frac{1}{2}$ particle to a B_0 field directed along the z-axis, then it will precess about the z-axis. Taking the result from the previous section, Equation B.76, as our starting point then we know the coherence states will precess around the z-axis as follows:

$$[\hat{\rho}_{coh}(t)] = \mathrm{e}^{-i\Omega_L t} \begin{pmatrix} \frac{1}{2} & i\frac{\hbar\gamma B_0}{k_B T} \\ -i\frac{\hbar\gamma B_0}{k_B T} & \frac{1}{2} \end{pmatrix} \tag{B.77}$$

where Ω_L is the offset Larmor frequency defined in Equation B.32. The magnetization will immediately begin to precess about the z-axis as soon as the 90° pulse is complete, moving all of the magnetization to the x'y'-plane. This tells us that the magnetization will continue to rotate around the z-axis without moving up or down. If we were to apply this result to the result from the 180° pulse, then we would end up with a magnetization that precesses around the negative z-axis at the offset Larmor frequency.

One way to see this is to look at how the expectation value of an operator will change over time by using the formula from [49]

$$i\hbar\frac{\mathrm{d}}{\mathrm{d}t}\langle\hat{Q}\rangle = \langle\left[\hat{Q},\hat{H}\right]\rangle + \left\langle\frac{\partial\hat{Q}}{\partial t}\right\rangle \tag{B.78}$$

For the case of the expectation value of the magnetization of our ensemble of spin-$\frac{1}{2}$ particles without relaxation, we obtain

$$\frac{\mathrm{d}}{\mathrm{d}t}\langle\vec{M}\rangle(t) = \gamma\langle\vec{M}\rangle(t)\times\vec{B}(t) \tag{B.79}$$

where we see that the expectation value of $\vec{M}$ holds the time-dependence rather than $\vec{M}$ itself.

If we want to add relaxation to the above terms, then we will introduce a new variable in the form described in [50], $\vec{\mathscr{M}}$ which is the sum of the $\langle\vec{M}\rangle$ values. Thus, we can write the magnetization equation of motion as:

$$\frac{\mathrm{d}}{\mathrm{d}t}\vec{\mathscr{M}}(t) = \vec{\mathscr{M}}_0 - \frac{\vec{\mathscr{M}}}{T_R} + \gamma\vec{\mathscr{M}}(t)\times\vec{B}(t) \tag{B.80}$$

The three terms on the right hand side of this equation are as follows: the first is the equilibrium state, or the source term. This consists of the initial condition to which the system returns. The second term is the damping source where T_R is called the relaxation time, and it describes the time it takes for the system to return back to it's original equilibrium state. The third, and last, term is the precession term that was mentioned earlier in Equation B.79.

As it turns out, we cannot assume just one overall T_R. In fact, there are two distinct T_R's: one for the transverse relaxation, T_2, and one for the longitudinal relaxation, T_1. Recall that the equilibrium state is $\vec{\mathscr{M}}_0 = \mathscr{M}_0\hat{z}'$, so that we get three equations of motion for the magnetization, corresponding to the x', y', and z' coordinates:

$$\begin{aligned}
\frac{\mathrm{d}}{\mathrm{d}t}\mathscr{M}_{z'}(t) &= \gamma\left(\vec{\mathscr{M}}(t)\times\vec{B}(t)\right)_{z'} - \frac{\mathscr{M}_{z'}(t)-\mathscr{M}_0}{T_1} \\
\frac{\mathrm{d}}{\mathrm{d}t}\mathscr{M}_{x'}(t) &= \gamma\left(\vec{\mathscr{M}}(t)\times\vec{B}(t)\right)_{x'} - \frac{\mathscr{M}_{x'}(t)}{T_2} \\
\frac{\mathrm{d}}{\mathrm{d}t}\mathscr{M}_{y'}(t) &= \gamma\left(\vec{\mathscr{M}}(t)\times\vec{B}(t)\right)_{y'} - \frac{\mathscr{M}_{y'}(t)}{T_2}
\end{aligned} \tag{B.81}$$

T_1 is known as the spin-lattice relaxation time constant and T_2 is called the spin-spin relaxation time constant. Here, $\vec{B}(t)$ is the total magnetic field which can be defined as

$$\vec{B}(t) = B_0\hat{z}' + \vec{B}_{RF}(t) \equiv \vec{B}_{eff} \tag{B.82}$$

where we see that the total magnetic field is the summation of the static field produced by the scanner and the RF field that is produced by the coil in the VOI (volume of interest). I will then define this to be the effective B-field. This effective B-field is axis of rotation about which the spin will precess. If there is no RF pulse, then the spin will precess about the z-axis, but if there exists a strong RF field produced, it can even flip the spin 180° to rotate around the negative z-axis!

Now assume that the RF field is that of Equation B.34:

$$\vec{B}_{RF}(t) = B_{RF}\cos\left(\omega_{coil}t\right)\hat{x}'$$

where we have set the phase angle of the pulse to zero. This gives the effective field to be:

$$\vec{B}_{eff} = B_0\hat{z}' + B_{RF}\cos(\omega_{coil}t)\,\hat{x}' \tag{B.83}$$

We can use the results from Section B.3 to find the Hamiltonian of this system

$$\begin{aligned}\underline{\hat{H}_{static,RF}} &\cong \omega_{nut}\hat{R}_z(\phi_p)\hat{S}_x\hat{R}_z(-\phi_p) + \Omega_L\hat{S}_z \\ &= \frac{\hbar}{2}\begin{pmatrix} \Omega_L & \omega_{nut}e^{-i\phi_p} \\ \omega_{nut}e^{i\phi_p} & -\Omega_L \end{pmatrix}\end{aligned} \tag{B.84}$$

As a side note, once we have a Hamiltonian of the form (for a two level system):

$$\hat{H} = \begin{pmatrix} E_1 & W_{12} \\ W_{21} & E_2 \end{pmatrix}$$

we can write Rabi's formula which describes the probability of finding a particle in a different state than it started after some time, t. For example if a particle started in the $|\alpha\rangle$ state at t=0, then Rabi's formula would describe the probability of finding it in the $|\beta\rangle$ state at some later time, t. Rabi's formula says [50]:

$$\mathscr{P}_{|\alpha\rangle|\beta\rangle}(t) = \frac{4\left|W_{|\alpha\rangle|\beta\rangle}\right|^2}{4\left|W_{|\alpha\rangle|\beta\rangle}\right|^2 + \left(E_{|\alpha\rangle} - E_{|\beta\rangle}\right)^2}\sin^2\left[\sqrt{4\left|W_{|\alpha\rangle|\beta\rangle}\right|^2 + \left(E_{|\alpha\rangle} - E_{|\beta\rangle}\right)^2}\frac{t}{2\hbar}\right] \tag{B.85}$$

so that all we have to do is now replace

$$\begin{aligned} E_1 \equiv E_{|\alpha\rangle} &= \frac{\hbar}{2}\Omega_L \\ E_2 \equiv E_{|\beta\rangle} &= -\frac{\hbar}{2}\Omega_L \\ |W_{12}| \equiv \left|W_{|\alpha\rangle|\beta\rangle}\right| &= \frac{\hbar}{2}\omega_{nut}\end{aligned} \tag{B.86}$$

so that we get the simplified probability of being in the $|\beta\rangle$ state:

$$\mathscr{P}_{|\alpha\rangle|\beta\rangle}(t) = \frac{\omega_{nut}^2}{\omega_{nut}^2 + \Omega_L^2}\sin^2\left[\sqrt{\omega_{nut}^2 + \Omega_L^2}\frac{t}{2}\right] \tag{B.87}$$

Thus when we are far from resonance $\Omega_L >> \omega_{nut}$, then the amplitude of $\mathscr{P}$ is very small, indicating that the probability of transitioning from one state to another is

small. While, when we are exactly on resonance $\Omega_L = 0$, it is possible to have a 100% chance of moving from one state to another, while at other times there is a zero percent chance, due to the $\sin^2[\ ]$ dependence.

Getting back to Equation B.81, we recall that T_1 is the spin-lattice time constant. This time constant correlates to a loss of energy from our system, given back to the lattice in which our nucleus is being held. By exciting the nucleus from the $|\beta\rangle$ state, we are adding energy to the system. As this particle vibrates and rotates in it's lattice, it will lose energy, returning to thermal equilibrium.

T_2, on the other hand, is not a process which dissipates energy, but instead is a dephasing of the transverse magnetization. Recall from Section B.2 and Equation B.27 that as a single spin precesses around the z-axis (or even the $\vec{B}_{eff}$ field) that it will pick up a phase factor. Since we are analyzing an ensemble of spins, it is likely that different spins will accumulate different phases as they precess. Because of this, the averaging of all the magnetizations, including their phases, will cancel the transverse magnetization. Note, this does NOT meant that there is no longer a transverse magnetization, but instead the transverse magnetization exists, it is just averaging to zero.

C. Introduction to the Scanner

The scanner is one of the most important hardware components in the MRI and MRS data acquisition. It uses powerful magnetic fields to take advantage of the NMR effect. Figure C.1 shows the magnetic bore with it's powerful B_0 field going along the z-axis. The B_0 field is used to align the magnetic moments of the molecules contained within the subject. See Section B.6 for details.

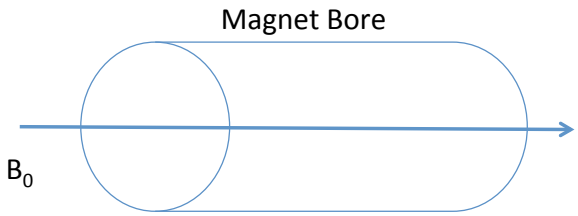

Figure C.1. The magnetic bore with a uniform B_0 field passing through the center of the scanner. This field aligns the magnetic moments of the sample to point along the direction of B_0.

One important component to the scanner is the use of magnetic field gradients. First, I will introduce how gradients are made and then how they are used.

Figure C.2 shows that if there exists two coils with current flowing in opposite directions, you can superimpose the individually produced magnetic fields to achieve a linear gradient. Thus, coils with opposite flowing currents are used to create these magnetic field gradients. The simple coil design for the x-, y-, and z-axis are shown in Figure C.3(a). Notice that arcs are used for the x- and y-axis gradient coils and loops are used for the z-axis gradient coils. Finally, Figure C.4 shows how these magnetic fields interact to produce a y-axis gradient. The magnetic fields from the arcs produce four different magnetic fields that, when superimposed, will add and

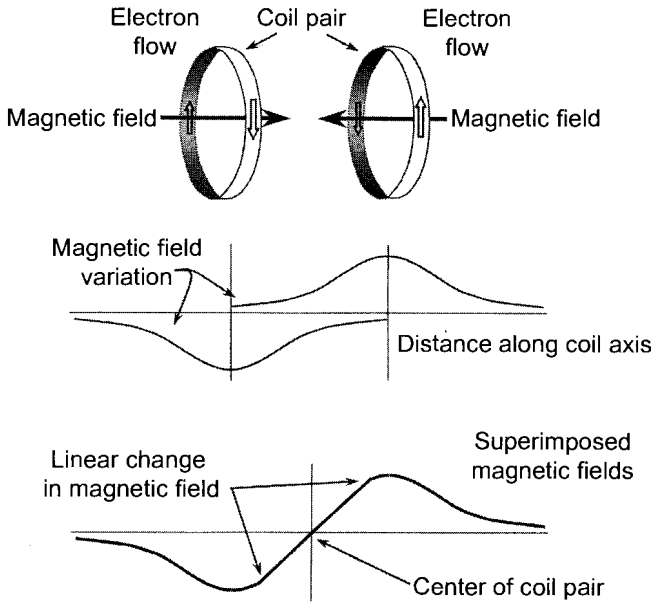

Figure C.2. Two single-loop coils with current flowing in opposite directions. These produce the individual fields seen in the middle picture. When the two fields are added, a linear magnetic field gradient is produced.

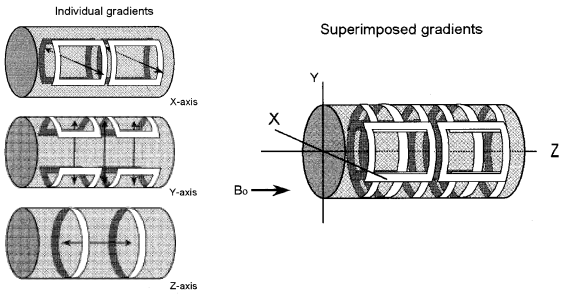

(a) The basic design of gradient coils are shown for each axis [31].

(b) One possible design for gradient coils in a real NMR system [54].

Figure C.3. The basic principle of gradients is superposition of magnetic fields produced from two coils, Figure C.3(a). This same idea can be expanded on and then used as seen in Figure C.3(b).

subtract to cancel out the gradient field in the center of the coils and create gradients in other locations.

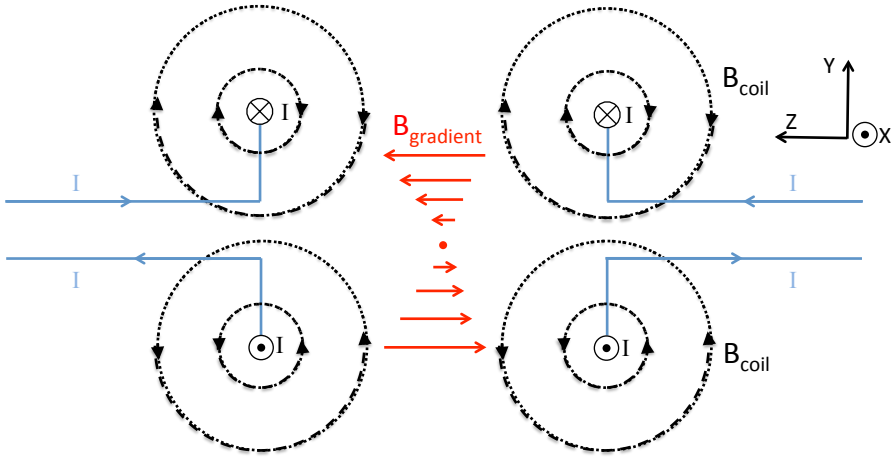

Figure C.4. Four arcs with currents flowing in opposite directions. These produce the individual fields seen here. This is a side view of the coils in the shape of those shown in Figure C.3(a). The current in the bottom left arc flows out of the page through the arc and then travels up and to the left to complete the circuit.

Gradients are used to "move" through k-space, see Section 2.1, and to spatially localize positions within the body for imaging: slice selection, frequency encoding, and phase encoding. By applying a gradient, we are essentially changing the precessional frequencies about the B_0 axis, Figure C.5.

When a z-gradient is applied to the magnet bore, a slice selection gradient (SSG) is said to have been applied. This allows the nuclei along the z-axis to change their precessional frequency in a fashion as shown in Figure C.5. When RF signals are then applied to the ROI, they are done so at a certain frequency, usually the Larmor frequency, ω_L. Since the nuclei along the gradient have had their Larmor frequency changed due to the gradient, only the "slice" that remains at the Larmor frequency will be excited, Figure C.6(a). The thickness of the slice can be changed by applying a different gradient strength, as seen in Figure C.6(b).

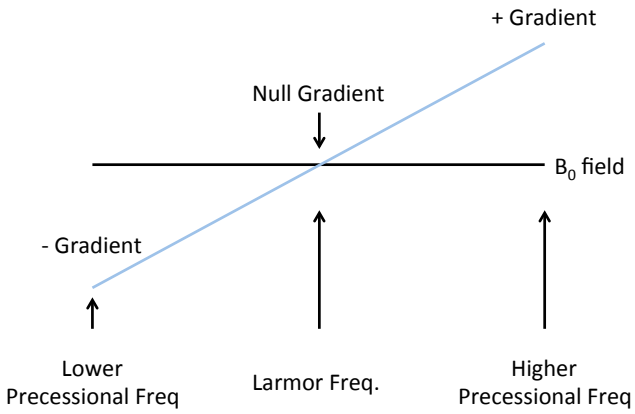

Figure C.5. The application of a gradient changes the precessional frequency about B_0. The nuclei in the negative gradient will have a smaller magnetic field, and thus will have a smaller precessional frequency; while the nuclei in the positive gradient will have a larger magnetic field and will precess at a faster frequency.

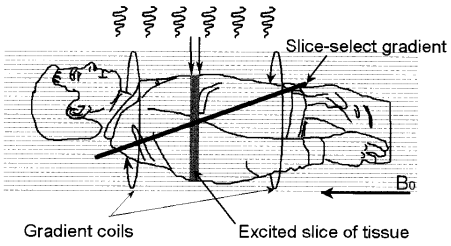

(a) Only the slice that precesses at the Larmor frequency will be excited

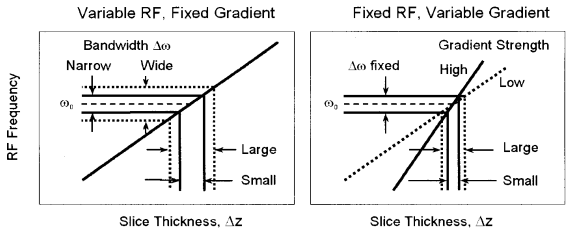

(b) By applying stronger or weaker RF pulses, the thickness of the slice can be changed. Here, ω_0 denotes the Larmor frequency

Figure C.6. The gradient along the z-axis, the transverse direction, determines the slice thickness. Both pictures were obtained from [31].

By applying the slice selective gradient along the z-axis, a spatial dependence has been established along the z-axis. Now, for the other two directions, x and y, a different gradient can be applied, called the frequency encoding gradient (FEG) and the phase encoding gradient (PEG).

The FEG is similar to the SSG, but is in a direction perpendicular to the B_0 field, for example in the x-direction. So, if one were to view the subject down the z-axis, the frequency profile looks similar to that shown in Figure C.5, but now along the x-axis as opposed to the z-axis, as in the SSG. What this FEG does, is to set different frequencies along the, in this case, x-axis. See Figure C.7 for a schematic of the FEG.

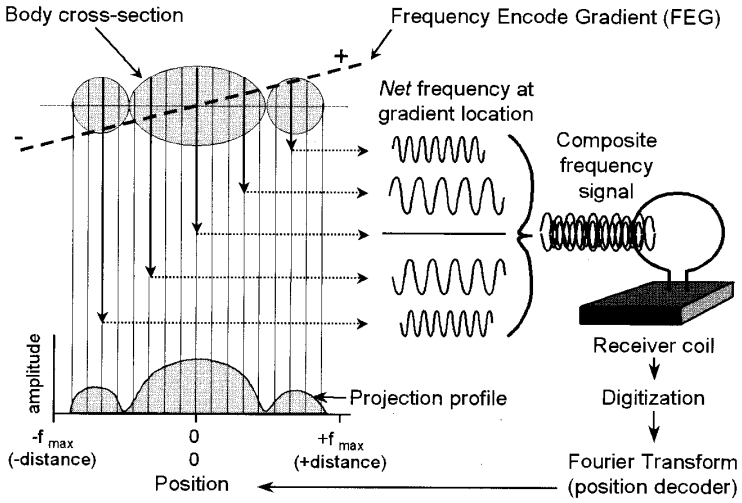

Figure C.7. An axial view of a subject. The frequency encoding gradient (FEG) is along the x-axis in this case. Notice that the frequency of the signal from the subject increases along the gradient. The receiver detects the total signal of different frequencies, and through a Fourier Transform, decodes the position of the signal source from the different frequencies observed. This figure is from [31]

Now that two dimensions have been mapped, it's time to show how the third dimension can be localized. This is done through the use of a Phase Encoding Gradient (PEG). The PEG is different from the other two gradients because it is turned on for

a brief amount of time and then turned back off. This allows some nuclei to precess around the B_0 field faster or slower than others. Once again, referring to Figure C.5, nuclei in the positive gradient will precess at a faster speed than those that precess at the Larmor frequency at the null point of the gradient field.

Figure C.8 shows how a particular set of nuclei will behave when applied with a certain gradient field, top scale. Below the applied PEG, there is a color-coded spectrum showing the range of frequencies which will occur due to this PEG. Figure C.8 also shows four different times: t_0, t_1, t_2, and t_3. These times associate with the following: at t_0 the PEG has not been turned on and all nuclei are precessing at the Larmor frequency, ω_L. For $t_0 < t \leq t_1$, the PEG has just been turned on and we see that the nuclei begin to separate due to the different frequencies. At some time t_2 the nuclei have been subjected to the PEG for a greater length of time and separate even more. For $t_2 \leq t < t_3$, the PEG is turned off and the nuclei return to precessing at the Larmor frequency, but now with a distinctive phase that depends on their positioning within the subject and gradient.

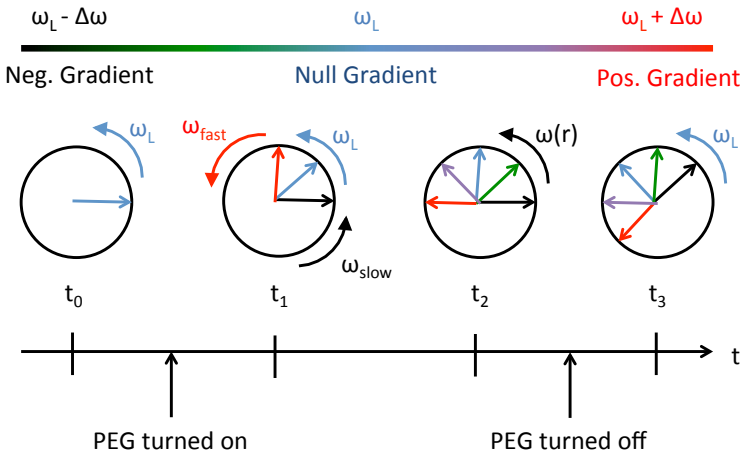

Figure C.8. A schematic of the phases for different nuclei as a function of time that are subjected to some PEG. Note the color coded dependence shown (blue is the Larmor frequency) and that we can define: $\omega_{fast} = \omega + \Delta\omega$ as well as $\omega_{slow} = \omega - \Delta\omega$.

Figure C.9 shows that the PEG can be applied many different times through the course of a scan. In doing so, it effectively gives an alternate viewpoint of the subject. Another way to think of it would be to note that the gradients "move" us through the k-space matrix. By applying a different strength of gradient for a certain time, we are moving through k-space in the k_y direction. In the case of Figure C.9, we have a 256x256 matrix, and so we have applied the PEG 256 different times to fill the entire k-space matrix.

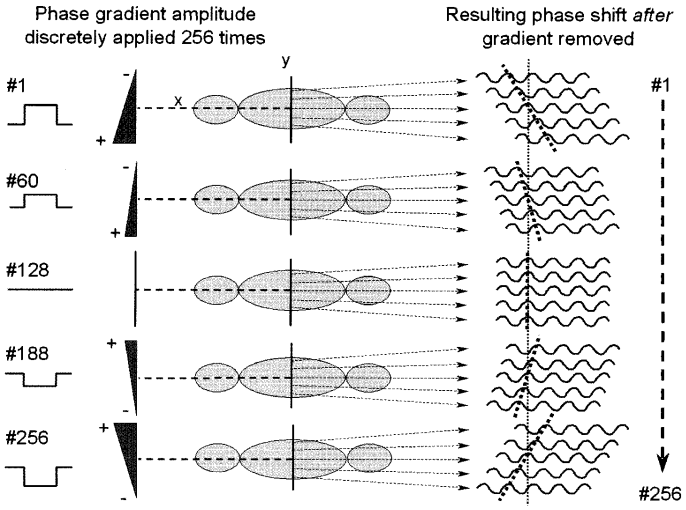

Figure C.9. This figure, obtained from [31], shows the different applications of different strength PEGs. Once the PEG has been turned off, the signals have accumulated different phases based on their position within the subject and the applied gradient. The PEG is applied with different strengths for every repetition time (TR). This is in contrast to the SSG and the FEG which maintain a fixed strength throughout every TR within the acquisition.

With the introduction of the FEG and the PEG, all three dimensions have been mapped out and could now be decoded through a Fourier Transform. Since the gradient strengths are known, once the FT has decoded the individual frequencies, the position can be calculated from the known gradient strengt

LIST OF REFERENCES

LIST OF REFERENCES

[1] IJ Cox, DK Menon, J Sargentoni, DJ Bryant, AG Collins, GA Coutts, RA Iles, JD Bell, IS Benjamin, S Gilbey, HJF Hodgson, and MY Morgan. P-31 Magnetic-Resonance Spectroscopy of the Human Liver uing Chemical-Shift Imaging Techniques. *Journal of Hepatology*, 14(2-3):265–275, MAR 1992.

[2] Steven F. Solga, Alena Horska, Jeanne M. Clark, and Anna Mae Diehl. Hepatic 31p magnetic resonance spectroscopy: a hepatologist's user guide. *Liver International*, 25(3):490–500, 2005.

[3] RV Tse, M Hawkins, G Lockwood, JJ Kim, B Cummings, J Knox, M Sherman, and LA Dawson. Phase I Study of Individualized Stereotactic Body Radiotherapy for Hepatocellular Carcinoma and Intrahepatic Cholangiocarcinoma. *Journal of Clinical Oncology*, 9(48):404–410, 2008.

[4] SS Lo, LA Dawson, EY Kim, NA Mayr, JZ Wang, Z Huang, and HR Cardenes. Stereotactic Body Radiotherapy for Hepatocellular Carcinoma. *Discovery Medicine*, 9(48):404–410, 2010.

[5] HR Cardenes, TR Price, SM Perkins, M Maluccio, P Kwo, TE Breen, MA Henderson, TE Schefter, K Tudor, J Deluca, and PA Johnstone. Phase I Feasibility Trial of Stereotactic Body Radiation Therapy for Primary Hepatocellular Carcinoma. *Clinical and Translational Ooncology*, 12(3):218–225, 2010.

[6] Charlie C. Pan, Brian D. Kavanagh, Laura A. Dawson, X. Allen Li, Shiva K. Das, Moyed Miften, and Randall K. Ten Haken. Radiation-Associated Liver Injury. *International Journal of Radiation Oncology*Biology*Physics*, 76(3, Supplement):S94 – S100, 2010. Quantitative Analyses of Normal Tissue Effects in the Clinic.

[7] A Panda, S Jones, K Sandrasegaran, and U Dydak. Monitoring Response of Liver Cancer to Targeted Radiation Therapy with a Novel ^{31}P,^{1}HMRS Coil. page 3470. AAPM Conference, 2010.

[8] S Jones, A Panda, H Cardenes, J Fletcher, G Hutchins, and U Dydak. A Spatially Resolved Evaluation of Radiation Induced Metabolic Response in Normal and Malignant Liver with 3D ^{31}PMRSI. ISMRM Conference, 2012.

[9] Ahmedin Jemal, Freddie Bray, Melissa M. Center, Jacques Ferlay, Elizabeth Ward, and David Forman. Global cancer statistics. *CA: A Cancer Journal for Clinicians*, 61(2):69–90, 2011.

[10] E A Eisenhauer, P Therasse, J Bogaerts, L H Schwartz, D Sargent, R Ford, J Dancey, S Arbuck, S Gwyther, M Mooney, L Rubinstein, L Shankar, L Dodd, R Kaplan, D Lacombe, and J Verweij. New response evaluation criteria in solid tumours: revised RECIST guideline (version 1.1). *Eur J Cancer*, 45(2):228–247, Jan 2009.

[11] Ri-Sheng Yu, Liang Hao, Fei Dong, Jian-Shen Mao, Jian-Zhong Sun, Ying Chen, Min Lin, Zhi-Kang Wang, and Wen-Hong Ding. Biochemical Metabolic Changes Assessed by ^{31}P Magnetic Resonance Spectroscopy After Radiation-Induced Hepatic Injury in Rabbits. *World Journal of Gastroenterology*, 15(22):2723–2730, 2009.

[12] Igor Sersa, Simona Kranjc, Gregor Sersa, Alenka Nemec-Svete, Bojan Lozar, Ana Sepe, Jernej Vidmar, and Marjeta Sentjurc. Study of Radiation Induced Changes of Phosphorus Metabolism in Mice by ^{31}PNMR Spectroscopy. *Radiation and Oncology*, 44(3):174–179, May 2010.

[13] H Pan, Simpson DR, LK Mell, AJ Mundt, and JD Lawson. A Survey of Stereotactic Body Radiotherapy use in the United States. *Cancer*, pages 4566–4572, 2011.

[14] DL Andolino, HR Cardenes, and et al. Stereotactic Body Radiotherapy for Primary Hepatocellular Carcinoma. *International Journal of Radiation Oncology*Biology*Physics*, 2011.

[15] I Lax, H Blomgren, I Näslund, and R Svanström. Stereotactic radiotherapy of malignancies in the abdomen. methodological aspects. *Acta Oncol*, 33(6):677–83, 1994.

[16] L Potters, M Steinberg, C Rose, R Timmerman, S Ryu, JM Hevezi, J Welsh, M Mehta, DA Larson, and NA Janjan. American Society for Therapeutic Radiology and Oncology and American College of Radiology Practice Guideline for the Performance of Stereotactic Body Radiation Therapy. *International Journal of Radiation Oncology*Biology*Physics*, 60(4):1026–1032, 2004.

[17] GM Glazer, SR Smith, TL Chenevert, PA Martin, AN Stevens, and RH Edwards. Image Localized ^{31}PMagnetic Resonance Spectroscopy of the Human Liver. *NMR in Biomedicine*, 1(4):184–189, 1989.

[18] IJ Cox, JD Bell, CJ Peden, RA Iles, CS Foster, P Watanapa, and RC Williamson. In Vivo and In Vitro ^{31}PMagnetic Resonance Spectroscopy of Focal Hepatic Malignancies. *NMR in Biomedicine*, 5(3):114–120, 1992.

[19] Pieter C. Dagnelie, Paul E. Sijens, Deni J. A. Kraus, André S. Th. Planting, and Pieter van Dijk. Abnormal liver metabolism in cancer patients detected by 31p mr spectroscopy. *NMR in Biomedicine*, 12(8):535–544, 1999.

[20] Anshuman Panda, Scott Jones, Helmut Stark, Rahul S. Raghavan, Kumar Sandrasegaran, Navin Bansal, and Ulrike Dydak. Phosphorus Liver MRSI at 3T Using a Novel Dual-tuned Eight-channel 31P/1H Coil. *Magnetic Resonance in Medicine*, 68(5):1346–1356, 2012.

[21] Anshuman Panda. *Fast ^{31}PMagnetic Resonance Spectroscopic Imaging of the Liver: Clinical Implementation and Applications in Post-Radiation Therapy Response Monitoring*. Phd thesis, Purdue University, 2012.

[22] Scott Jones. *3D ^{31}PMRSI of Human Liver: A Spatially Resolved Study of Normal and Malignant Tissue in Response to Stereotactic Body Radiation Therapy*. PhD thesis, Purdue University, 2013.

[23] Robin A. de Graaf. *In Vivo NMR Spectroscopy: Principle and Techniques*. JOHN WILEY & SONS INC, 2nd edition, 2007.

[24] RA Iles, AN Stevens, JR Griffiths, and PG Morris. Phosphorylation Status of Liver by ^{31}P-NMR Spectroscopy, and its Implications for Metabolic Control. *Biochemical Journal*, 229:141–151, 1985.

[25] NJ Serkova, JC Rose, E Epperson, HV Carey, and SL Martin. Quantitative Analysis of Liver Metabolites in Three Stages of the Circannual Hibernation Cycle in 13-Lined Ground Squirrels by NMR. *Physiol Gernomics*, 31:15–24, 2007.

[26] R. M. Dixon, P. W. Angus, B. Rajagopalan, and G. K. Radda. Abnormal phosphomonoester signals in 31P MR spectra from patients with hepatic lymphoma. a possible marker of liver infiltration and response to chemotherapy. *British Journal of Cancer*, 63(6):953–958, 1991.

[27] R Oberhaensli, B Rajagopalan, GJ Galloway, Taylor DJ, and GK Radda. Study of Human Liver Disease with P-31 Magnetic Resonance Spectroscopy. *Gut*, 31(4):463–467, 1990.

[28] DJ Meyerhoff, GS Karczmar, F Valone, and et al. Hepatic Cancers and Their Response to Chemoembolization Therapy: Quantitative Image-Guided 31P Magnetic Resonance Spectroscopy. *Investigative Radiology*, 27:456–464, June 1992.

[29] Z Yuan, XD Ye, S Dong, LC Xu, and XS Xiao. Evaluation of Early Imaging Response After Chemoembolization of Hepatocellular Carcinoma by Phosphorus-31 Magnetic Resonance Spectroscopy - Initial Experience. *Journal of Vascular and Interventional Radiology*, 22(8):1166–1173, 2011.

[30] M. Chmelík, A. I. Schmid, S. Gruber, J. Szendroedi, M. Krššák, S. Trattnig, E. Moser, and M. Roden. Three-Dimensional High-Resolution Magnetic Resonance Spectroscopic Imaging for Absolute Quantification of 31P Metabolites in Human Liver. *Magnetic Resonance in Medicine*, 60(4):796–802, 2008.

[31] Jerrold Bushberg, J. Anthony Seibert, Edwin Leidholdt Jr., and John Boone. *The Essential Physics of Medical Imaging*. Lippincott Williams and Wilkins, 2nd edition, 2002.

[32] U Dydak, M Weiger, KP Pruessmann, D Meier, and P Boesiger. Sensitivity-Encoded Spectroscopic Imaging. *Magnetic Resonance in Medicine*, 46(4):713–722, 2001.

[33] Daniel K. Sodickson and Warren J. Manning. Simultaneous Acquisition of Spatial Harmonics (SMASH): Fast Imaging with Radiofrequency Coil Arrays. *Magnetic Resonance in Medicine*, 38:591–603, 1997.

[34] Peter M. Jakob, Mark A. Griswold, Robert R. Edelman, and Daniel K. Sodickson. AUTO-SMASH: A self-calibrating technique for SMASH imaging. *Magnetic Resonance Materials in Physics, Biology and Medicine*, 7:42–54, 1998.

[35] Mark A. Griswold, Peter M. Jakob, Robin M. Heidemann, Mathias Nittka, Vladimir Jellus, Jianmin Wang, Berthold Kiefer, and Axel Haase. Generalized Autocalibrating Partially Parallel Acquisitions (GRAPPA). *Magnetic Resonance in Medicine*, 47:1202–1210, 2002.

[36] NP Willis and Yoram Bresler. Lattic-Theoretic Analysis of Time-Sequential Sampling of Spatiotemporal Signals- Part II: Large Space-Bandwidth Product Asymptotics. *IEEE Transactions on Information Theory*, 43(1):208–220, January 1997.

[37] Siemens Medical. MAGNETOM Trio. Booklet.

[38] American College of Radiology (ACR), Reston, VA. *Phantom test guidance for the ACR MRI Accreditation Program*, 1998.

[39] R Buchli, CO Duc, E Martin, and P Boesiger. Assessment of absolute metabolite concentrations in human tissue by ^{31}P MRS in vivo. Part I: Cerebrum, cerebellum, cerebral gray and white matter. *Magnetic Resonance in Medicine*, 32(4):447–452, 1994.

[40] A Naressi, C Couturier, JM Devos, M Janssen, C Mangeat, R de Beer, and D Graveron-Demilly. Java-based Graphical User Interface for the MRUI Quantitation Package. *MAGMA*, 12(2-3):141–152, 2001.

[41] D Stefan, FD Cesare, A Andrasescu, E Popa, A Lazariev, E Vescovo, O Strbak, S Williams, Z Starcuk, M Cabanas, D van Ormondt, and D Graveron-Demilly. Quantitation of Magnetic Resonance Spectroscopy Signals: the jMRUI Software Package. *Measurement Science and Technology*, 20(10), 2009.

[42] L Vanhamme, T Sundin, PV Hecke, and SV Huffel. MR Spectrocopic Quantitation: a Review of Time-Domain Methods. *NMR in Biomedicine*, 14(4):233–246, 2001.

[43] P Mandal. In vivo proton magnetic resonance spectroscopic signal processing for the absolute quantitation of brain metabolites. *European Journal of Radiology*, 81:653–664, 2012.

[44] R Pohmann and M von Kienlin. Accurate phosphorus metabolite images of the human heart by 3d acquisition-weighted csi. *Magnetic Resonance in Medicine*, 45:817–826, 2001.

[45] M Griswold, P Jakob, M Nittka, J Goldfard, and A Haase. Partially Parallel Imaging With Localized Sensitivities (PILS). *Magnetic Resonance in Medicine*, 44:602–609, 2000.

[46] F Breuer, M Blaimer, R Heidemann, M Mueller, M Griswold, and P Jakob. Controlled Alisasing in Parallel Imaging Results in Higher Acceleration (CAIPIRINHA) for Multi-Slice Imaging. *Magnetic Resonance in Medicine*, 53:684–691, 2005.

[47] M Lustig, D Donoho, and J Pauly. Sparse MRI: The Application of Compressed Sensing for Rapid MR Imaging. *Magnetic Resonance in Medicine*, 58:1182–1195, 2007.

[48] P Shin, P Larson, M Ohliger, M Elad, J Pauly, D Vigneron, and M Lustig. Calibrationless parallel imaging reconstruction based on structured low-rank matrix completion. *Magnetic Resonance in Medicine*, 72(4):959–970, 2014.

[49] David Griffiths. *Introduction to Quantum Mechanics*. Prentice Hall, 2nd edition, 2005.

[50] C Cohen-Tannoudji, Bernard Diu, and Franck Laloe. *Quantum Mechanics*, volume 1,2. Wiley, 2005.

[51] Malcolm H. Levitt. *Spin Dynamics*. John Wiley & Sons, Ltd, 1st edition, 2001.

[52] W. G. Proctor and F. C. Yu. The Dependence of a Nuclear Magnetic Resonance Frequency upon Chemical Compound. *Phys. Rev.*, 77:717–717, Mar 1950.

[53] Maurice Goldman. *Quantum Description of High Resolution NMR in Liquids*. Oxford, 1988.

[54] http://www.mrsolutions.co.uk/products/system-design/ July 2013.

VITA

VITA

Tony Clevenger was born in Louisville, KY and attended Louisville Male High School, where he began his love of physics and the sciences. After completing high school, he moved on to the University of Louisville where he majored in general physics his 4 years there. Completing his Bachelors of Science degree at the University of Louisville in 2008, he moved on to Purdue University where he accepted a position of a Graduate Student for both a Teaching Assistant and, eventually, a Research Assistant. At Purdue University, Tony completed his Master of Science Degree in Physics in 2011 and continued on with research in the field of Medical Physics.